



HAL
open science

Direct numerical simulations of flow in dense fluid-particle systems

Mohamed Salim Hamidi

► **To cite this version:**

Mohamed Salim Hamidi. Direct numerical simulations of flow in dense fluid-particle systems. Solid mechanics [physics.class-ph]. Université de Perpignan, 2024. English. NNT : 2024PERP0004 . tel-04573580

HAL Id: tel-04573580

<https://theses.hal.science/tel-04573580>

Submitted on 13 May 2024

HAL is a multi-disciplinary open access archive for the deposit and dissemination of scientific research documents, whether they are published or not. The documents may come from teaching and research institutions in France or abroad, or from public or private research centers.

L'archive ouverte pluridisciplinaire **HAL**, est destinée au dépôt et à la diffusion de documents scientifiques de niveau recherche, publiés ou non, émanant des établissements d'enseignement et de recherche français ou étrangers, des laboratoires publics ou privés.

THÈSE

Pour obtenir le grade de
Docteur



Délivré par
UNIVERSITE DE PERPIGNAN VIA DOMITIA

Préparée au sein de l'école doctorale
Energie et Environnement (ED305)

Et de l'unité de recherche
PROMES-CNRS, UPR 8521

Spécialité : **Science de l'ingénieur**

Présentée par **Mohamed Salim HAMIDI**

**Simulations Numériques Directes d'écoulements
denses fluide-particules**

Soutenance prévue le **7 février 2024** devant le jury composé de

M. Stéphane ABIDE , PR, UCA-LJAD	Rapporteur
M. Sylvain SERRA , MCF-HDR, ENSGTI-LaTEP	Rapporteur
M. Jérôme BELLETTRE , PR, Polytech Nantes-LTEN	Examineur
M. Renaud ANSART , PR, INPT-LGC	Examineur
M. Gilles Flamant , DRE, CNRS-PROMES	Examineur
Mme Françoise Bataille , PR, UPVD-PROMES	Directrice de thèse
M. Adrien Toutant , MCF-HDR , UPVD-PROMES	Directeur de thèse
M. Samuel Mer , MCF , UPVD-PROMES	Co-Encadrant de thèse

ACKNOWLEDGEMENTS

Completing this thesis was a journey filled with challenges and learning, and it would not have been possible without the support and guidance of many.

Foremost, I extend my heartfelt gratitude to my supervisors, Francoise Bataille, Adrien Toutant, and Samuel Mer. Their expertise and mentorship have been pivotal in my research journey. Francoise's insightful guidance, Adrien's innovative problem-solving approaches, and Samuel's thorough and thoughtful advice have been invaluable to my growth and the success of this work.

I am sincerely grateful to my thesis committee members, Stéphane Abide, Sylvain Serra, Jérôme Bellettre, Renaud Ansart, and Gilles Flamant, for their willingness to review my work.

A special thank you to my teammates, Dorian, Jean-Marc, Damien, Sofia, Simon and Edouard. Working alongside them in a collaborative and dynamic environment has been one of the highlights of my Ph.D. journey. Their perspectives and support played a crucial role in my research.

My sincere appreciation goes to the IT team, Philippe and Faissal. Their technical expertise and prompt assistance with the computing resources were vital for my research. I would also like to extend my thanks to the HR team - Sandrine, Armelle, Naouel, and Romie. Their efficient handling of administrative tasks and supportive approach made many processes smoother and easier.

Lastly, I want to acknowledge the other lab staff, members, and fellow colleagues and students. Although too many to name individually, their collective wisdom, encouragement, and camaraderie have been a constant source of motivation and have greatly enriched my experience.



1

RÉSUMÉ

Contexte

En 2023, le constat alarmant sur l'état du climat mondial s'est accentué. Cette année a été confirmée comme la plus chaude depuis le début des relevés de températures globales en 1850, surpassant de manière significative le précédent record établi en 2016. Avec une moyenne de 0.60°C au-dessus de la période de référence 1991-2020 et 1.48°C au-dessus des niveaux préindustriels de 1850-1900 [25]. Dans ce contexte, les Accords de Paris sur le climat, qui visent à maintenir l'augmentation de la température moyenne mondiale par rapport à la période préindustrielle « bien en dessous de 2°C » voir de préférence à limiter cette hausse à 1,5°C, prennent une importance renouvelée. Etant donné que ce seuil est considéré comme crucial pour éviter les effets les plus dévastateurs du changement climatique.

La COP28 a constitué un jalon majeur dans cette lutte. Elle a marqué la fin du premier « bilan mondial » des actions menées en vertu de l'Accord de Paris. Ce bilan a mis en évidence le manque de progrès dans tous les aspects de l'action climatique, incluant la réduction des émissions de gaz à effet de serre, le renforcement de la résilience climatique, et l'apport de soutien financier et technologique aux nations vulnérables. Bien que la COP28 ait été l'objet de controverses en raison de son organisation par un pays producteur de pétrole elle a été un moment inédit : pour la première fois, les énergies fossiles, principales causes du dérèglement climatique, ont été explicitement ciblées dans l'accord final, signalant ainsi le début de la fin de l'ère des combustibles fossiles. Cette avancée marque un tournant politique et économique important, fruit de la mobilisation persistante de la société civile et de nombreux États. Le texte final appelle les nations du monde entier à « abandonner les combustibles fossiles dans les systèmes énergétiques de manière juste, ordonnée et équitable », en accélérant les actions nécessaires pour atteindre la neutralité carbone d'ici 2050. Pour y parvenir, l'accord prévoit de tripler la capacité mondiale des énergies renouvelables et de doubler le taux d'amélioration annuel moyen de l'efficacité énergétique d'ici 2030 [24].

Dans ce paysage énergétique en mutation le solaire à concentration (CSP) sera amené à gagner en importance dans le mix énergétique mondial. Contrairement aux systèmes

photovoltaïques (PV) plus connus, qui transforment directement la lumière du soleil en électricité grâce à des matériaux semi-conducteurs, les systèmes de solaire à concentration (CSP) fonctionnent en focalisant la lumière solaire sur une petite surface pour générer une chaleur intense, qui est ensuite convertie en électricité par un processus thermique. Au cœur du principe de fonctionnement du CSP se trouve l'utilisation de miroirs ou de lentilles pour concentrer une grande surface de lumière solaire en un faisceau focalisé vers un récepteur. Cette énergie solaire concentrée est d'abord absorbée par le récepteur, puis utilisée pour chauffer un fluide caloporteur. Ce fluide chauffé est ensuite utilisé, directement ou indirectement, comme source de chaleur pour alimenter un cycle thermodynamique de production d'électricité (voir figure 1.1).

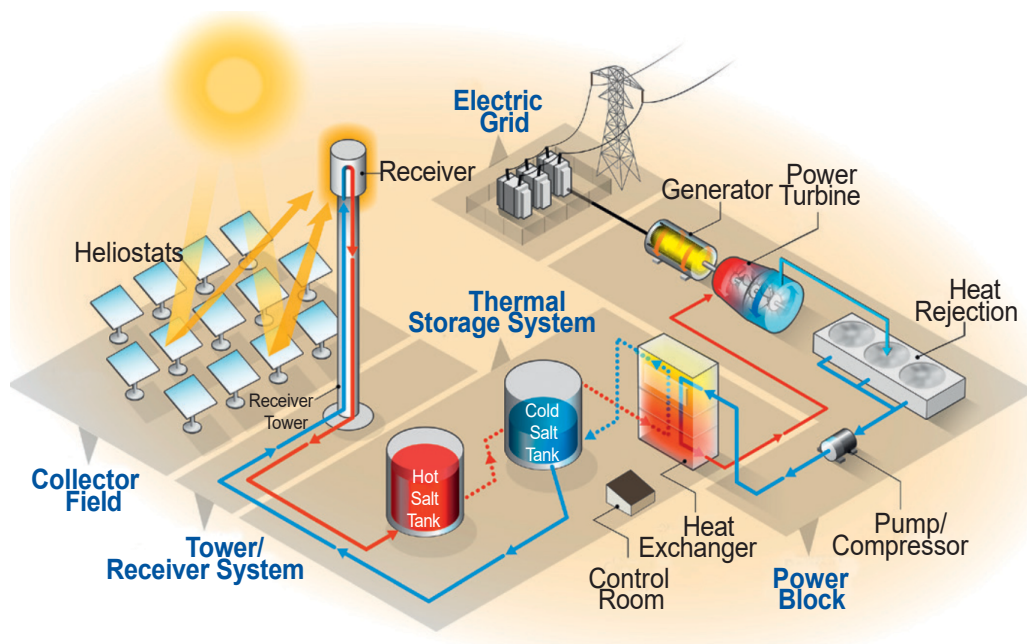


Figure 1.1: Fonctionnement d'une centrale solaire à concentration[84].

Bien que la capacité installée des technologies CSP soit actuellement faible comparée à celle des énergies photovoltaïque et éolienne, ces technologies présentent un potentiel de croissance significatif pour l'avenir. On s'attend à ce que les systèmes CSP se développent parallèlement aux capacités croissantes des énergies PV et éolienne, contribuant ainsi à un mix énergétique mondial plus équilibré et durable [59]. En effet, l'ajout de sources d'énergie renouvelables contrôlables peut être très bénéfique pour compenser les fluctuations de puissance causées par la nature intermittente des énergies PV et éolienne. À cet égard, les systèmes CSP, en particulier lorsqu'ils sont couplés avec du stockage d'énergie thermique (TES), peuvent jouer un rôle significatif dans l'équilibrage de la courbe d'offre et de demande d'électricité. Cela aide à assurer une fourniture d'électricité stable et fiable sur le réseau [59]. De plus, les systèmes CSP sont également d'excellents systèmes de production d'électricité dans la gamme de 10 à 1000 MW [84]. Cependant, un obstacle majeur freinant la commercialisation à grande échelle du solaire à concentration (CSP) est son coût nominal élevé de l'électricité (LCOE) comparé à celui du photovoltaïque et de l'éolien terrestre. Pour renforcer la position concurrentielle du

CSP, des efforts importants en vue de réduire les coûts et d'améliorer les performances de tous les sous-systèmes des centrales CSP sont vivement souhaités.

Actuellement, les technologies CSP de troisième génération font l'objet de recherches intensives. L'objectif principal est d'augmenter l'efficacité de conversion de l'énergie solaire en électricité afin de réduire le coût de l'électricité générée (LCOE). Une des stratégies consiste à améliorer l'efficacité du cycle, notamment en utilisant le cycle Brayton avec des températures de cycle maximales dépassant les 700 °C. Un autre aspect crucial pour améliorer les performances concerne le choix du fluide caloporteur. Divers fluides caloporteurs sont à l'étude, notamment les gaz à haute pression, les sels fondus à haute température et les particules solides [9]. En particulier, cette dernière option offre plusieurs avantages, tels qu'une plage de température de fonctionnement plus large et une stabilité thermique améliorée, qui pourraient optimiser l'efficacité et les performances des systèmes CSP [7].

Les fluides caloporteurs à base de particules suscitent un intérêt grandissant dans le domaine du CSP, avec diverses technologies développées à travers le monde [78, 64, 41]. La technologie d'intérêt pour ce travail de thèse est le récepteur solaire à particules tubulaire verticale, également connu sous le nom de lit fluidisé bouillonnant ascendant (UBFB), développé par le laboratoire PROMES-CNRS en France, en collaboration avec des partenaires internationaux. Cette recherche fait partie des projets européens "CSP-2" et "Next-CSP" [46, 61].

La figure 1.2 représente le système UBFB (Upflow Bubbling Fluidized Bed) en conditions d'ensoleillement (à gauche), un diagramme schématisé du système (au centre), ainsi que les phénomènes de bullage et de bouchonnage observables à température ambiante (à droite). Le système UBFB repose sur des tubes immergés dans un réservoir

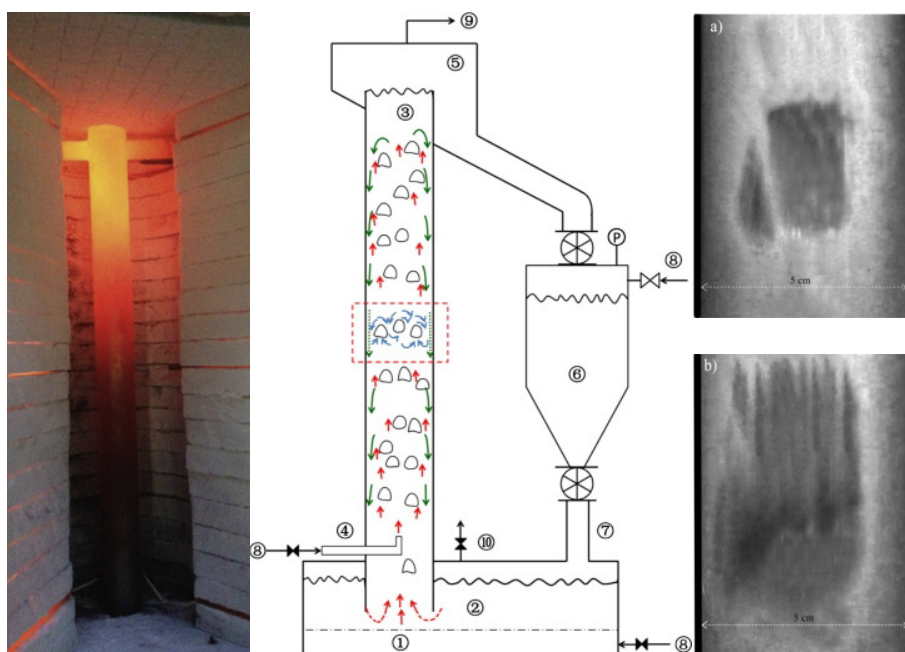


Figure 1.2: Représentation du récepteur solaire à particules en écoulement vertical

d'alimentation pour les particules (le distributeur). Lorsque de l'air est introduit dans le distributeur sous des conditions bien spécifiques, il en résulte la suspension des particules solides dans le flux d'air montant. Le mélange en suspension exhibe des caractéristiques similaires à celles d'un fluide. Par exemple, le mélange peut s'écouler librement et s'adapter à la forme de son contenant, générant des bulles, etc. Ce phénomène est connu sous le nom de fluidisation.

En appliquant une pression dans la partie supérieure libre du distributeur, un flux de particules ascendant dans les tubes est obtenu avec une large gamme de fractions volumiques solides. Des études expérimentales ont montré que les récepteurs UBFB peuvent atteindre des coefficients de transfert de chaleur de l'ordre de 800 à 1200 watts par mètre carré par kelvin, les rendant très efficaces sous diverses conditions d'irradiation [8, 126, 128, 55]. Le concept UBFB offre plusieurs autres avantages technologiques, notamment l'utilisation d'un récepteur tubulaire similaire à ceux utilisés avec des sels fondus et la capacité d'utiliser le même milieu comme fluide caloporteur et matériau de stockage. Contrairement aux sels fondus, les particules ne sont pas limitées à une plage de température de fonctionnement spécifique, permettant des températures de fonctionnement élevées et une conversion de chaleur-électricité plus efficace via des cycles thermodynamiques à haute température [7]. D'un point de vue économique, la technologie UBFB peut potentiellement réduire les coûts associés au fluide caloporteur et au milieu de stockage, car les particules sélectionnées peuvent être nettement moins chères que les sels fondus [67]. D'un point de vue environnemental, l'utilisation de particules minérales peut aider à diminuer l'empreinte écologique globale de la centrale électrique [69].

La recherche expérimentale sur les récepteurs UBFB s'est principalement concentrée sur des configurations de petite échelle avec des tubes courts (1 à 2 mètres) et des tubes un peu plus longs (jusqu'à 4 mètres) mais dans des conditions de température ambiantes. Pour passer à l'échelle commerciale de la technologie UBFB (10 à 50 MWth), des tubes plus longs (d'au moins 6 mètres) sont nécessaires. Cependant, des études antérieures ont montré que les régimes de fluidisation dans les tubes varient de manière significative avec la hauteur des tubes. La performance thermique du récepteur solaire dépend grandement de cette hydrodynamique complexe. Bien comprendre la physique des écoulements multiphasiques devient donc un enjeu crucial pour concevoir des systèmes UBFB viables et efficaces.

Les écoulements fluide-particules, en particulier dans les systèmes de lits fluidisés, illustrent très bien le caractère multi-échelles de la physique gouvernant ces écoulements (voir Figure 1.3). À la plus petite échelle, la physique est dictée par des interactions telles que les collisions, les couches limites et les sillages de particules. Ces interactions se produisent à des échelles de temps de l'ordre de la microseconde voire de la nanoseconde. La fraction volumique solide, qui varie considérablement dans ces systèmes, influence également l'équilibre entre les interactions collisionnelles et la dynamique des particules dans le fluide, avec une complexité émergente à mesure que la concentration de particules augmente. À l'échelle macroscopique, le comportement est influencé par le contexte d'application, englobant des structures et des phénomènes d'écoulement à grande

échelle. Cela inclut des phénomènes comme la formation de bulles et la recirculation de particules, les frontières introduisant des inhomogénéités supplémentaires. L'interaction entre ces échelles est bidirectionnelle, chaque échelle influençant et étant influencée par les autres, rendant la prédiction et la compréhension de tels flux une tâche complexe [105].

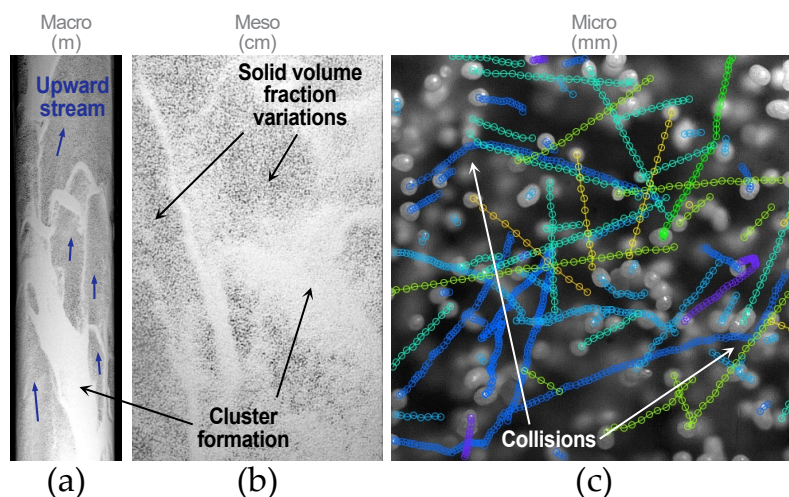


Figure 1.3: (a) Illustration du caractère multi-échelle des écoulements fluide-particules.

Dans ce contexte, la simulation numérique, en particulier les techniques de simulation numérique directe (SND), offre une approche complémentaire aux méthodes analytiques et expérimentales pour mieux comprendre la physique des écoulements multiphasiques. Dans la SND, les équations régissant la phase fluide sont résolues sans aucune simplification ni modélisation de la turbulence, capturant toute la gamme d'échelles présentes dans l'écoulement. Cette méthode requiert toutefois d'importantes ressources informatiques en raison de la nécessité de résoudre toutes les échelles pertinentes, des plus petits tourbillons aux plus grandes structures d'écoulement. Cependant, le SND offre un aperçu inégalé des mécanismes fondamentaux régissant le comportement de l'écoulement, en fournissant des informations détaillées sur le mouvement et les interactions des phases, telles que les trajectoires, vitesses et taux de collision des particules, ainsi que la vitesse instantanée du fluide... Même s'il n'est généralement pas possible d'utiliser cette méthode pour simuler directement des systèmes de taille industrielle en raison de l'intensité des calculs requis, les avancées dans le domaine informatique et le développement de méthodes numériques plus efficaces permettent désormais de réaliser des SND sur des systèmes autrefois hors de portée.

Il est désormais possible de modéliser avec précision l'évolution des écoulements particuliers impliquant plusieurs centaines de particules, sur des échelles de temps permettant une convergence statistique. De plus, les méthodes DNS peuvent être utilisées dans une approche de remontée d'échelle, fournissant ainsi des informations précieuses pour des méthodes plus macroscopiques telles que la méthode des deux fluides, qui dépendent de lois de fermeture précises. Une fois à maturité, on s'attend à ce que les simulations numériques directes réalisées contribuent grandement aux phases de conception et d'optimisation des systèmes d'ingénierie. Cela réduira non seulement le besoin de tests

pilotes expérimentaux, mais également le temps nécessaire à la commercialisation des nouvelles technologies. À cette fin, l'objectif principal de cette thèse est de développer une méthode de simulation numérique directe capable de simuler efficacement un écoulement de particules impliquant plus de quelques centaines de particules. Cette méthode sera implémentée dans le code de calcul TrioCFD, initialement développé par le CEA pour étudier les écoulements diphasiques gaz/liquide dans les réacteurs nucléaires. Cependant, la version standard de ce code n'a actuellement pas la capacité de simuler des écoulements granulaires. Par conséquent, notre implémentation nécessitera l'utilisation d'une technique appropriée pour imposer la contrainte de rigidité dans la phase solide, ainsi que l'implémentation d'un modèle de collision pour prendre en compte les interactions entre les particules.

La suite de ce résumé suit le texte principal de la thèse en présentant, dans un premier temps, la méthodologie et l'algorithme développés. Ensuite, nous présenterons des cas tests de validation et les principaux résultats obtenus à partir des simulations réalisées.

Méthode

L'algorithme utilisé dans ce travail pour réaliser des simulations numériques directes des écoulements fluide-particules est basé sur le formalisme mono-fluide (one-fluid). Dans cette approche, un seul ensemble d'équations est utilisé pour décrire le comportement de toutes les phases présentes dans le domaine de calcul. Les différentes phases sont traitées comme un seul fluide dont les propriétés matérielles varient spatialement, en fonction de la fonction indicatrice de phase I . Les équations gouvernantes sont données par :

$$\nabla \cdot \mathbf{u} = 0 \quad (1.1a)$$

$$\frac{\partial \rho \mathbf{u}}{\partial t} + \nabla \cdot (\rho \mathbf{u} \mathbf{u}) = -\nabla p + \nabla \cdot \left(\mu \left(\nabla \mathbf{u} + \nabla^T \mathbf{u} \right) \right) + \rho \mathbf{g} + \mathbf{F}_c \quad (1.1b)$$

Où \mathbf{u} représente le champ de vitesse, ρ le champ de densité, p le champ de pression, μ le champ de viscosité dynamique, \mathbf{g} l'accélération gravitationnelle et \mathbf{F}_c la force de collision. Les deux phases sont considérées comme incompressibles. ρ et μ sont considérés constants dans chaque phase mais présentent une transition abrupte à travers l'interface. Les équations sont identiques à celles d'un écoulement monophasique. Par conséquent, les techniques développées pour résoudre les équations pour les écoulements monophasiques peuvent être facilement utilisées. La seule différence est que le solveur doit être adapté pour gérer les propriétés matérielles variant spatialement.

Lors de la résolution numérique des équations précédentes, il est nécessaire d'identifier la phase présente n'importe où dans le domaine. Pour cela, la fonction indicatrice de phase I est introduite. Elle est définie comme étant égale à 1 dans la phase solide, à 0 dans la phase fluide, et égale à la fraction volumique solide $\alpha = V_s/V_{cell}$ dans toutes les

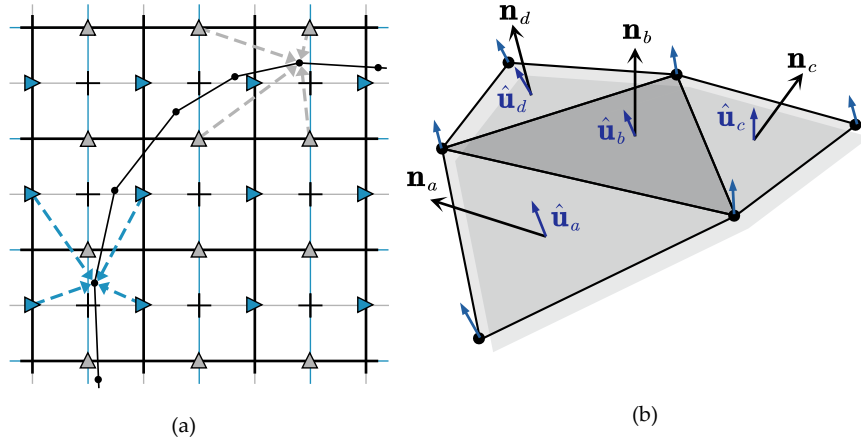


Figure 1.4: Représentation graphique des maillages de résolution (a) maillage fixe, (b) maillage mobile.

cellules traversées par une interface. Dans les cellules biphasées, la densité est définie comme la moyenne pondérée par la fonction indicatrice des deux densités fluide et solide :

$$\rho = I\rho_{solide} + (1 - I)\rho_{fluide} \quad (1.2)$$

Lorsque les particules se déplacent, l'interface entre les deux phases est déplacée. Pouvoir localiser précisément la position de l'interface est primordial dans le formalisme mono-fluide. L'advection de la fonction indicatrice est régie par :

$$\frac{\partial I}{\partial t} + \mathbf{u}_b \cdot \nabla I = 0 \quad (1.3)$$

Où \mathbf{u}_b représente la vitesse de déplacement de l'interface. Pour résoudre l'équation précédente, la méthode de Front tracking est utilisée. Selon cette méthode, la frontière entre les deux phases est suivie par un maillage de surface mobile composé de marqueurs Lagrangiens connectés qui sont advectés par rapport à un maillage Eulérien fixe (voir Figure 1.4).

La vitesse barycentrique de l'interface \mathbf{u}_m est ensuite calculée numériquement à partir de :

$$\mathbf{u}_m = \frac{1}{\sum A_i} \sum A_i \mathbf{u}_i \quad (1.4)$$

où A_i et \mathbf{u}_i sont respectivement la surface et le vecteur vitesse associés au marqueur i du maillage Lagrangien. Les marqueurs sont ensuite déplacés avec la vitesse barycentrique :

$$\mathbf{x}_i^{n+1} = \mathbf{x}_i^n + \Delta t \mathbf{u}_m^{n+1} \quad (1.5)$$

Une fois les nouvelles positions des marqueurs x_i^{n+1} connues, le front est utilisé pour reconstruire la fonction indicatrice et pour mettre à jour les propriétés physiques locales en conséquence. Les difficultés habituellement soulevées par la méthode de suivi frontal, liées à la conservation de la masse et à la gestion de la fragmentation et de la coalescence des inclusions, sont absentes dans notre situation.

D'un point de vue eulérien, la contrainte de rigidité au sein de la phase solide peut être exprimée comme suit [107] :

$$\frac{1}{2} \left(\nabla \mathbf{u} + \nabla^T \mathbf{u} \right) = \mathbf{0} \quad (1.6)$$

Cette formulation est très pratique par rapport aux équations mono-fluide. Elle décrit une contrainte localisée pour le domaine rigide qui pourrait être directement imposée sur l'équation de conservation de la quantité de mouvement sans avoir besoin de connaître au préalable les vitesses du solide. En pratique, il est possible d'annuler le tenseur de déformation en imposant une valeur élevée pour μ à l'intérieur de la région solide par rapport au domaine fluide. Le comportement de corps rigide sera dans ce cas appliqué de manière asymptotique. Cette approche est appelée méthode de pénalité visqueuse [97, 16]. Cette stratégie présente l'avantage de simplifier grandement le couplage entre les phases solide et fluide, puisque le couplage est fait implicitement et l'inertie de la région solide est entièrement portée par le solveur fluide. Le champ de vitesse à l'intérieur du solide étant un champ sans divergence, l'équation de continuité est également automatiquement satisfaite. En ce qui concerne la modélisation de la viscosité dynamique dans les mailles traversées par l'interface diphasique, l'utilisation d'une moyenne harmonique est préférée à une moyenne arithmétique, car la moyenne harmonique satisfait mieux à la condition de continuité des contraintes à l'interface. Cependant, même avec cette stratégie, le rapport de viscosité peut occasionnellement être si élevé que des ajustements supplémentaires sont nécessaires. Par exemple, certains auteurs ont proposé de réduire le rayon des particules pour compenser cet effet [115]. Dans notre cas, nous avons préféré utiliser une fonction en escalier pour modéliser la viscosité équivalente à l'interface. L'application de la viscosité du fluide dans les mailles biphasiques permet en quelque sorte de réduire le diamètre hydraulique des particules. Le rapport de viscosité prescrit pour nos simulations varie entre 10^3 et 10^4 .

Pour ce qui est de la modélisation des collisions particule-particule et particule-paroi, une version modifiée de la méthode de modélisation combinée de Mohaghegh et al. 2019 [83] a été adoptée. Dans cette approche, la force de collision est modélisée sur la base d'un système masse-ressort sans amortisseur. Cette méthodologie permet de réduire le nombre de paramètres numériques en comparaison avec d'autres modèles de collision de la littérature [13, 12, 66, 26]. Pour tenir compte des pertes dissipatives liées au frottement fluide et aux collisions inélastiques, la raideur du ressort est ajustée en utilisant le coefficient de restitution pour obtenir la vitesse de rebond désirée à la fin de la collision, contrairement à d'autres modèles qui nécessitent souvent l'utilisation d'un modèle de lubrification et d'un modèle de force-déplacement impliquant un coefficient d'amortissement. Une particularité de cette approche réside dans le fait que la vitesse

de rebond des particules est connue avant même que l'impact ne se produise. Cela est dû au fait que le coefficient de restitution utilisé pour corriger la raideur du ressort est calculé à partir d'une corrélation expérimentale entre le coefficient de restitution et le nombre de Stokes à l'impact [99]. De plus, cette méthode permet d'étendre la durée de la collision, permettant ainsi de réaliser des simulations sur des durées prolongées. Les coefficients du modèle sont fournis explicitement, éliminant le besoin d'une solution itérative. Enfin, le nombre de paramètres numériques est réduit car aucun modèle de lubrification supplémentaire n'est requis.

Dans le passage suivant, les grandes lignes du modèle de collision sont exposées : Considérons une collision se produisant entre deux particules sphériques p et q ou entre la particule p et un mur. La force de contact \mathbf{F}_c agissant sur une particule pendant une collision est modélisée par un oscillateur harmonique comme :

$$\mathbf{F}_c = -k\delta_n \mathbf{n} \quad (1.7)$$

avec k est la raideur du ressort et δ_n la distance normale séparant les surfaces des sphères en collision donnée par :

$$\delta_n = \|\mathbf{x}_p - \mathbf{x}_q\| - (R_p + R_q) \quad (1.8)$$

où \mathbf{x}_p et \mathbf{x}_q sont les positions des centres de masse des particules p et q , R_p et R_q sont les rayons des particules. \mathbf{n} est le vecteur normal au plan de collision défini par :

$$\mathbf{n} = \frac{\mathbf{x}_p - \mathbf{x}_q}{\|\mathbf{x}_p - \mathbf{x}_q\|} \quad (1.9)$$

L'équation différentielle décrivant le mouvement du système est donnée par :

$$m_e \ddot{\delta}_n + k\delta_n = 0 \quad (1.10)$$

La raideur du ressort k a été dérivée par [13] dans le cas particulier d'une collision élastique :

$$k = m_e \left(\frac{\pi}{\tau_0} \right)^2 \quad (1.11)$$

où m_e est la masse effective et τ_0 est la durée de collision prescrite. Pour les interactions particule-particule, $m_e = m_p m_q / (m_p + m_q)$ avec m_p et m_q étant la masse des particules p et q respectivement. Si la collision se produit entre une particule p et un mur, alors $m_e = m_p$. La durée de collision étirée est prise comme un multiple N du pas de temps du solveur Navier-Stokes Δt :

$$\tau_0 = N\Delta t \quad (1.12)$$

Physiquement, les collisions sont inélastiques, ce qui signifie qu'une partie de l'énergie cinétique est dissipée pendant le contact. Même dans le scénario où la contrainte visqueuse est négligeable, une certaine énergie est encore dissipée sous forme de

vibrations dans le solide. Le coefficient de restitution sec e_d tient compte de cette dissipation d'énergie :

$$e_d = \frac{\Delta u_{reb,d}}{\Delta u_{imp,d}} \quad (1.13)$$

où $\Delta u_{reb,d}$ et $\Delta u_{imp,d}$ sont respectivement les vitesses relatives de rebond et d'impact des deux surfaces solides en collision dans l'absence de dissipation visqueuse du fluide (régime sec). Le coefficient de restitution sec du solide est une propriété physique directement liée aux propriétés élastiques du matériau. La valeur par défaut utilisée dans ce travail de thèse est $e_d = 0.97$. En régime humide (présence d'un fluide visqueux), la dissipation d'énergie est nettement plus élevée en raison de la dissipation visqueuse du fluide. [68, 120] (Figure 1.5) ont montré expérimentalement que le coefficient de restitution apparent ou effectif est fortement corrélé avec le nombre de Stokes St :

$$St = \frac{2 R_{eff} \Delta u_{imp} \rho_s}{9 \mu_f} \quad (1.14)$$

Dans cette équation, R_{eff} représente le rayon effectif, défini par $R_{eff} = R_p R_q / (R_p + R_q)$ dans le cas de la collision de deux particules, et $R_{eff} = R_p$ dans le cas d'une collision entre une particule et une paroi. Δu_{imp} correspond à la vitesse relative au moment de l'impact, ρ_s est la densité des particules, et μ_f est la viscosité dynamique du fluide.

La relation entre le coefficient de restitution effectif e et le nombre de Stokes St peut être exprimée comme le produit du coefficient de restitution sec constant et d'un coefficient de restitution "humide", e_w , dépendant du nombre de Stokes St . Typiquement, e_w varie de 0 à 1 :

$$e(St) = e_d e_w(St) = \frac{\Delta u_{reb}}{\Delta u_{imp}} \quad (1.15)$$

De manière similaire à [83], la vitesse de rebond nécessaire à la fin d'une collision est obtenue en utilisant la relation $e_w = \exp(-35/St)$ en tant que paramètre d'entrée du modèle. Le coefficient de restitution effectif de la collision est calculé en fonction du nombre de Stokes St avant l'impact et est utilisé pour ajuster la raideur du ressort dans l'Eq.4.36. Cette procédure élimine le besoin d'un modèle de lubrification ou d'un coefficient d'amortissement en tenant compte intrinsèquement de la dissipation d'énergie.

Il est à noter que le nombre de Stokes pré-collision est calculé au moment où les particules commencent à entrer en collision, ce qui signifie que l'effet de lubrification a déjà été sous-résolu, car l'espace entre les particules est inférieur à une cellule de grille. Par conséquent, le nombre de Stokes pourrait être surestimé. En pratique, l'énergie cinétique de la particule avant et après la collision est prescrite en utilisant le coefficient de restitution effectif. La différence entre les deux énergies correspond aux effets dissipatifs. Après avoir traduit cette différence en énergie potentielle, il peut être montré facilement que, pour obtenir la vitesse de rebond souhaitée, la raideur du ressort

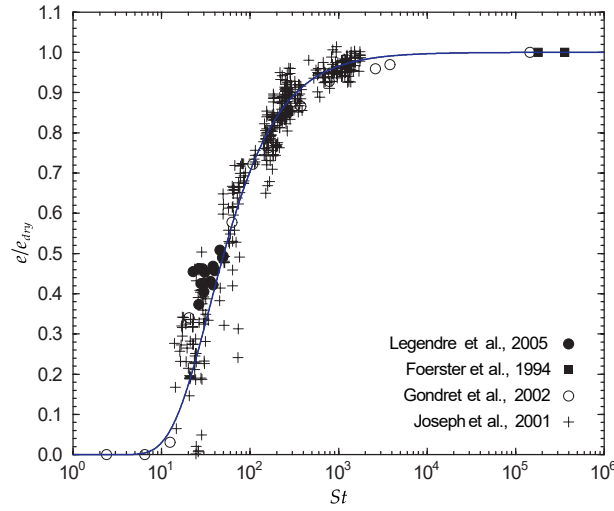


Figure 1.5: Adapté de [76]. Coefficient de restitution en milieu humide en fonction du nombre de Stokes St . Points de données de [68, 53, 75, 47].

doit être réduite d'un facteur e^2 pendant la phase de rebond (voir [83] pour plus de détails sur la dérivation). L'ajustement est effectué après que le chevauchement maximal des interfaces permis par la raideur du ressort soit atteint, et les particules commencent à se déplacer dans des directions opposées. La raideur du ressort est traitée comme une fonction définie par morceaux du produit scalaire $\Delta \mathbf{u} \cdot \mathbf{n}$ (Eq.4.49). Le changement de signe de ce dernier est utilisé pour déterminer précisément le moment où la réduction de la raideur est effectuée (voir Fig1.6):

$$k_i = \begin{cases} k_{imp} = m_e \left(\frac{\pi}{\tau_0} \right)^2 & \text{if } \Delta \mathbf{u} \cdot \mathbf{n} \leq 0 \\ k_{reb} = k_{imp} e^2 & \text{if } \Delta \mathbf{u} \cdot \mathbf{n} > 0 \end{cases} \quad (1.16)$$

La force de collision $\mathbf{F}_c = -k_i \delta_n \mathbf{n}$ est ensuite appliquée aux cellules purement solides dans le domaine de simulation (correspondant à une fonction indicatrice strictement égale à 0). Cela est fait à chaque pas de temps jusqu'à ce qu'il n'y ait plus de chevauchement entre les deux solides.

La distance δ_n (Eq. 1.8) entre les surfaces de chaque paire de particules p et q est calculée. Si $(\delta_n < 0)$, alors une collision est détectée et la force à appliquer à chacune de ces particules est calculée. Conformément à la troisième loi du mouvement de Newton, la force de réaction à appliquer à la particule q est d'intensité égale et de direction opposée à la force appliquée à la particule p :

$$\mathbf{F}_{c,p \rightarrow q} = -\mathbf{F}_{c,q \rightarrow p} \quad (1.17)$$

Les forces agissant sur la particule p sont additionnées et divisées par le volume V_p de la particule p . Le résultat est ensuite appliqué aux cellules solides appropriées grâce à

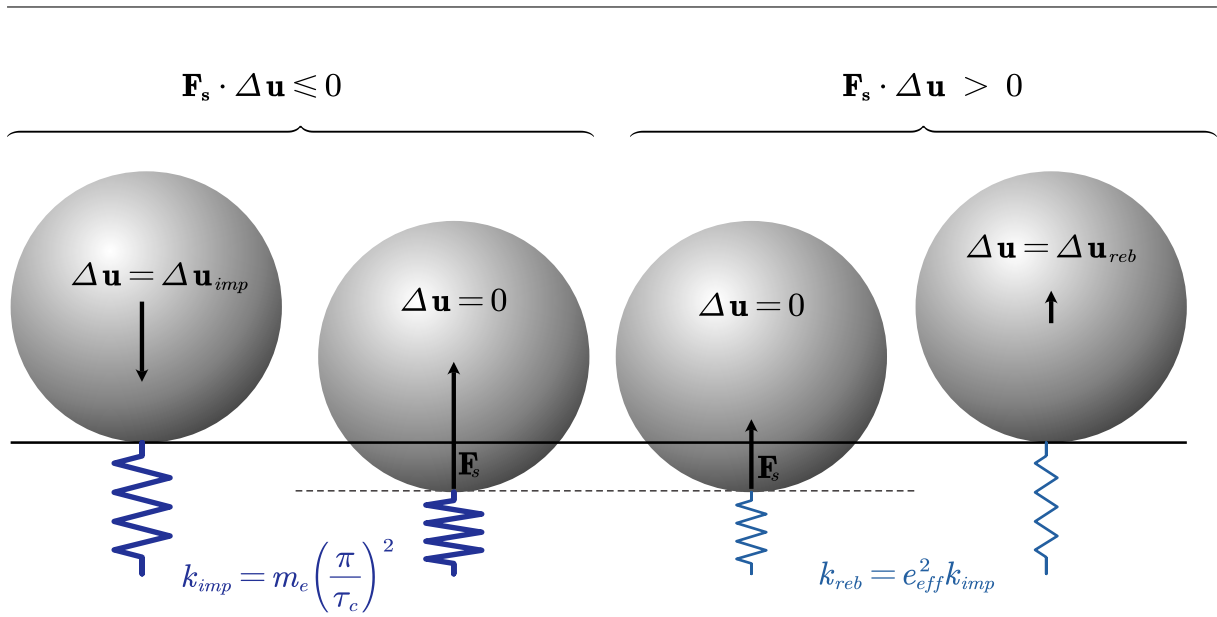


Figure 1.6: Diagramme explicatif du modèle de collision.

la fonction indicatrice de phase :

$$\mathbf{c}^{n+1} = I^n \sum_q \frac{\mathbf{F}_{\mathbf{c}, q} \rightarrow p^{n+1}}{V_p} \quad (1.18)$$

Les forces sont calculées à chaque pas de temps jusqu'à ce qu'aucun chevauchement ne soit observé ($\delta_n \geq 0$). L'intégration temporelle de la force de collision est effectuée par un schéma de temps Euler semi-implicite (SIE) pour éviter les divergences numériques causées par le schéma Euler explicite :

$$\mathbf{F}_{\mathbf{c}, q} \rightarrow p^{n+1} = -k_i \delta n^{n+1} \mathbf{n} \quad (1.19)$$

où \mathbf{n} est donné par Eq. 4.38 et δn^{n+1} est la distance séparant la surface des deux particules en collision évaluée au temps $n + 1$:

$$\delta n^{n+1} = \left| (\mathbf{x}p^n - \mathbf{x}q^n) + \Delta t (\mathbf{u}p^n - \mathbf{u}q^n) \right| - (R_p + R_q) \quad (1.20)$$

Dans le cas d'une collision mur-particule, une particule virtuelle identique à la particule p est générée derrière le mur, comme proposé dans [50]. Cette stratégie permet de traiter le calcul de la force de collision dans la situation de collision mur-particule de manière identique au scénario particule-particule.

Enfin, les équations de Navier-Stokes sont résolues par une méthode de prédiction/-correction sur une grille cartésienne échelonnée avec une discrétisation en volume fini Marker-And-Cell (MAC) [92]. Pour alléger les contraintes numériques causées par les hauts rapports de viscosité R_μ requis par la méthode de pénalité visqueuse, l'évaluation du terme source diffusif est implicite et calculée avec un algorithme d'Uzawa.

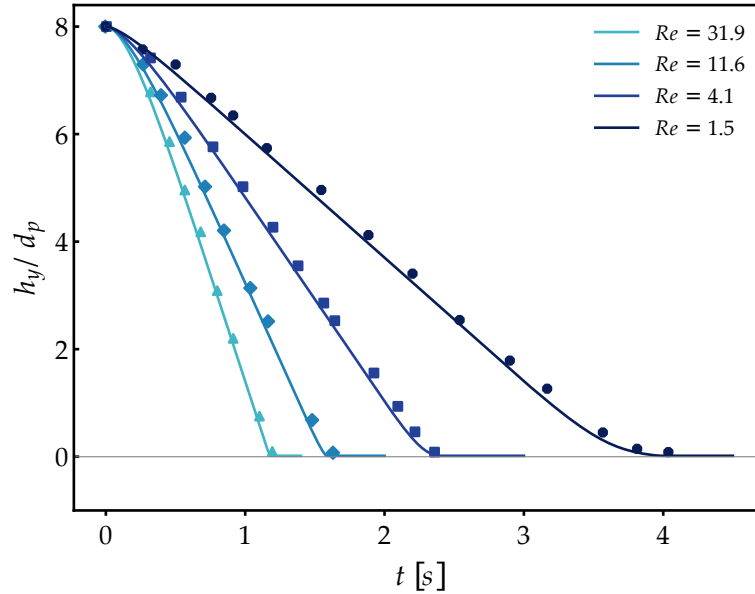


Figure 1.7: Profile de la hauteur normalisée h_y/d_p en fonction du temps pour une particule en sédimentation. Symboles : données expérimentales de Cate et al. [18], lignes : simulations.

Validation et simulations

la méthodologie de simulation présentée précédemment est validée en reproduisant les cas tests de [18] et [53]. Le premier cas test correspond à la sédimentation d'une particule sphérique dans un conteneur contenant un fluide au repos à différents nombres de Reynolds. Les nombres de Reynolds, $Re_t = \rho_f V_t R_p / \mu_f$ basés sur la vitesse terminale V_t considérée dans cette étude sont 1.5, 4.1, 11.6, and 32.2.

Ces conditions sont obtenues en ajustant le type de fluide à l'intérieur du conteneur. Les dimensions du conteneur sont de 0.10 m \times 0.16 m \times 0.10 m dans les directions x, y et z, respectivement.

La gravité $g = 9.81 \text{ m} \cdot \text{s}^{-1}$ agit dans la direction négative de y. La position de lâcher du centre de gravité de la particule est située 12.75 cm au-dessus du fond du réservoir et est centrée dans les directions x et z. La densité de la particule solide est $\rho_p = 1120 \text{ kg/m}^3$. Des conditions aux limites de non-glissement sont imposées sur les parois du domaine, tandis que des conditions aux limites de sortie (avec une pression de référence nulle) sont appliquées à la limite supérieure. Initialement, le fluide est au repos dans le domaine. Le rapport de viscosité est fixé à $R_\mu = 1000$ pour les quatre cas. Enfin, un pas de temps d'intégration égal à $\Delta t = 10^{-4} \text{ s}$ est utilisé pour le solveur de pression.

Pour réaliser les simulation sur les figures ultérieures, une moyenne harmonique et une résolution de grille de $R_\Delta = 15$ ont été employées pour les quatre nombres de Reynolds. Les résultats de ces simulations sont comparés avec les résultats expérimentaux de ten Cate et al. sur les figures 5.2 et 5.3. Comme le montre la comparaison, la dynamique

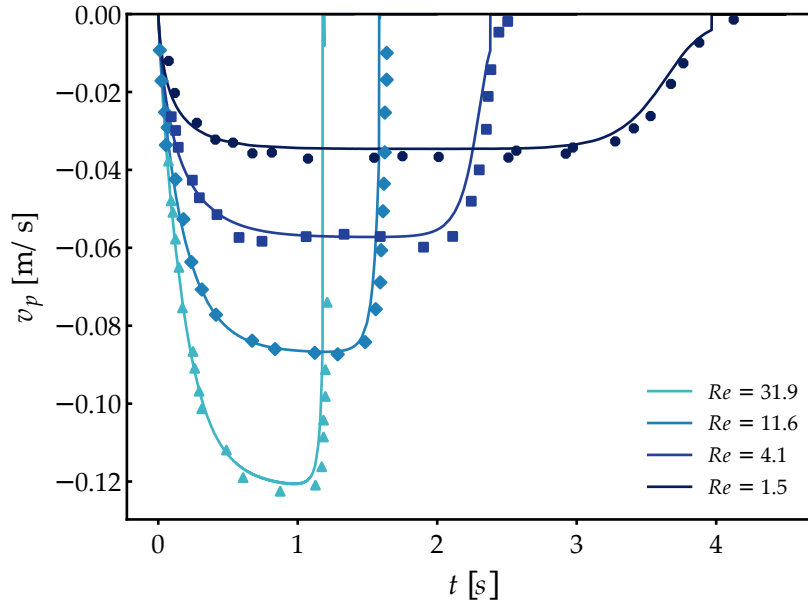


Figure 1.8: Profile de la vitesse de particule v_p en fonction du temps pour une particule en sédimentation. Symboles : données expérimentales de Cate et al. [18], lignes : simulations.

d'une particule en sédimentation à des nombres de Reynolds allant jusqu'à 31.9 est fidèlement capturée par nos simulations. La section suivante sera consacrée à une validation supplémentaire du modèle de collision, spécifiquement dans le contexte du régime de rebond. Pour valider notre méthode, nous reproduisons les données expérimentales de Gondret, Lance, and Petit [53].

La configuration de la simulation met en jeu une particule en acier inoxydable qui est libérée dans un réservoir rempli d'huile de silicone RV10. Sous l'effet de la gravité, la particule accélère vers le fond du réservoir, entrant en collision à plusieurs reprises avec le fond de la boîte. L'évolution temporelle de la trajectoire et des profils de vitesse verticale a été simulée, et elle a été comparée aux données expérimentales. Les nombres de Stokes pour les rebonds successifs sont $St = 75, 41, 20,$ and 5 . La simulation est réalisée dans un domaine de $9 \text{ mm} \times 12 \text{ mm} \times 9 \text{ mm}$ avec une résolution de maillage de $R_\Delta = 16$. Le diamètre de la particule est $d_p = 3 \text{ mm}$ et le centre de la particule est positionné aux coordonnées $(4.5 \text{ mm}, 8.88 \text{ mm}, 4.5 \text{ mm})$. Les densités du fluide et du solide sont respectivement égales à 935 kg/m^3 and 7800 kg/m^3 . La viscosité du fluide est égale à $0.01 \text{ Pa} \cdot \text{s}$ et le rapport de viscosité est maintenu à $R_\mu = 1000$. Des conditions aux limites de non-glissement sont imposées sur toutes les parois du domaine, et le pas de temps est fixé à $\Delta t = 5 \times 10^{-5} \text{ s}$.

Les figures 1.9 et 1.10 montrent le comportement temporel de la distance normalisée de la particule par rapport au mur et sa vitesse de sédimentation. Les simulations utilisent à la fois la moyenne harmonique et la modélisation en escalier pour calculer la viscosité dans les cellules traversées par l'interface. Les deux méthodes montrent une forte concordance avec les données expérimentales pendant la phase initiale de

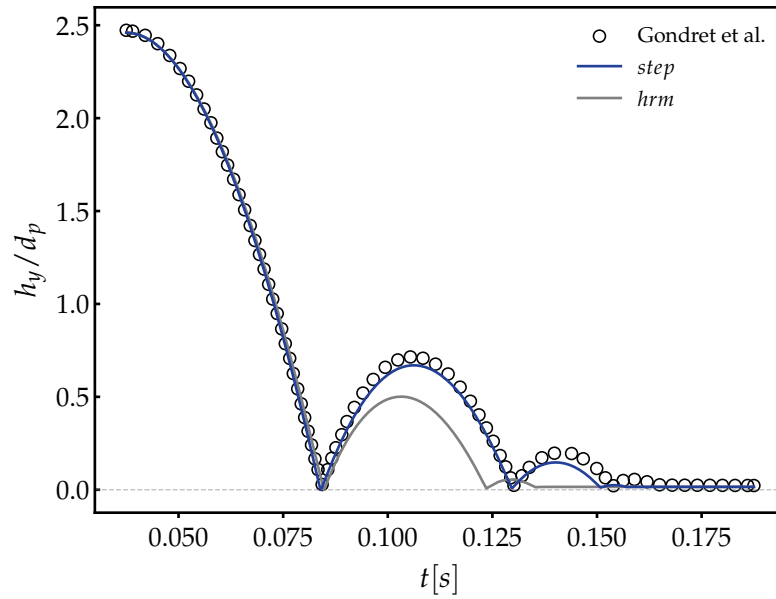


Figure 1.9: Profile de la hauteur normalisée h_y/d_p en fonction du temps. Symboles : données expérimentales de Gondret, Lance, and Petit [53], lignes : simulations

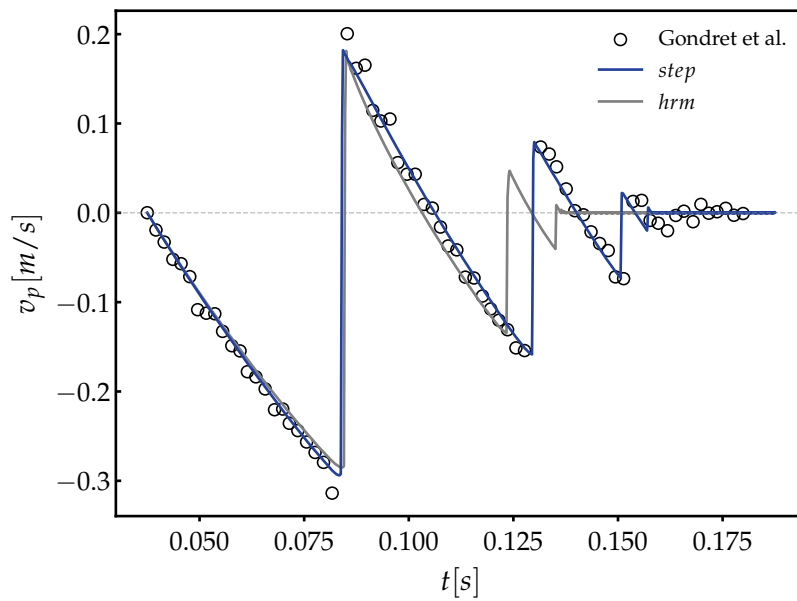


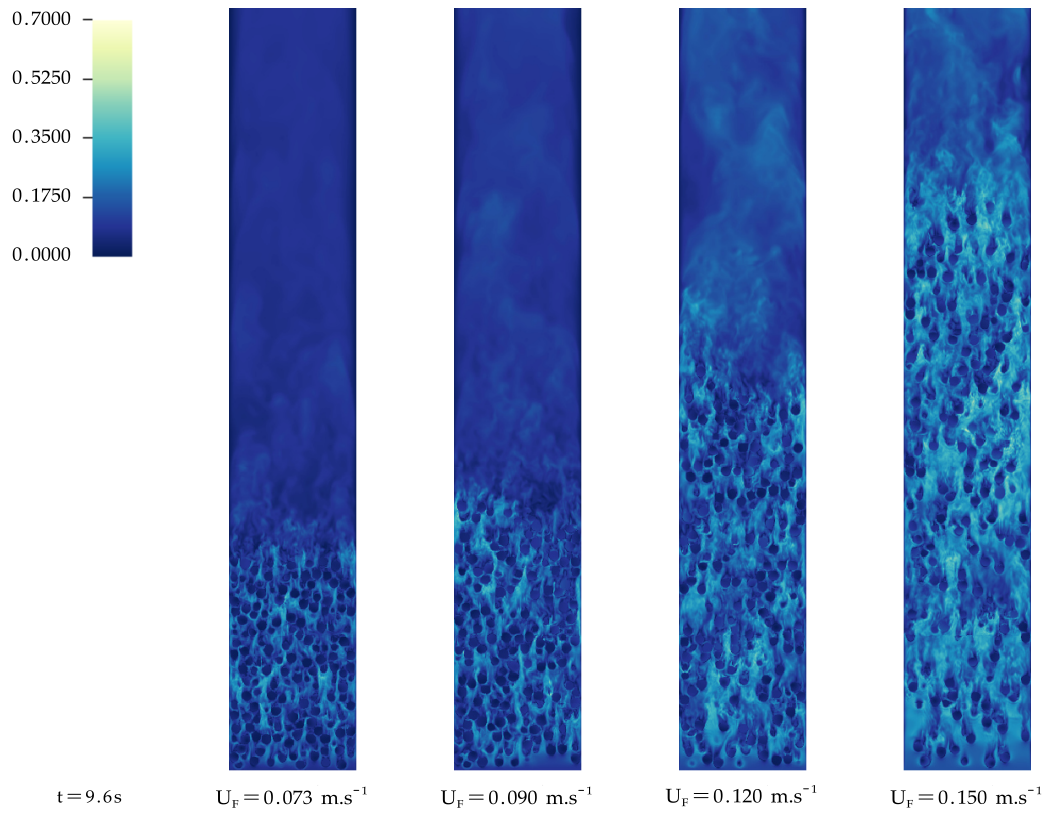
Figure 1.10: Profile de la vitesse de particule v_p en fonction du temps. Symboles : données expérimentales de Gondret, Lance, and Petit [53], lignes : simulations actuelles

sédimentation, fournissant une représentation correcte de la trajectoire de la particule. Cependant, des incohérences deviennent apparentes après le premier rebond. En particulier, après la première interaction de la particule avec son sillage, la force de traînée est surestimée, entraînant une réduction des hauteurs de rebond. L'utilisation de la méthode de fonction d'étape pour le calcul de la viscosité améliore les résultats de la simulation. Ce faisant, nous diminuons numériquement le diamètre hydrodynamique de la particule, réduisant ainsi la traînée. Au fur et à mesure que la simulation progresse et que la particule rebondit plusieurs fois, de légères déviations entre les données simulées et expérimentales émergent. Ces écarts entraînent une sédimentation plus précoce de la particule simulée par rapport à son homologue réel.

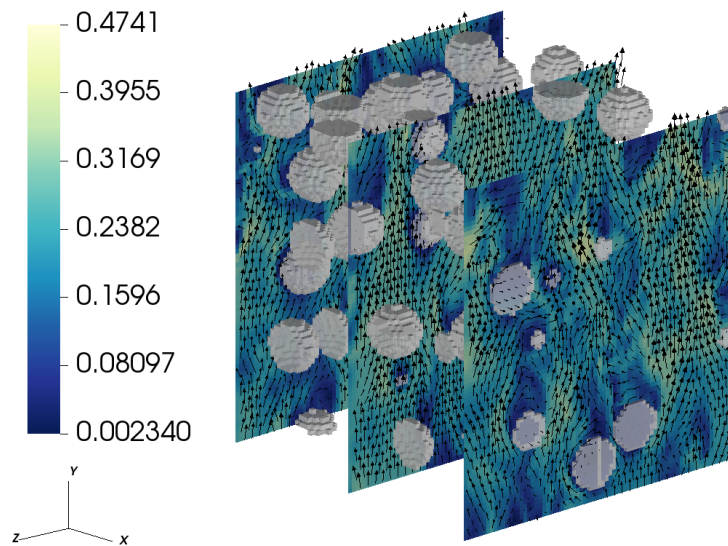
Dans la section suivante, nous évaluerons la performance de la méthode dans le cas plus complexe d'un lit fluidisé avec plus de 2000 particules en interaction. Pour ce faire, nous présentons les résultats de simulation d'un système de 2100 particules à quatre vitesses de fluidisation différentes. Les paramètres de la simulation sont basés sur l'expérience de Aguilar-Corona [1], qui a étudié la fluidisation de particules sphériques monodispersées de Pyrex de 6 mm ($\rho_p = 2230 \text{ kg/m}^3$) dans une solution aqueuse concentrée de thiocyanate de potassium ($\rho_f = 1400 \text{ kg/m}^3$, $\mu_f = 3.8 \times 10^{-3} \text{ Pas}$). La vitesse terminale de la particule est $V_t = 0.24 \text{ m/s}$.

Le dispositif expérimental a été spécialement conçu pour servir de référence lors de la validation numérique, car l'indice de réfraction des deux phases a été choisi pour permettre des techniques de mesure optique non intrusives. Ces techniques sont utilisées pour caractériser le champ de vitesse du fluide et l'agitation des particules. La même configuration a déjà été étudiée numériquement par Ozel et al. [86], en utilisant la méthode de pénalité tensorielle implicite de Vincent et al. [115], avec une résolution de maillage de $R_\Delta = 12$. Le nombre de Reynolds basé sur la vitesse terminale est $Re_t = 530$ et le nombre de Stokes associé est $St_t = 94$. Nous visons à évaluer la performance de notre approche en reproduisant la configuration numérique d'Ozel pour quatre vitesses de fluidisation différentes : $U_F = 0.15 \text{ m/s}$, 0.12 m/s , 0.09 m/s , 0.073 m/s . Le domaine de calcul est de dimension $0.072 \text{ m} \times 0.648 \text{ m} \times 0.072 \text{ m}$, et correspond à la même surface de section transversale expérimentale. Pour maintenir la cohérence avec l'étude originale, nous avons également imposé une résolution de maillage de $R_\Delta = 12$, qui est légèrement plus grossière que la résolution utilisée dans les cas précédents, mais est considérée comme un équilibre juste entre coût computationnel et précision. De plus, le rapport de viscosité est fixé à $R_\mu = 1 \times 10^4$. Pour accélérer la phase transitoire initiale, le lit de particules a été conçu pour correspondre étroitement à la hauteur de lit obtenue dans le cas numéro 3 de [86] (où $U_F = 0.12 \text{ m/s}$ et la hauteur de lit est atteinte dans le régime stationnaire).

La Figure 1.11 fournit à la fois une vue macroscopique et microscopique de la dynamique du lit fluidisé. La figure du haut illustre l'intensité de la vitesse au plan central du domaine à $t = 9.6$ secondes, couvrant diverses vitesses de fluidisation U_F . Notamment, les vitesses à l'intérieur des particules sont significativement plus faibles que dans le fluide environnant. À mesure que U_F augmente, nous observons l'émergence de



(a) Contour de l'amplitude de la vitesse dans un plan centré sur le domaine pendant le régime établi



(b) Vecteur vitesses dans la région centrale inférieure du cas où $U_F = 0.120 \text{ m/s}$

Figure 1.11: Visualisation des structures de l'écoulement

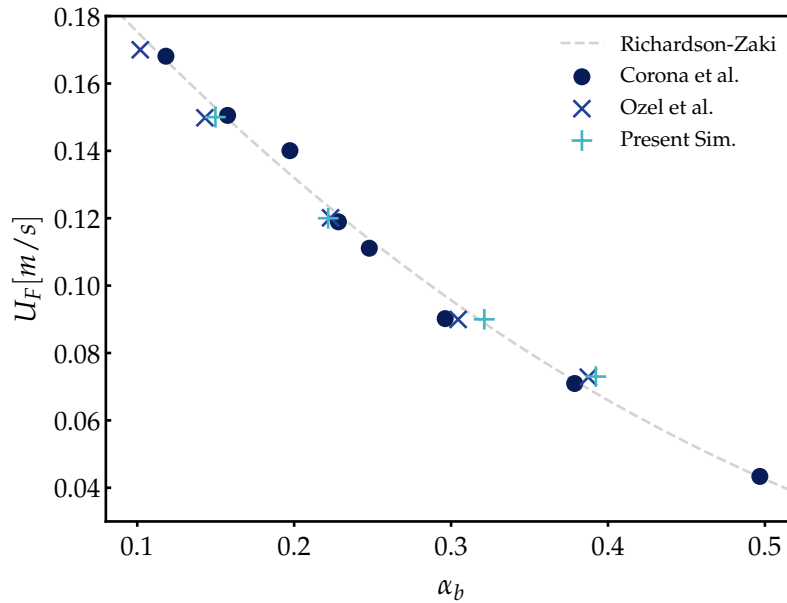


Figure 1.12: Vitesse de fluidisation en fonction de la concentration solide du lit.

structures pseudo-turbulentes plus grandes se formant dans le sillage des particules. En se concentrant sur le niveau microscopique, le tracé vectoriel de la figure du bas révèle la formation de couches limites dynamiques autour de chaque particule. La vitesse du fluide passe de la vitesse de la particule à sa surface à des valeurs dépassant la vitesse de fluidisation plus loin dans le domaine. La distribution non uniforme des particules est également évidente, conduisant à des disparités de vitesse entre les régions riches en particules et les régions pauvres en particules. À mesure que les particules se déplacent à travers le fluide, leurs couches limites perturbent l'écoulement, créant des zones de sillage à faible vitesse juste derrière elles. L'interaction et la superposition de ces sillages de plusieurs particules ajoutent une couche de complexité à la dynamique de l'écoulement.

Une étape importante dans la validation du lit fluidisé est l'établissement de la loi de fluidisation. Les fractions volumiques moyennes du lit sont affichées dans la Figure 5.15 en fonction de la vitesse de fluidisation. Les résultats sont comparés avec les données expérimentales de Aguilar-Corona [1], les résultats numériques de [86], et la corrélation empirique proposée par Richardson and Zaki [96] avec $n = 2.4$ et $U_{F0} = 0.24$ m/s comme suggéré dans Aguilar-Corona [1]. D'autres quantités importantes qui capturent bien la dynamique microscopique du lit sont le coefficient d'anisotropie et l'énergie cinétique totale. Ces quantités sont tracées en fonction de la fraction volumique dans Fig. 5.17a. D'après le graphique, nous observons que les valeurs obtenues sont légèrement inférieures à celles de [86]. Cependant, nous constatons également qu'il n'y a pas de dépendance du coefficient d'anisotropie, k_{anis} , sur la fraction volumique moyenne des particules. Ceci est vrai sauf pour le dernier cas, qui correspond à la vitesse de fluidisation la plus élevée de $U_F = 0.15$ m/s. Des tendances similaires sont observées pour l'énergie cinétique. Enfin, cette analyse démontre que l'approche développée

au cours de cette thèse permet de simuler un lit fluidisé solide-liquide avec la même précision que [86, 115].

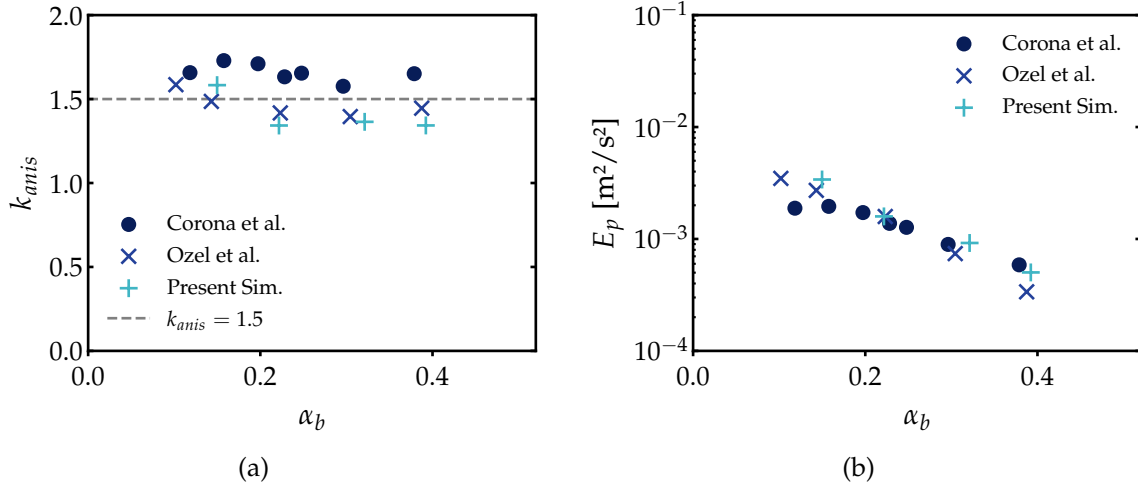


Figure 1.13: Coefficient d’anisotropie des fluctuations de la vitesse des particules en fonction de la concentration solide du lit.

Conclusion

Dans le contexte de cette thèse, des modifications conséquentes ont été apportées à l’algorithme de suivi frontal (front tracking) de TrioCFD pour réaliser des simulations numériques directes d’écoulements denses de fluides-particules.

En appliquant la technique de pénalisation visqueuse au formalisme monofluide afin de traiter les contraintes de rigidité, nous avons réussi à maintenir une interaction précise entre les phases solide et fluide, sans avoir à recourir à des termes de forçage supplémentaires. De plus, l’utilisation d’une moyenne harmonique et d’une fonction en escalier pour calculer la viscosité équivalente dans les cellules traversées par une interface diphasique s’est avérée efficace pour calibrer le diamètre hydraulique lorsque le maillage de simulation ne pouvait pas être suffisamment raffiné pour des raisons de coût. La gestion des interactions à courte portée entre les particules a été réalisée grâce à un modèle de collision combiné, permettant de prendre en compte la dissipation visqueuse et inélastique.

La validation de notre méthode de simulation par rapport à des références expérimentales a démontré sa fiabilité, avec une bonne concordance avec des références expérimentales, notamment dans les cas de simulation du mouvement de chute en présence d’un fluide visqueux et de la trajectoire de rebond de particules lors d’impacts contre une paroi verticale. Enfin, cette méthode a permis de simuler avec succès des écoulements

granulaires denses comptant plus de 2000 particules, reproduisant ainsi les résultats expérimentaux avec une bonne précision.

CONTENTS

Acknowledgements	iii
1 Résumé	v
Contents	xxiv
List of Figures	xxix
List of Tables	xxxiii
2 Introduction	1
2.1 Context	2
2.1.1 Concentrated solar power	3
2.1.2 Particle-based HTF	6
2.2 The Challenge posed by Particle Fluid flows	9
2.3 Numerical Modeling of fluid particules flows	11
2.3.1 Multiscale modeling approach	14
2.4 Thesis Objectives	15
3 Fundamental concepts on the physics of fluid-particle flows	17
3.1 Key parameters and adimensional numbers	18
3.1.1 Phase coupling	21
3.1.2 Fluidization	22
3.2 Fluid-Particles Interactions Modeling	24
3.2.1 Solid Phase Equations	25

3.2.2	Body Forces	26
3.2.3	Hydrodynamic Forces	27
3.2.4	Transient Forces	30
3.3	Numerical methods for BF-PRDNS	32
3.3.1	Immersed Boundary Methods	32
3.3.2	Distributed Lagrange Multiplier	33
3.3.3	Viscous Penalty Methods	34
3.3.4	Lattice Boltzman Methods	35
3.4	Particle-Particle Interactions Modeling	35
3.4.1	Lubrication modeling	35
3.4.2	Direct Contact Modeling	36
3.4.3	Cohesive Forces	45
4	Numerical Method	47
4.1	Presentation of the TrioCFD Framework	48
4.2	Deriving the One-Fluid Formulation	48
4.2.1	Two-fluids equations derivation	49
4.2.2	One-fluid equations derivation	53
4.2.3	Advection of the interface: The front-tracking method.	55
4.2.4	Solid Rigidity Constraint: Viscous Penalization	57
4.2.5	Modeling of the one-fluid physical properties at the interface	57
4.3	Particle-particle interactions: Collision modeling	58
4.3.1	Particle-particle collisions	59
4.3.2	Time integration of the collision force	62
4.3.3	Particle-wall collisions	62

Contents

4.4	Numerical implementation	63
4.4.1	The projection method	64
4.4.2	Solving the advection-diffusion problem	65
4.4.3	Solving the degenerate Stokes problem	68
4.5	Complete Algorithm	70
5	Numerical Simulations Results	71
5.1	Hydrodynamic validation: Sedimentation of a solid particle in a finite size domain	72
5.2	Collisional response validation: Normal collision of a particle with a planar wall	75
5.3	Particle resolved direct numerical simulation of a 2100 liquid–solid fluidized bed	78
5.3.1	Solid Phase Statistics	81
6	Conclusions and future work	89
	Bibliography	93
	Abstract / Résumé	103

LIST OF FIGURES

1.1	Solar energy conversion technologies.	vi
1.2	Représentation du récepteur solaire à particules en écoulement vertical .	vii
1.3	(a) Illustration du caractère multi-échelle des écoulements fluide-particules.	ix
1.4	Représentation graphique des maillages de résolution (a) maillage fixe, (b) maillage mobile.	xi
1.5	Adapté de [76]. Coefficient de restitution en milieu humide en fonction du nombre de Stokes St . Points de données de [68, 53, 75, 47].	xv
1.6	Diagramme explicatif du modèle de collision.	xvi
1.7	Profile de la hauteur normalisée h_y/d_p en fonction du temps pour une particule en sédimentation. Symboles : données expérimentales de Cate et al. [18], lignes : simulations.	xvii
1.8	Profile de la vitesse de particule v_p en fonction du temps pour une particule en sédimentation. Symboles : données expérimentales de Cate et al. [18], lignes : simulations.	xviii
1.9	Profile de la hauteur normalisée h_y/d_p en fonction du temps. Symboles : données expérimentales de Gondret, Lance, and Petit [53], lignes : simulations	xix
1.10	Profile de la vitesse de particule v_p en fonction du temps. Symboles : données expérimentales de Gondret, Lance, and Petit [53], lignes : simulations actuelles	xix
1.11	Visualisation des structures de l'écoulement	xxi
1.12	Vitesse de fluidisation en fonction de la concentration solide du lit. . . .	xxii
1.13	Coefficient d'anisotropie des fluctuations de la vitesse des particules en fonction de la concentration solide du lit.	xxiii
2.1	Examples of fluid-particles flows	2
2.2	Solar energy conversion technologies.	4
2.3	Overview of the three generation of CSP technologies [59]	5

List of Figures

2.4	Particle-based HTF systems	7
2.5	(a) Off-sun UBFB experimental setup. (b) Wall slug. (c) Axisymmetric slug. (d) Flow regime evolution with tube height.	8
2.6	(a) Multiscale character of granular flows. (b) High speed camera characterization of the granular flow.	9
2.7	Overview of simulation methods in fluid-particle flows.	12
2.8	Two types of Direct Numerical Simulation	14
2.9	Multiscale modeling approach.	15
3.1	Adapted from [76]. Wet coefficient of restitution, as a function of the Stokes number St . The solid line is the best fit of the data points of [68, 53, 75, 47]	20
3.2	Interphase coupling. Based on [42, 112]	22
3.3	Geldart's powder classification.	23
3.4	Illustration of fluidization regimes.	24
3.5	Drag coefficient for an incompressible flow over a smooth sphere as a function of Reynolds number, Cheng [20] correlation, Di Felice [33] correlation, and Schiller-Naumann correlation	28
4.1	Illustration of mixed method FT/VOF in TrioCFD	48
4.2	Biphasic control volume.	49
4.3	Graphical representation of resolution meshes (a) fixed mesh, (b) moving mesh	56
4.4	(a) Phase indicator schematic for the Front Tracking algorithm: purely solid cells (dark grey), purely fluid cells (white), and interface-crossed cells or mixed cells (gradient grey based on solid volume fraction). (b) Intersection of the Lagrangian and Eulerian meshes, demonstrating the determination of volume fractions from their relative positioning.	57
4.5	Explanatory diagram of the collision model.	61
4.6	(a) Control volume for the pressure calculation. (b) Control volume for the x-direction velocity calculation. (c) Control volume for the y-direction velocity calculation.	66

List of Figures

5.1	Time evolution of the simulated (a) vertical position and (b) vertical velocity for the case 1.4, $Re = 31.9$ as a function of mesh resolution and mixed cells viscosity modeling. Dashed line: resolution of 15 grid cells per diameter; continuous line: resolution of 30 grid cells per diameter. Blue line: harmonic averaging; gray line: arithmetic averaging. Vertical position normalized with the particle diameter.	73
5.2	Time histories of the normalized gap height h_y/d_p for a particle settling in a small container. Symbols: experimental data of Cate et al. [18], lines: present simulations	74
5.3	Time histories of the Settling Velocity v_p for a particle settling in a small container. Symbols: experimental data of Cate et al. [18], lines: present simulations	74
5.4	Time histories of the normalized gap height h_y/d_p . Symbols: experimental data of Gondret, Lance, and Petit [53], lines: present simulations	76
5.5	Time histories of the y-component of the particle velocity v_p . Symbols: experimental data of Gondret, Lance, and Petit [53], lines: present simulations	76
5.6	3D views of the particles' position distribution in the domain at $t = 0$ s and 9.6 s for the four fluidization velocities tested.	78
5.7	Fluid flow structure visualization.	80
5.8	Time evolution of the particle average streamwise velocity component, y-direction	81
5.9	Time evolution of the particle average transverse velocity component, continuous line x-direction, dashed lines z-direction	82
5.10	Time evolution of the particle velocity variance	83
5.11	Anisotropy coefficient	83
5.12	Fluctuating kinetic energy	84
5.13	Time-averaged profile of solid volume fraction	85
5.14	(a): Time evolution of maximum axial particle position at different fluidization velocities: $U_F = 0.073$ m/s, 0.090 m/s, 0.120 m/s, and 150 m/s. The continuous lines represent the average mean value of y_{max} over the range $t = [5 \text{ s}, 10 \text{ s}]$ (b) Box plot of the distribution of y_{max} (m). The box represents the interquartile range (IQR), the line inside the box is the mean, the whiskers extend to the minimum and maximum values.	86

List of Figures

5.15	Fluidization velocity with respect to the bed solid concentration.	86
5.16	Variance of axial (a) and transverse (b) particle velocity with respect to the bed solid concentration.	87
5.17	Anisotropy coefficient of the particle velocity fluctuations as a function of the bed solid concentration	88

LIST OF TABLES

3.1	Comparison of numerical integration methods	44
4.1	Term expression for the equation balance	50
4.2	Numerical parameters for the collision model in the case of a collision between two identical particles, and a particle-wall collision.	63
5.1	Physical parameters for a spherical particle settling in viscous fluid . . .	72

2

INTRODUCTION

2.1. Context



Figure 2.1: (a) Sediment plume of the Rhône river in France. Credit: European Union, Copernicus Sentinel-2 imagery. (b) Eruption of the Hunga Tonga-Hunga Ha’apai volcano. (c) Sandstorm near the city of Djelfa, Algeria. (d) Pneumatic transport of grains. (e) Pharmaceutical fluidized bed coating machine.

2.1 Context

Fluid-particle flows, also known as particle-laden flows, represent a significant subclass of multiphase flows. As the name implies, these flows are characterized by the simultaneous presence of two distinct phases: a continuous fluid phase either gas or liquid, and a dispersed particulate phase that is transported by the fluid phase.

A distinguishing characteristic of fluid-particle flows is the intense interaction between the fluid and particulate phases. This interaction is marked by a continuous and intricate exchange of momentum - and depending on the physics of the flow energy and mass - across the interfaces that separate the two phases. This complex interplay and the resulting coupling of phases give rise to a multitude of captivating phenomena that are unique to fluid-particle flows, and set them apart from their single-phase counterparts in a profound manner. Fluid-particle flows are not only intellectually engaging but also practically significant. These flows are omnipresent across diverse strata of natural phenomena and industrial application, with instances ranging from common daily occurrences to highly specialized technological applications [112].

In the environmental domain, these flows are instrumental in geological processes such as soil erosion and sediment transport in rivers. Here, soil particles, along with sand, silt, and rocks, are transported by rainwater, continuously reshaping the landscapes over time. Additionally, fluid-particle dynamics extend into the atmospheric domain with

2.1. Context

phenomena such as the dispersion of dust during storms and the spread of volcanic ash during volcanic eruptions (see Fig. 2.1). They also play a crucial role in the field of microbiology where biological entities like viruses, bacteria, and nutrients can be viewed as particles suspended in biological fluids such as blood or lymph. This fluid-particle interaction is a fundamental aspect of how these entities move, interact, and distribute within the host organism. A notable example is the spread of the SARS-CoV-2 virus, which has caused the COVID-19 pandemic.

In the industrial and technological landscape, fluid-particle flows are integral to numerous processes across a vast array of sectors. For instance, the pharmaceutical industry employs these flows in processes like granulation, where fine particles are bound together in the presence of a liquid to form larger granules. Similarly, in the mineral processing industry, hydraulic transport of ores involves creating a slurry where solid particles are transported by a fluid medium. Fluid-particle flows are also integral to operations of fluidized bed reactors in chemical engineering, which are essential for large-scale chemical processes such as catalytic cracking of petroleum.

Lastly, in the wake of the global climate crisis, the role of fluid-particle flows in renewable energy solutions has become increasingly significant, especially in Concentrated Solar Power (CSP) technology.

2.1.1 Concentrated solar power

Concentrated Solar Power (CSP) systems are a form of renewable energy technology designed to harness the sun's energy. Unlike the more broadly known photovoltaic (PV) systems, which convert sunlight directly into electricity via semiconductor materials, CSP systems work by focusing sunlight onto a small area to generate high-intensity heat, which is then converted to electricity through a thermal process. Both type of systems are displayed on Fig. 2.2.

At the core of CSP's working principle is the utilization of mirrors or lenses to concentrate a large area of sunlight into a focalized beam aimed at a reciver. This concentrated solar energy is first absorbed by the reciver and then used to heat up a working fluid. The heated fluid is then employed either dirctly or indirectly as a heatsource for alimenting a thermodynamic cycle for electric power generation [48].

There are four main CSP technologies, differentiated primarily by the geometry of their collectors: Parabolic Trough Collector (PTC), Linear Fresnel Reflector (LFR), Parabolic Dish Collector (PDC), and Solar Power Tower (SPT). [48] LFR and PTC fall under line-focusing systems. These systems harness sunlight by focusing radiation 60–100 times onto an absorber pipe. Commercially, these technologies often operate based on the Rankine cycle, with synthetic oil or steam serving as heat transfer fluids [84, 91].

On the other hand, SPT and PDC fall into the category of point-focusing central receiver

2.1. Context

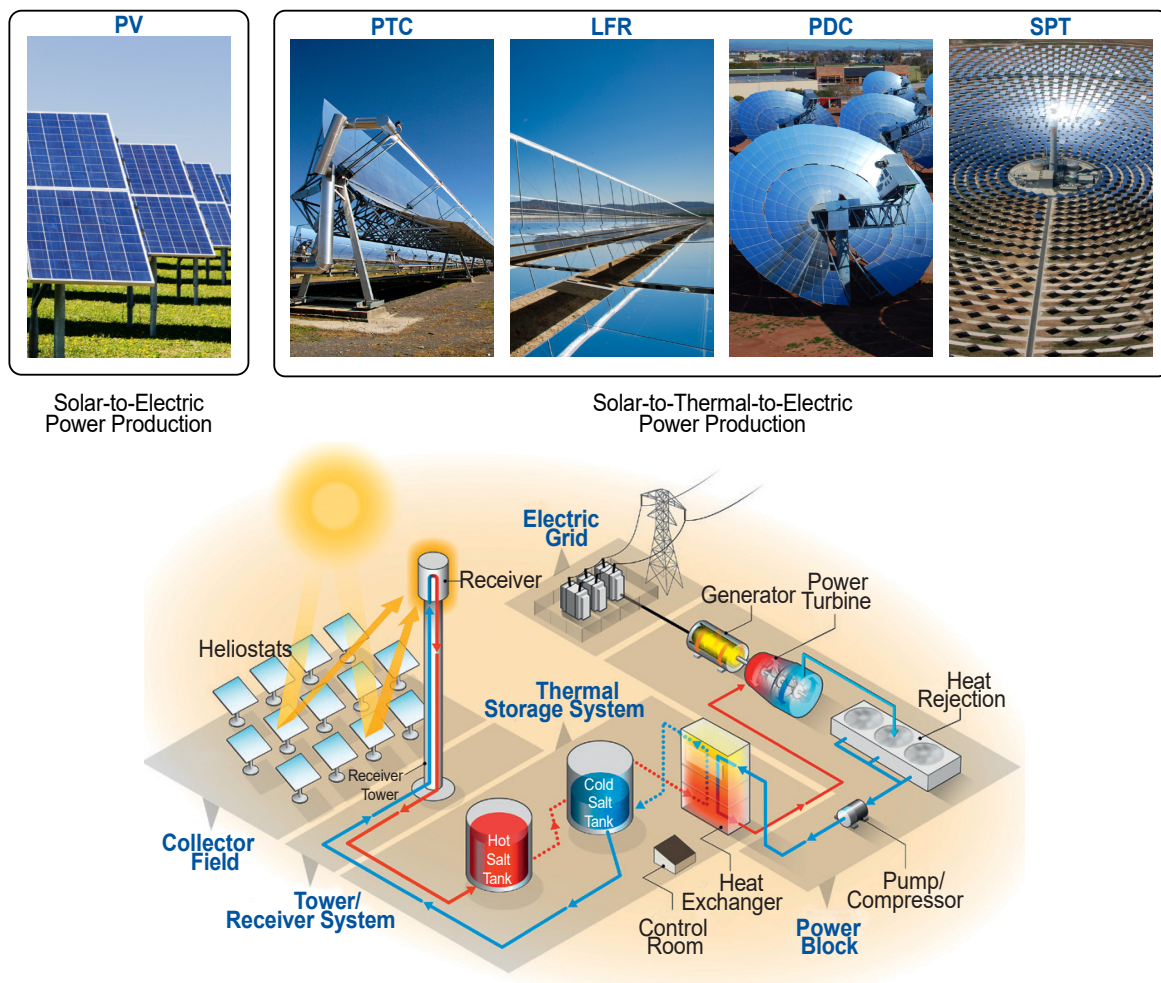


Figure 2.2: (Top) PV: Photovoltaic systems, PTC: Parabolic Trough Collector, LFR: Linear Fresnel Reflector, PDC: Parabolic Dish Collector, SPT: Solar Power Tower (Bottom) Concentrating solar power plant [84].

systems. Solar tower plants employ numerous heliostats that concentrate solar radiation up to 1000 times onto a central receiver. The dish-Stirling systems take the focusing aspect even further, where a dish-shaped mirror concentrates solar radiation up to 3000-fold into the receiver cavity of a Stirling engine [84].

Although the installed capacity of Concentrated Solar Power technologies is currently small compared to Photovoltaic and wind energy, these technologies exhibit significant growth potential for the future. CSP systems are expected to expand in parallel with the ever-increasing capacities of PV and wind energy, contributing to a more balanced, sustainable global energy mix [59]. . Indeed, the addition of renewable power sources that are controllable can be highly beneficial for offsetting the power fluctuations caused by the intermittent nature of PV and wind energy. In this regard, CSP systems, especially when coupled with Thermal Energy Storage (TES), can play a significant role in smoothing out the electricity supply-demand curve. This helps to ensure a steady and reliable electricity supply on the grid [59]. Furthermore, CSP systems also serve as

2.1. Context

excellent bulk electricity production systems in the 10-1000 MW range [84].

The interest in CSP technologies is clearly seen in the growth rates over the recent years. In 2019, the cumulative CSP capacity reached 6430 MWh_e, with an additional 3645 MWh_e under construction or development [59]. However, a major obstacle that hinders the large-scale commercialization of CSP is the substantial nominal levelized costs of electricity (LCOE_n). In 2018, it was found that some CSP plants could achieve an LCOE_n of around 10.9 c\$/kWh_e. However, the global weighted-average LCOE_n of CSP projects commissioned in 2018 was 18.5 c\$/kWh_e, which is significantly higher than those of photovoltaics (8.5 c\$/kWh_e) and onshore wind power (5.6 c\$/kWh_e) [59]. To enhance the competitive positioning of CSP, concerted efforts toward cost reductions and performance improvements across all subsystems in the CSP plant are highly desirable [59].

Based on the cycle efficiency and the thermodynamic cycle types, CSP technologies can be categorized into three generations as outlined in Figure 2.




Generation	1 st gen.	2 nd gen.	3 rd gen.
Receiver outlet temp.	~250 - 450 °C	~500 - 565 °C	~720 °C
Typical plant or technology	PTC, SPT, LFR 	PTC, SPT, LFR ~500 - 565 °C 	PDC 
Heat transfer medium	Oil or steam	Steam or salt	Gas
Thermal energy storage	Early designs: No or small Recent designs: Yes	Early designs: No or small Recent designs: Yes	No
Power cycle	Steam Rankine cycle	Stirling	Brayton cycle
Peak temp. of cycle	~240-440 °C	~480-550 °C	~720 °C
Design cycle eff.	~ 28-38%	~ 38-44%	~38%
Annual solar-electric eff.	~ 9-16%	~ 10-20%	~25%

Figure 2.3: Overview of the three generation of CSP technologies [59]

The first-generation CSP systems mainly utilized the Rankine cycle with an approximate cycle efficiency of 28-38%. The peak cycle temperature in these systems varied from a modest 240 °C to 440 °C. In this generation PTC, SPT and LFR technologies were primarily employed. Early designs lacked thermal energy storage, limiting the plant operations to sunlit hours. Nevertheless, more recent iterations have incorporated a two-tank sensible TES to ensure functionality during nighttime or overcast conditions. Despite the lower cycle efficiency, with an annual solar-electric efficiency of roughly 9-16%, first-generation CSP systems comprise the majority (around 80.2%) of the installed capacity, with PTC systems constituting about 76.5% of this figure [59].

The second-generation CSP plants employ an improved Rankine cycles, achieving an enhanced cycle efficiency of approximately 38-44%. The peak cycle temperature for these systems ascended to a range of 480 °C to 550 °C. These systems are almost always integrated with TES, where a binary nitrate serving dual purposes as the heat transfer fluid and thermal storage material. Although efficient, this solution encounters limitations related to minimum and maximum operating temperatures, as the salts solidify around 220-260 °C and suffer chemical degradation at temperatures beyond 565-600 °C [9]. These limitations hinder the overall performance and efficiency of the CSP system [126]. As a result, these plants can attain an annual solar-electric efficiency of about 10-20%. While PDC systems leveraging the Stirling cycle, with a typical cycle efficiency around 38%. Despite higher efficiency, PDC implementation has been restricted due to reliability issues such as gas leaks [59]. Economic analysis highlights that among all CSP systems, the second-generation Solar Power Tower can attain the lowest nominal levelized cost of electricity $LCOE_n$ at 10.90 c\$/kWh_e, thus reducing the cost difference with PV. This implies the potential of SPT systems to generate dispatchable electricity more cost-effectively than other CSP systems, supporting the trend of SPT systems constituting 61.51% of the total projected capacity [59].

Currently, third-generation CSP technologies are under intense research. The primary objective is to augment solar-electric efficiency to reduce $LCOE_n$. One key strategy involves enhancing cycle efficiency, where the Brayton cycle, with peak cycle temperatures exceeding 700 °C, is suggested. The cycle efficiency is also anticipated to exceed 50%. Various solar collection pathways employing diverse HTFs are being investigated, particularly focusing on high-pressure gases, high-temperature molten salts, and solid particles [9].

Specifically, solid particles present several benefits such as a broader operating temperature range and potential thermal stability, which could optimize the efficiency and performance of CSP systems [7].

2.1.2 Particle-based HTF

Particle-based HTFs have attracted considerable interest in the field of CSP, with various technologies being developed worldwide. Some notable examples include the "falling particle" receiver by Sandia National Laboratories in the United States [64], the top-irradiated draft tube fluidized bed developed by [78] and the centrifugal receiver developed by the German Aerospace Center (DLR) [41]. Another noteworthy development is the particle-in-tube solar receiver, also known as the Upflow Bubbling Fluidized Bed (UBFB), which is developed by the National Center for Scientific Research (CNRS) in France in collaboration with international partners. This research is part of the European projects "CSP-2" and "Next-CSP.[46, 61]". The receivers are illustrated in Fig. 2.4.

In the UBFB design, tubes are submerged within a vessel called the dispenser, which acts

2.1. Context

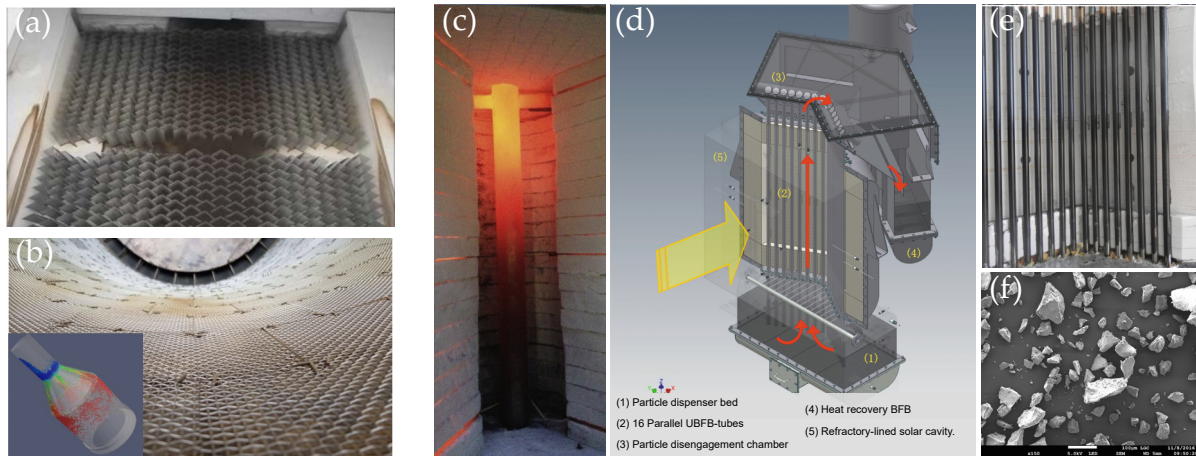


Figure 2.4: (a) Falling particles receiver. (b) Centrifugal receiver. (c) UBFB single tube on-sun experiment. (d) 3D schematics of the multi-tube UBFB solar receiver. (e) On-sun experiment of the multi-tube UBFB. (f) Microscopic magnification of powders used as HTF in the UBFB system.

as a feeder tank for the particles. When air is introduced into the dispenser under specific conditions it results in the suspension of the solid particles in the upward-moving air stream. The suspended mixture starts to exhibit characteristics similar to those of a liquid. For instance, the mixture can flow freely, conform to the shape of its container much like a fluid does, etc. This phenomenon is referred to as fluidization.

By applying pressure in the dispenser's freeboard, an upward particle flow in the tubes is achieved (See Fig. 2.5(c)). This type of flow is distinct from traditional risers, as it relies on a combination of carrier phase velocity and a pressure gradient between the dispenser and the collector, resulting in a wide range of solid volume fractions [55]. On-sun studies have shown that UBFB receivers can achieve heat transfer coefficients in the range of $800 \text{ W} \cdot \text{m}^{-2} \cdot \text{K}^{-1}$ to $1200 \text{ W} \cdot \text{m}^{-2} \cdot \text{K}^{-1}$, making them highly efficient under various irradiation conditions [8, 126, 128]. The UBFB concept offers several other technological benefits, including the use of a tubular receiver similar to those employed with molten salts and the ability to use the same medium as both HTF and storage material. Unlike molten salts, particles are not restricted to a specific working temperature range, allowing for high operation temperatures and more efficient heat-to-electricity conversion via high-temperature thermodynamic cycles [7]. Economically, UBFB technology can potentially reduce costs associated with the HTF and storage medium, as the selected particles can be significantly less expensive than molten salts [67]. Environmentally, the use of mineral particles can help decrease the power plant's overall environmental footprint [69].

Up to this point, experimental research on UBFB receivers has primarily focused on smaller-scale setups with tubes of small internal diameters and irradiated lengths ranging from 1 to 2 meters [8, 88, 11, 74], as well as longer tubes in ambient conditions up to 4 m. However, to successfully scale up the UBFB technology for commercial applications in the range of $10 \text{ MW}_{\text{th}}$ to $50 \text{ MW}_{\text{th}}$, it is necessary to employ taller tubes, preferably at least 6 m in height. Previous research has demonstrated that fluidization

2.1. Context

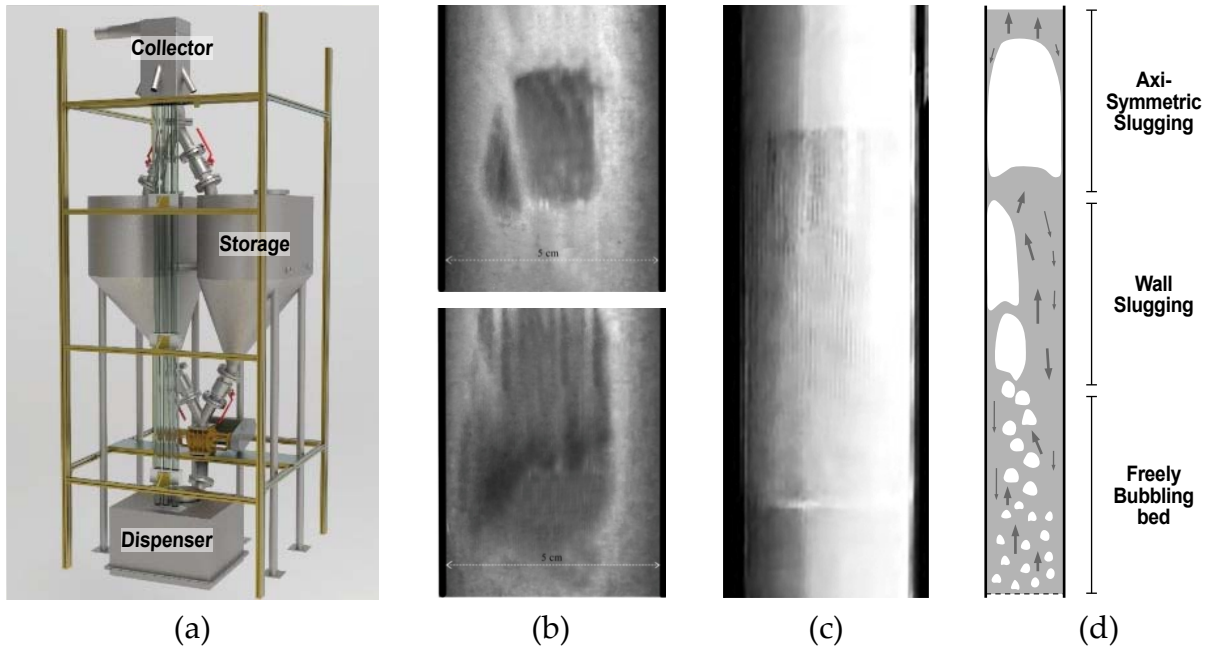


Figure 2.5: (a) Off-sun UBFB experimental setup. (b) Wall slug. (c) Axisymmetric slug. (d) Flow regime evolution with tube height.

regimes within the tubes are not homogeneous in relation to tube height [32, 100, 55]. At the base of the tubes, small bubble-like gas pockets begin to form as a result of increased gas pressure. These bubbles, in turn, entrain particles, carrying them upward. The phenomenon shares a visual similarity with boiling, leading to the term 'bubbling fluidization' regime. As we move further up the tube, these bubbles start to merge, creating larger 'slugs' of gas. The slugs are significant enough to encompass a substantial portion of the tube's diameter, although not its entirety. Given their size and shape, these slugs preferentially ascend near the tube's wall, leading to the term 'wall slug' regime. The transition from the bubbling regime to the wall slug regime notably takes place at around the 0.7 m mark. At greater elevations, these slugs progressively increase in size, eventually covering the full diameter of the tube at approximately 1.7 m. This critical point signals the transition from the wall slug regime to the 'axisymmetric slug' regime, where the slugs of gas occupy the central axis of the tube.

The thermal performance of the solar receiver is closely related to the hydrodynamics of the two-phase flow. While wall slugs have a limited impact on particle mixing since they do not cover the entire cross-sectional area of the tube, axis-symmetric slugs can significantly impair heat transfer due to the reduction in axial and radial particle mixing, as well as direct contact between the gas volume and the tube wall, thus hindering particle convection heat transfer [127]. Moreover other studies suggest that the turbulent regime is the most favorable for on-sun operation in order to maximize the wall-to-bed heat transfer and, consequently, the receiver efficiency [32, 72].

In light of these observations, it becomes evident that a comprehensive understanding of the underlying physics of multiphase flows is crucial for designing more efficient

2.2. The Challenge posed by Particle Fluid flows

and effective UBFB systems. By thoroughly investigating both the operating conditions and potential measures that can mitigate the axi-symmetric slugging phenomena while enhancing turbulent fluidization in long tubes, we can develop strategies to optimize the performance of UBFB receivers. This, in turn, will enable the development of more advanced and scalable solar power systems, paving the way for a cleaner and more sustainable future.

2.2 The Challenge posed by Particle Fluid flows

Grasping the dynamics of fluid-particle flows is critical, yet this remains a daunting task due to inherent complexities. The difficulty in making sense of these flows is mainly attributed to two factors - the multiscale nature of interactions in fluid-solid flows and the limitations of the tools available to study them.

In the context of fluidized bed systems, the largest flow structures can be on the order of meters. Yet, these structures are directly influenced by particle-gas and particle-particle interactions, which take place on a scale of micrometers [113]. Fig. 2.6a illustrates the multiscale and intricate nature of the physics of fluid-particle flows.

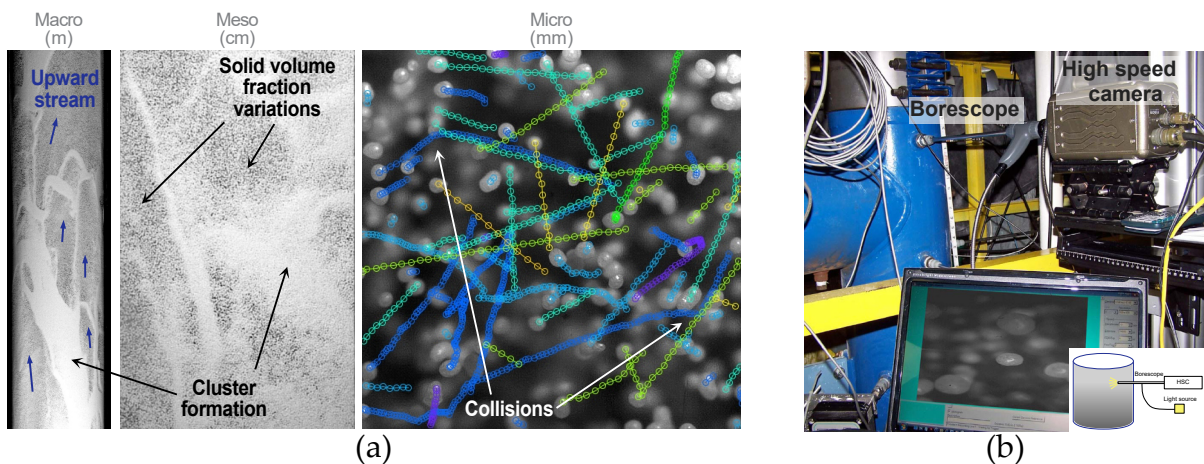


Figure 2.6: (a) Multiscale character of granular flows. (b) High speed camera characterization of the granular flow.

At the smallest scale, known as the *microscale*, interactions occur between individual particles and the surrounding fluid. In particle-laden flows, the particle diameter d_p is an essential length scale. Consequently, flow features near the particles, such as boundary layers and wakes, are usually defined as a function of the particle size. These features generate structures that typically range from 1 to $10 d_p$ [105]. The behavior of the flow around particles is also significantly influenced by the solid volume fraction. In fluidized bed systems, this fraction can range from less than 5% to nearly the close-packing limit, depending on the inlet velocity. The magnitude of the solid volume fraction governs the significance of collisional interactions relative to particle-fluid interactions. For highly

2.2. The Challenge posed by Particle Fluid flows

dilute flows, the effect of flow on a particle at the microscale can be adequately described by the flow past an isolated particle. However, as the volume fraction increases and particles move closer to each other, the wakes start to interact and merge. This makes it challenging to associate a flow structure uniquely with a particle. At this level of mass loading, particle-particle and particle-wall collisions also come into play. These micro-interactions occur over extremely short timescales ranging from microseconds for the fluid phase to nanoseconds for the solid phase.

Scaling up, we encounter *mesoscale* interactions, encompassing phenomena that span lengths and timescales larger than the microscale but smaller than the macroscale. The definition of mesoscale isn't precise or universally agreed upon. However, a useful definition, among many, considers mesoscale as the length over which particles are no longer uniformly distributed, and the variation in volume fraction becomes significant [104]. At this level, the focus shifts to understanding fluid velocity fluctuations caused by intermediate mechanisms. These include the formation and evolution of instabilities or inhomogeneities, the variations in particle concentration, and the clustering behavior where hundreds of particles congregate together under the influence of cohesive and electrostatic forces.

Finally, at the *macroscale*, interactions are dictated by the specific problem or application context. This level encompasses the large-scale structures and patterns that come to light as a consequence of interactions unfolding at smaller scales. In the context of turbulent flow, the macroscale corresponds to large-scale energy-containing motions. The time scales involved in this context are also extensive, ranging from several seconds to hours. The macroscale features phenomena such as the formation of bubbles, the occurrence of slugging, or the overarching circulation of particles, to name a few. An added layer of complexity is introduced by boundaries, which contribute to macroscale inhomogeneities that persist even when averaged over time [105]. For instance, in riser flows, higher concentrations of particles are often observed near bounding walls. This can lead to a downward motion of particles (and sometimes gas) in the wall region and an upward flow in the core region, a pattern found commonly in both riser flow and turbulent fluidization. These inhomogeneities have a far-reaching impact on gas and particle residence time distributions within the device, affecting the degree of contact between phases. Ultimately, these factors influence the overall performance of the system. The interconnectivity of these scales is bidirectional, as microscale processes influence mesoscale behavior, which in turn shapes macroscale processes. Conversely, macroscale features define the environment for mesoscale interactions, which subsequently dictate the conditions for microscale phenomena to occur.

While a deep understanding of fluid-particle flows requires a comprehensive exploration across all these scales the endeavor is often hindered by the limitations of analytical and experimental methods available:

Mathematically, these flows are notoriously complex, with strongly coupled and nonlinear governing equations that are dependent on the location of the two-phase interface. This complexity makes it challenging to use *analytical methods*. Even for seemingly simple configurations, such as flow around a sphere. Analytical solutions are only

available for the limiting cases of very low Reynolds numbers (creeping flow in the Stokes regime) or very high Reynolds numbers (inertial flow in the Newton regime), leaving the intermediate cases - which are often the most relevant - without a clear analytical solution Clift, Grace, and Weber [23].

Moreover, most of what is currently known about two-phase flow dynamics comes from *experimental* studies. These investigations have delved into a diverse array of fluid-solid flow characteristics, such as the existence of different fluidization regimes, the preferential clustering of particles, and the emergence of bubble-like voids in dense fluidized beds. Furthermore, researchers have uncovered the crucial role that operating conditions play in fluidization behavior, highlighting the significance of factors such as flow rates and pressure in determining the overall performance of fluidized beds. Experimental studies have also explored the effects of varying temperatures on fluid-solid flows, demonstrating that high temperatures can lead to particle recirculation near the walls, a phenomenon not observed at room temperature [8]. Additionally, researchers have investigated the impact of slugging on heat transfer rates and mixing, identifying strategies to optimize the efficiency of fluidized bed systems. Other notable findings from experimental studies include the observation of vertically traveling one-dimensional (1D) waves in liquid-fluidized beds and the secondary instability of such beds. However, despite the extensive literature on this topic, the implementation of experimental protocols is not always straightforward. The spatial scales that researchers are interested in are often quite small, making visual or optical access to these scales difficult with non-intrusive methods such as high-frequency video capture, PIV, radioactive tracers, or acoustic spectroscopy. Additionally, with these non-intrusive methods, it is often necessary to adjust the optical indices of the two phases, which can be challenging, especially for gaseous fluidized beds. Moreover, the control of operating conditions, particularly the fluidization rate, is also an important parameter that is not always easy to set up.

2.3 Numerical Modeling of fluid particles flows

In this context, numerical simulation techniques offer an interesting and complementary approach for gaining a better understanding of the complex physics of multiphase flows. By utilizing appropriate numerical methods, we are able to conduct virtual experiments that provide us with an in-depth look at the flow without disrupting it. This allows for the examination of a broad range of operating conditions and provides comprehensive insights into the movement and interactions of the different phases. Additionally, numerical simulation possesses the ability to detach itself from real-world scenarios and study the impact of parameters that are unattainable to investigate in a laboratory setting. An example of this is the effect of weightlessness in microgravity, where in this case the numerical approach is often the only viable means at our disposal.

However, the multiscale nature of granular flows discussed previously presents a

2.3. Numerical Modeling of fluid particles flows

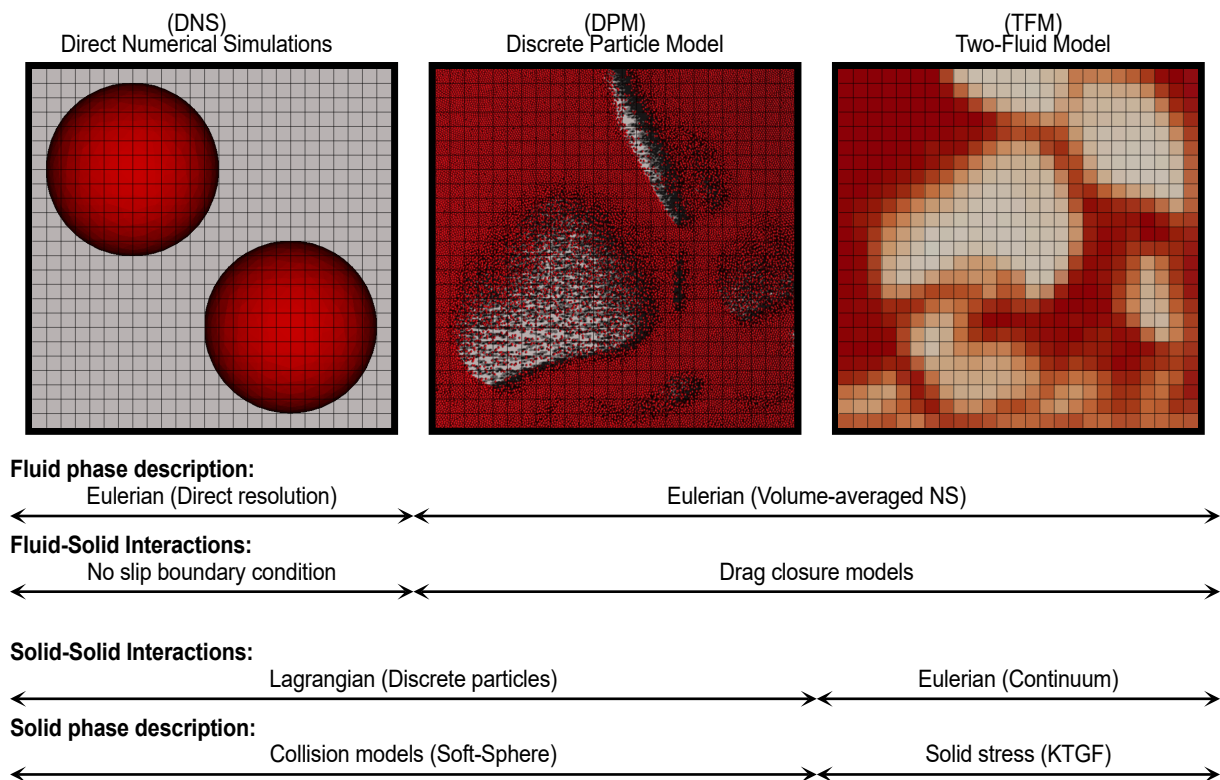


Figure 2.7: Overview of simulation methods in fluid-particle flows.

significant challenge in the numerical modeling of such systems, as it is not feasible to cover all time and space scales present in industrial applications with a single method. Consequently, over the years, a plethora of numerical methods have been developed and documented in the literature to target specific scales. These methods can be categorized into three main groups, akin to the previous classification of multiscale phenomena in granular flows: Macroscale methods, such as the Two Fluid Methods (TFM), focus on modeling the overall behavior of granular flows by considering the solid and fluid phases as interpenetrating continua. In this approach, both phases are described by separate sets of averaged conservation equations for mass, momentum, and energy. The coupling between the two phases is achieved through exchange terms that account for the interactions between particles and the surrounding fluid. Key interactions include the effective solid's pressure and the effective solids phase stress tensor, which represent the forces acting within the granular media and their effects on the flow. TFM is the primary method capable of simulating pilot-scale industrial processes due to its ability to capture the global behavior of the system without resolving individual particle interactions. However, one limitation of TFM arises from the averaging process used to derive the equations of the model. This averaging necessitates additional closures for the coupling terms, which are often obtained through empirical correlations or kinetic theory-based approaches, such as the Kinetic Theory of Granular Flow (KTGF). The use of empirical correlations or KTGF-based closures introduces a degree of uncertainty in the model predictions, as these closures may not accurately represent the wide range of granular flow conditions encountered in industrial applications. Furthermore, the TFM

2.3. Numerical Modeling of fluid particles flows

does not account for the detailed microscale phenomena that may influence the flow behavior, such as particle shape, size distribution, or cohesion.

At the mesoscale, the Discrete Element Method (DEM) [29, 17] is utilized to model granular flows by explicitly simulating the motion and interactions of individual particles in a Lagrangian framework while describing the fluid phase using an Eulerian approach. The particles are considered as rigid bodies interacting through contact forces. Newton's laws govern the motion of these particles, facilitating the incorporation of various forces, such as collision, friction, and cohesive forces. Particle-particle and particle-wall collisions are computed individually using appropriate models (e.g., hard-sphere or soft-sphere). A primary motivation behind the development of DEM models was to circumvent the need for modeling the rheology of the solid phase on a continuum scale. DEM is particularly well-suited for simulating systems where particle-scale effects are crucial and cannot be disregarded, such as in dense granular flows or fluidized beds with intricate particle shapes. However, these simulations necessitate input models for interphase interaction forces and effective stress in the fluid phase. The fluid-particle force must be provided as part of the model, either in the form of a correlation or by solving the locally averaged equations of motion for the fluid phase. This approach is commonly referred to as CFD-DEM.

Finally, at the microscale, Direct Numerical Simulation (DNS) is utilized to provide an in-depth understanding of the flow physics at the smallest scales. In DNS, the governing equations for the fluid phase are solved without any simplifications or turbulence modeling, capturing the full range of scales present in the flow. This method requires substantial computational resources due to the need to resolve all relevant scales, from the smallest turbulent eddies to the largest flow structures. However, DNS provides unparalleled insight into the fundamental mechanisms governing the behavior of granular flows, by providing detailed information on the motion and interactions of the phases, such as the particle trajectories, velocities, and collision rates, and the fluid velocity ...

Direct Numerical Simulation (DNS) techniques can be categorized into two primary categories: boundary-fitted and non-boundary-fitted methods. Each of these approaches has unique advantages and challenges that must be considered when selecting the most appropriate method for a given application.

Boundary-fitted methods (Fig. 2.8(a)), such as the Arbitrary Lagrangian-Eulerian (ALE) method or the Deforming-Spatial-Domain/Space-Time (DSD/ST) method, aim to conform the computational grid to the flow boundaries, providing a detailed and accurate representation of the flow behavior near solid surfaces. While these techniques are capable of capturing high-resolution flow information around complex geometries, they often require substantial computational resources and time for mesh generation. This becomes particularly challenging in three-dimensional cases, where the generation of high-quality meshes is essential for ensuring accurate numerical solutions. Additionally, the process of generating boundary-fitted meshes can be labor-intensive and require

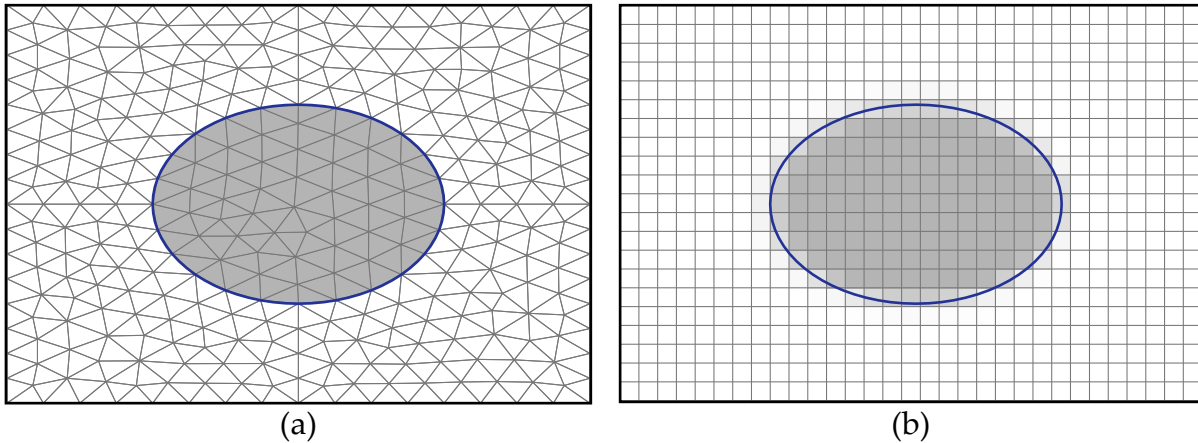


Figure 2.8: (a) Boundary-fitted grid. (b) Non-Boundary-fitted grid.

expert knowledge, potentially extending the time and resources needed for a successful simulation.

In contrast, non-boundary-fitted methods (Fig. 2.8(b)), such as the fictitious domain method, the immersed boundary method, and the Lattice Boltzmann method, use a non-aligned grid to solve the fluid phase equation, and handle the moving solid interfaces separately. The primary advantage of non-boundary-fitted methods is the relative ease of grid generation, usually employing a structured Cartesian grid. However, it is important to note that these methods show some limitations in accurately capturing flow details near boundaries compared to their boundary-fitted counterparts. Despite this limitation, they are almost always preferred for simulating large-scale solid-fluid flows due to their efficiency and ease of use, as demonstrated in the literature.

2.3.1 Multiscale modeling approach

In some cases, direct numerical calculation (DNS) can be readily used for solving practical problems, such as studying a laminar flow around bacteria in microbiology. However, it is generally not feasible to use this method for simulating industrial-sized systems as the DNS approach is computationally intensive and requires high-performance computing resources. But thanks to the advancements in computer technology and the development of more efficient numerical methods, it is now possible to conduct DNS on systems that were previously too large to simulate. We can now accurately model the evolution of diluted flows of several hundred particles over timescales that allow for statistical convergence. This makes the resulting simulations an ideal benchmark case for developing and validating other numerical methods.

Additionally, DNS methods can be used in an upscaling approach, providing valuable information for higher-scale methods that rely on precise closure laws.

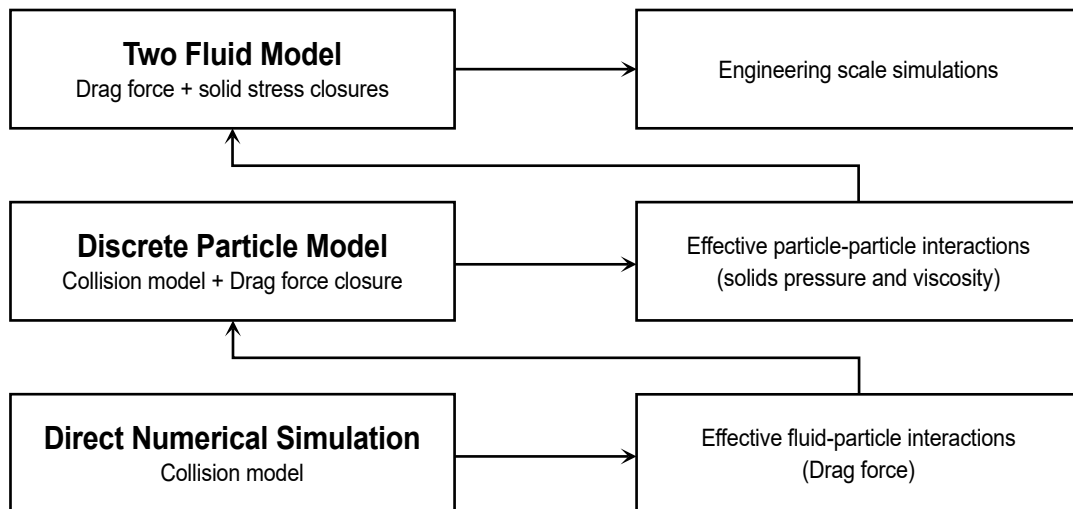


Figure 2.9: Multiscale modeling approach.

While DNS has been widely used in the study of single-phase turbulent flows, its application in the study of two-phase flows is still lagging behind. The DNS approach has been used to study a wide range of multiphase flow problems, including fluidized beds, particle-laden pipes, and spray systems. But most research in this area is focused on fixed particle beds with periodic walls. However, the greatest breakthroughs can be made in cases where it is necessary to track the motion of a significant number of particles and study their interactions with the walls of the domain.

Upon reaching maturity, it is expected that the simulations conducted will greatly aid in the design and optimization phases of engineering systems. This will not only reduce the need for experimental pilot tests but also decrease the time it takes for new technologies to be brought to market.

2.4 Thesis Objectives

To this end, the main objective of this thesis is to develop a direct numerical simulation method that can effectively simulate particle flow with more than a few hundred particles. This method will be implemented in the TrioCFD computational code, which was originally developed by the CEA for studying two-phase gas/liquid flows in nuclear reactors. However, the standard version of this code does not currently have the capability to simulate granular flows. Therefore, our implementation will require the use of an adapted technique to impose the rigidity constraint in the dispersed phase, as well as the implementation of a collision model to account for particle-particle interactions. Once developed, our method will be rigorously validated by simulating various test cases from the literature.

2.4. Thesis Objectives

During the next chapter, a brief reminder of the fundamental notions necessary for the study of granular flows will be given, alongside an overview of the different direct numerical simulation methods that can be used to study particle flow. In chapters 3 and 4, the method chosen for this thesis will be detailed and validated against preliminary test cases and a study of a fluidized bed of 2100 particles.

3

FUNDAMENTAL CONCEPTS ON THE PHYSICS OF FLUID-PARTICLE FLOWS

The purpose of this chapter is to provide an introduction to the fundamentals of particulate flows, including their physical background, and governing equations. By exploring these concepts, we will lay the foundation for the analysis and modeling of particulate flows that will be used throughout this thesis.

3.1 Key parameters and adimensional numbers

Density Ratio

The first dimensionless number of interest is the density ratio, represented by:

$$R_\rho = \frac{\rho_p}{\rho_f}$$

where ρ_p denotes the density of the particles, and ρ_f the density of the surrounding fluid. This dimensionless number characterizes the buoyancy of the particles in the fluid, as in case where $R_\rho = 1$, the particles are referred to as neutrally buoyant. These type particles, if small enough, hold significant experimental value as they tend to follow the flow streamlines precisely. When $R_\rho \neq 1$, the particles are known as inertial particles. Unlike neutrally buoyant particles, inertial particles do not strictly follow the streamlines. Instead, they tend to accumulate preferentially in fluid regions with high strain rates if the particles are heavy ($R_\rho > 1$), or in regions with low strain rates if the particles are light ($R_\rho < 1$).

Reynolds Number

The particle Reynolds number, denoted as Re_p , is a dimensionless parameter that quantifies the relative velocity of a particle with respect to the surrounding fluid. It is essential for characterizing the momentum exchange between the particle and fluid phases. The particle Reynolds number is defined as:

$$Re_p = \frac{\rho_f d_p W}{\mu_f}$$

where $W = |\mathbf{u}_p - \mathbf{U}_f|$ represents the magnitude of the slip velocity between the particle velocity \mathbf{u}_p and the fluid velocity \mathbf{U}_f far from the particle. μ_f denotes the dynamic viscosity of the fluid. The value of Re_p helps determine the nature of the flow around the particle. For $Re_p \ll 1$, the flow is in the Stokes regime. As Re_p increases, the flow separates, creating a recirculating eddy in the particle's wake. When $Re_p > 280$, the wake of an isolated particle exhibits time-dependent behavior and begins to shed vortices. Furthermore, the wake flow becomes turbulent when $Re_p > 500$.

Stokes Number

The Stokes number is a dimensionless parameter that provides information on the relative importance of particle inertia compared to that of the surrounding fluid. In particular, it is defined as the ratio of the particle response timescale τ_p to that of the

3.1. Key parameters and adimensional numbers

fluid τ_f . When the particle response time is much smaller than the fluid timescale, the particle follows the fluid motion closely and its behavior is essentially that of a passive tracer. On the other hand, when the particle response time is much larger, the particle behavior is dominated by its inertia.

The definition of the Stokes number depends on the velocity and length scales used in the definition of the response times of the fluid and the particle. One common definition based on the slip velocity W is given by the equation [108]:

$$St_p = \frac{2}{3} \frac{m_p W}{\pi \mu_f d_p^2}$$

where m_p is the mass of a particle. The Stokes number can be written as a function of the density ratio and the Reynolds number as follows:

$$St_p = \frac{1}{9} \frac{\rho_p}{\rho_f} Re_p = \frac{1}{9} R_p Re_p$$

Coefficient of Restitution

The dry coefficient of restitution e_d accounts for the energy dissipation during collision:

$$e_d = \frac{\Delta u_{reb,d}}{\Delta u_{imp,d}} \quad (3.1)$$

where $\Delta u_{reb,d}$ and $\Delta u_{imp,d}$ are, respectively, the rebound and impact relative velocities of the two solid surfaces colliding in the absence of fluid viscous dissipation (dry regime). The solid's dry coefficient of restitution is a physical property directly related to the material's elastic properties. The default value used in this work is $e_d = 0.97$.

In the wet regime, the energy dissipation is notably higher due to the fluid viscous dissipation. [68, 120] have shown experimentally that the apparent or effective coefficient of restitution is strongly correlated with the Stokes number St :

The relationship between the effective coefficient of restitution e and the Stokes number St can be written as the product of the constant dry coefficient of restitution and a "wet" coefficient of restitution, e_w depending on the St number. Typically e_w varies from 0 to 1:

$$e(St) = e_d e_w(St) = \frac{\Delta u_{reb}}{\Delta u_{imp}} \quad (3.2)$$

From Fig 3.1, we can see the effective coefficient of restitution e is pretty much equal to the dry coefficient of restitution for $St > 1000$. This is in accordance with the fact that in this range of Stokes numbers, viscous effects are negligible. However, for lower values of St , from 10 to 1000, significant variation of e is observed. The coefficient of restitution decreases with St and the related viscous stress rises. Below the critical value

3.1. Key parameters and adimensional numbers

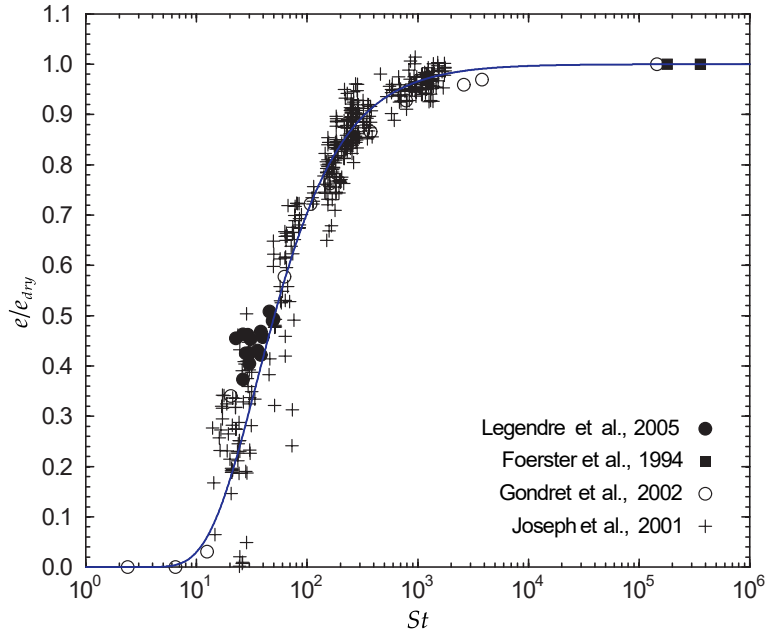


Figure 3.1: Adapted from [76]. Wet coefficient of restitution, as a function of the Stokes number St . The solid line is the best fit of the data points of [68, 53, 75, 47]

St 10, no rebound is observed. Using the analogy with a dissipative mass-spring system [75] showed that the evolution of the wet coefficient of restitution as a function of the St numbers followed the expression:

$$e_w = \exp\left(-\frac{35}{St}\right) \quad (3.3)$$

Mass loading

The solid volume fraction α_s , also known as the particle concentration, is a measure of the proportion of the volume occupied by particles V_s relative to the total volume of the mixture $V_m = V_f + V_s$. The solid volume fraction is expressed as:

$$\alpha_s = \frac{V_s}{V_m}$$

In a similar manner, the fluid volume fraction α_f can be represented by:

$$\alpha_f = \frac{V_f}{V_m}$$

Adhering to the principle of volume conservation, the entire volume is occupied by either the dispersed phase or the continuous phase. As a result, at any given point within the continuum, the combined sum of the two volume fractions is equal to 1:

$$\alpha_s + \alpha_f = 1$$

3.1. Key parameters and adimensional numbers

The volume fraction is closely related to phase coupling in multiphase flows. Phase coupling refers to the extent and nature of the interactions between different phases in a multiphase flow system - such as momentum, heat, and mass transfer. These interactions significantly affect the flow behavior. For example, in a solid-liquid flow, a high solid volume fraction (dense suspension) may result in stronger inter-particle interactions and increased friction between particles and the fluid. This can lead to changes in the flow regime, increased pressure drops, and reduced flow velocities. Conversely, a low solid volume fraction (dilute suspension) may result in weaker inter-particle interactions and less influence on the fluid flow.

In the following paragraph, we will classify the phase coupling of solid-fluid flows based on the volume fraction values.

3.1.1 Phase coupling

Elghobashi [42] introduced a classification system for gas-solid suspensions based on the solid volume (see Fig. 3.2) categorizing the coupling into three primary regimes:

- **One-way coupling:** In this regime, the solid volume fraction is low (in the range 10^{-6} to 10^{-5}), resulting in a negligible effect of particles on the gas flow. However, the gas flow does influence the motion of particles with sufficiently small inertia. In one-way coupling, the gas flow is treated as a pure fluid, and the particle phase motion is primarily governed by hydrodynamic forces, such as drag and buoyancy forces. It is assumed that particle-particle interactions are inconsequential in this regime.
- **Two-way coupling:** As the solid volume fraction increases (in the range 10^{-5} to 10^{-3}), the influence of the particle phase on the gas-phase flow pattern becomes significant. In this regime, turbulent structures commonly encountered in gas flows can be modified by the presence of particles. Although particle-particle interactions are still not considered dominant in two-way coupling, their impact on the gas flow becomes more pronounced, leading to alterations in the momentum or effective density of the fluid phase .
- **Four-way coupling:** For even higher solid volume fractions ($\alpha_s > 10^{-3}$), momentum transport among particles occurs through both hydrodynamics mechanisms and collisions between particles and/or confining walls. In this dense-particle regime, which is particularly relevant for industrial applications, particle-particle interactions become critical, necessitating the consideration of four-way coupling.

3.1. Key parameters and adimensional numbers

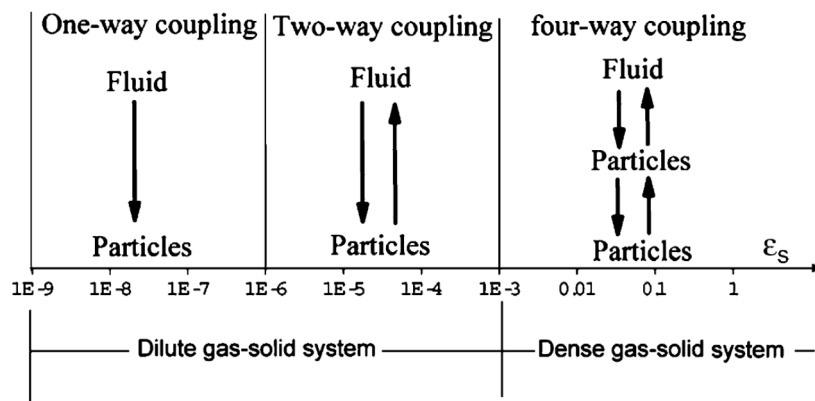


Figure 3.2: Interphase coupling. Based on [42, 112]

3.1.2 Fluidization

Phase coupling as a concept captures the essence of the interactions between fluid-particles and particle-particle at the microscopic level. The nature and intensity of these same interactions are directly related to the overall behavior of the mixture at a macroscopic level. One phenomenon of particular interest in a wide range of industrial applications that can emerge from these interaction is fluidization. The fluidization process, involves a fluid flowing upward through a bed of solid particles, suspending them and creating a dynamic, fluid-like state. This fluidized state allows for enhanced mixing and improved heat and mass transfer.

The type of particles in a fluidized bed plays a crucial role in determining the fluidization behavior. Geldart's classification (see Fig. 3.3) categorizes particles into four groups based on their fluidization properties at atmospheric pressure and room temperature:

- **Group A** (aeratable) particles exhibit appreciable but not dominant interparticle cohesive forces. They generally fluidize smoothly, show uniform bed expansion and high mixing in a fluidized state, and deaerate slowly when the flow is interrupted.
- **Group B** (bubble-ready or sand-like) particles have larger sizes with negligible interparticle forces. Bubbles form immediately when the gas superficial velocity exceeds the minimal fluidization velocity, and these particles mix relatively well in the fluidized state.
- **Group C** (cohesive) particles are dominated by strong interparticle cohesive forces due to their very small size. As a result, they tend to form clusters and aggregates, leading to agglomeration, channeling, and plugging phenomena, making them generally unsuitable for fluidization.

3.1. Key parameters and adimensional numbers

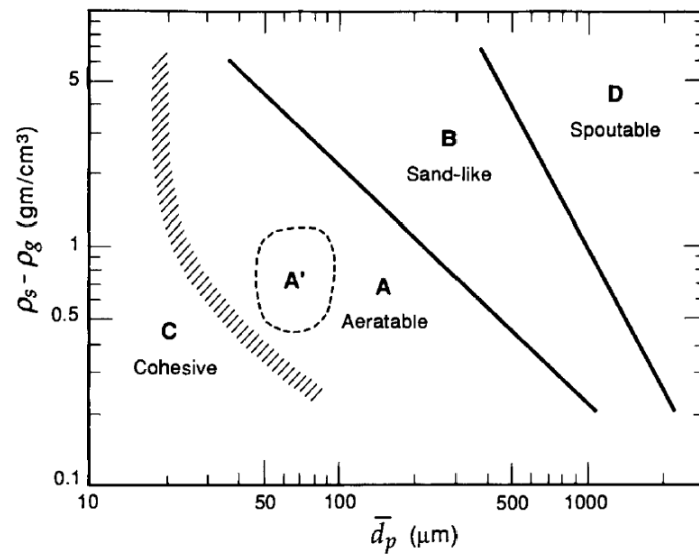


Figure 3.3: Geldart's powder classification.

- **Group D** (inertial or spoutable) particles consist of coarser particles with dominant inertia. They can be fluidized at higher velocities, but their mixing in the fluidization state is poor, making them more suitable for spouted fluidized beds.

Fluidization can manifest in several distinct regimes, which are primarily determined by the superficial gas velocity. Each regime is characterized by unique hydrodynamics, heat and mass transfer properties, making it important to understand the differences between these regimes and their transitions. Some of the primary fluidization regimes are:

- **Fixed bed:** In this regime, particles remain stationary, and no fluidization occurs. The fluid simply passes through the void spaces between the particles, leaving the bed in a fixed state.
- **Homogeneous fluidization:** In this regime, particles are uniformly suspended in the fluid, creating a homogeneous fluidized bed without the formation of bubbles. This type of fluidization is typically observed with Geldart Group A particles.
- **Bubbling fluidization:** Bubbles form and rise through the fluidized bed, causing significant mixing of the particles and promoting heat and mass transfer. Bubbling fluidization is a common regime for Geldart Group B particles.
- **Slugging fluidization:** Occurring in small-diameter beds, large gas slugs form and rise, causing significant bed expansion and particle movement. This regime is characterized by a pulsating motion and a series of pressure fluctuations.
- **Turbulent fluidization:** As gas velocity increases, particle motion becomes more chaotic, leading to enhanced mixing and improved heat and mass transfer. Turbu-

3.2. Fluid-Particles Interactions Modeling

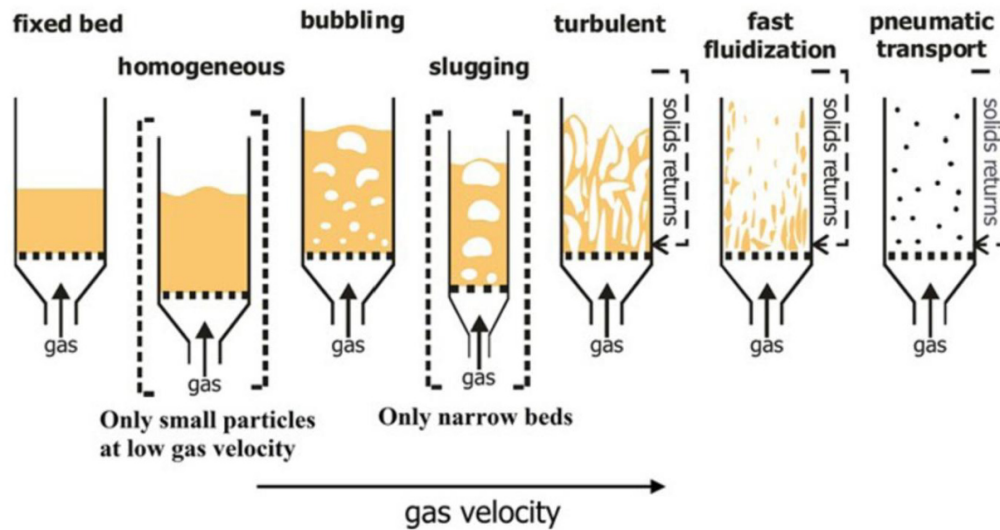


Figure 3.4: Illustration of fluidization regimes.

lent fluidization is particularly advantageous in industrial fluidization processes due to its vigorous gas-solid contact and high solid hold-up.

- **Fast fluidization:** In this regime, a dilute suspension of particles is achieved with high gas velocities, resulting in a more uniform distribution of particles throughout the bed. Fast fluidization is typically employed in circulating fluidized bed systems.
- **Pneumatic transport:** At high gas velocities, particles are conveyed upward in a dilute phase, similar to pneumatic conveying systems. This regime is characterized by low solid hold-up and high gas-solid contact, making it suitable for certain applications such as pneumatic conveying of powders and granular materials.

Fig. 3.4 provides a visualization of the different fluidization regimes.

3.2 Fluid-Particles Interactions Modeling

Before reviewing the various forces that may come into play during interfacial coupling, we recall some important concepts of solid mechanics that will be useful for deriving the governing equations in the following chapter.

3.2.1 Solid Phase Equations

In classical mechanics, the motion of a solid object is traditionally divided into the translation of the center of mass and rotation about the center of mass [52]. In a two-dimensional space, the solid's motion can be wholly described with three degrees of freedom (two translations and one rotation), while in three dimensions, six degrees of freedom are required (three translations and three rotations).

Consider a 2D solid particle, the center of mass of this object is denoted by x_p , while its orientation is denoted by θ_p . The position variables are related to the translational and rotational velocities u_p and ω_p respectively by:

$$\frac{dx_p}{dt} = u_p \quad (3.4a)$$

$$\frac{d\theta_p}{dt} = \omega_p \quad (3.4b)$$

In the context of three-dimensional space, describing the motion of particles is not as straightforward. It requires the use of three distinct angles, such as Euler angles, to accurately capture the orientation changes. This necessity adds complexity to the process of tracking orientation, as various techniques including Rotation Matrices, Cosine Angles, or Cayley-Klein parameters can be employed to accomplish this task (see [52]). Thus Eq. (3.4b) need to be replaced accordingly.

We call a "rigid body" an idealized entity possessing no internal degrees of freedom. This essentially means that no internal deformation takes place within such a body. Mathematically, this concept can be expressed as follows: for any two given points x_i and x_j on the solid, the distance between the two points remains unchanged, despite any external forces:

$$\frac{d}{dt} |x_i - x_j|^2 = 0 \quad (3.5)$$

During a Rigid Body Motion (RBM), the rigidity constraint Eq. (3.5) places specific conditions on the associated velocity field. Both necessary and sufficient, these conditions can be articulated in the following ways [107]:

Lagrangian form: The velocity field must be a Helicoidal Vector Field (HVF):

$$\mathbf{u}(\mathbf{x}) = \mathbf{u}_p + \boldsymbol{\omega}_p \times \mathbf{r} \quad (3.6)$$

where, $\mathbf{r} = \mathbf{x} - \mathbf{x}_p$ is the displacement vector.

Eulerian form: The strain rate tensor $D(\mathbf{u})$ must be null:

$$D[\mathbf{u}] = \frac{1}{2} (\nabla \mathbf{u} + \nabla^t \mathbf{u}) = 0 \quad (3.7)$$

3.2. Fluid-Particles Interactions Modeling

The time evolution of the center of mass velocity and angular velocity are governed by the Newton-Euler equations. These equations relate the rate of change of linear and angular momentum to the sum of external forces and moments (about the center of mass):

$$\frac{d}{dt} (m_p \mathbf{u}_p) = m_p \frac{d\mathbf{u}_p}{dt} + \mathbf{u}_p \frac{dm_p}{dt} = \sum \mathbf{F}_{ext} \quad (3.8a)$$

$$\frac{d}{dt} (\mathbf{J}_p \boldsymbol{\omega}_p) = \mathbf{J}_p \frac{d\boldsymbol{\omega}_p}{dt} + \boldsymbol{\omega}_p \times \mathbf{J}_p \boldsymbol{\omega}_p = \sum \mathbf{T}_{ext} \quad (3.8b)$$

where m_p and \mathbf{J}_p are the mass and moment of inertia tensor of the particle, respectively. They are given by:

$$m_p = \int_{\Omega_s} \rho_s dv \quad (3.9)$$

$$\mathbf{J}_p = \int_{\Omega_s} \rho_s (|\mathbf{r}|^2 \mathbf{I} - \mathbf{r} \otimes \mathbf{r}) dv \quad (3.10)$$

For a non-reactive (constant mass), spherically symmetric (isotropic inertia tensor) rigid particle, the general Newton-Euler equations simplify to:

$$m_p \frac{d\mathbf{u}_p}{dt} = \mathbf{F}_{fpi} + \mathbf{F}_{ppi} \quad (3.11a)$$

$$\mathbf{J}_p \frac{d\boldsymbol{\omega}_p}{dt} = \mathbf{r} \times \mathbf{F}_{fpi} + \mathbf{r} \times \mathbf{F}_{ppi} \quad (3.11b)$$

The external forces that influence a particle moving within a fluid are numerous and diverse. Accurately characterizing the impact of these forces on particle dynamics is crucial for understanding the complex of phases coupling. These external forces can be divided into two primary categories: Fluid-Particle Interaction forces \mathbf{F}_{fpi} and Particle-Particle Interaction forces \mathbf{F}_{ppi} . A comprehensive analysis of these two categories of forces will be undertaken in the subsequent sections. For a more refined understanding, we can further decompose the fluid-particle interaction forces into three categories: body (or volume) forces, hydrodynamic (or surface) forces, and transient (or inertial) forces:

3.2.2 Body Forces

When an object (or particle) is immersed in a fluid, it experiences an upward force known as the **buoyancy force**. This force arises due to the pressure difference between the top and bottom of the object in the fluid. Archimedes' Principle asserts that the

3.2. Fluid-Particles Interactions Modeling

buoyancy force equals the weight of the fluid displaced by the object. The net body force on the particle is the difference between the particle's weight and the buoyancy force:

$$F_b = \int_{\Omega_s} (\rho_p - \rho_f) \mathbf{g} dv \quad (3.12)$$

Assuming the densities are constant, the total force acting on the object becomes:

$$F_b = (\rho_p - \rho_f) V_p \mathbf{g} \quad (3.13)$$

where V_p is the total volume of the particle.

3.2.3 Hydrodynamic Forces

Hydrodynamic forces arise from the interaction between a fluid and an immersed particle's surface. This relationship is mathematically characterized by specific boundary conditions at the interface, most notably the kinematic and dynamic boundary conditions. These can be expressed as:

$$\begin{cases} \mathbf{u}(\mathbf{x}) = \mathbf{u}_s & \mathbf{x} \in \partial\Omega_s \\ \boldsymbol{\sigma}_f \cdot \mathbf{n} = \boldsymbol{\sigma}_s \cdot \mathbf{n} & \text{on } \partial\Omega_s \end{cases} \quad (3.14a)$$

$$\quad (3.14b)$$

where \mathbf{u} is the fluid velocity field at the interface location, \mathbf{u}_s is the solid's velocity at the same location, $\boldsymbol{\sigma}_f$ and $\boldsymbol{\sigma}_s$ are the stress tensors of the fluid and solid phases, respectively, and \mathbf{n} is the outward unit normal vector to the solid's surface $\partial\Omega_s$.

Given known pressure and velocity fields, the hydrodynamic forces acting on the particle can be determined by integrating the stress tensor across its surface:

$$F_h = - \oint_{\partial\Omega_s} \boldsymbol{\sigma} \cdot \mathbf{n} ds = - \oint_{\partial\Omega_s} p \mathbf{n} ds - \oint_{\partial\Omega_s} \boldsymbol{\tau} \cdot \mathbf{n} ds \quad (3.15)$$

Arguably these forces are the most important in influencing the particle's behavior within the fluid medium, and can be decomposed into three distinct contributions:

The Drag force:

The Drag force emerges due to the resistance encountered by a particle as it traverses through a fluid. The magnitude of this force increases as a function of the slip velocity between the fluid and the solid. This force exhibits a reactive nature since it materializes only when the object is in motion and it acts in the direction opposite to the object's movement through the fluid. This force is frequently represented as a function of

3.2. Fluid-Particles Interactions Modeling

the dimensionless Drag Coefficient (C_D) and the slip velocity by employing the drag equation:

$$F_D = \frac{1}{2} \rho_f C_D A (\mathbf{u}_f - \mathbf{u}_p) |\mathbf{u}_f - \mathbf{u}_p| \quad (3.16)$$

Here, A denotes the cross section of the solid perpendicular to the relative velocity ($\mathbf{u}_f - \mathbf{u}_p$). For a sphere, $A = \pi d_p^2/4$.

For an incompressible external flow over a sphere, the dimensionless drag coefficient primarily functions as the Reynolds number (Re). Its evolution is depicted Fig. 3.5 as the standard, steady drag coefficient curve.

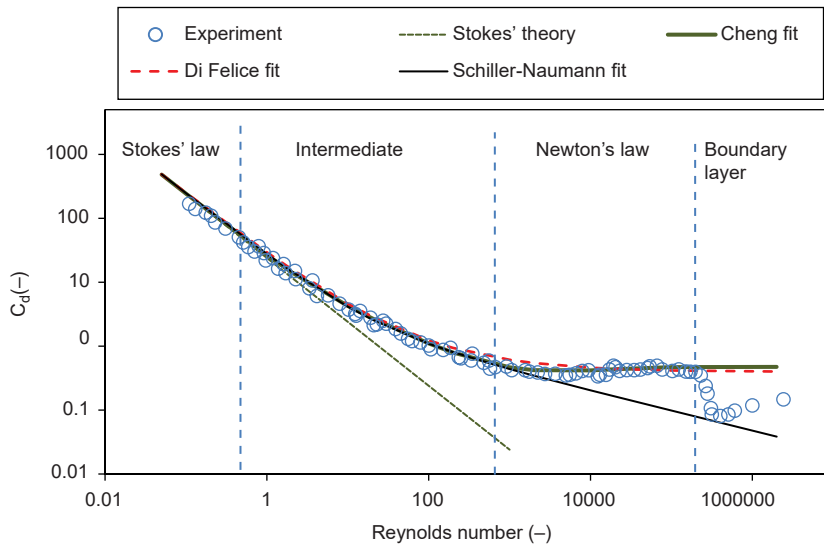


Figure 3.5: Drag coefficient for an incompressible flow over a smooth sphere as a function of Reynolds number, Cheng [20] correlation, Di Felice [33] correlation, and Schiller-Naumann correlation

While analytical expressions for the drag coefficient are limited to low Reynolds numbers, numerous empirical correlations have been developed to evaluate the drag coefficient. The most commonly utilized correlations are shown in Figure 3.5. For a recent review of empirical correlations for rigid spheres, refer to Goossens [54]. The figure highlights the presence of four distinctive regions:

Stokes' region: Here, an inverse relationship is observed between the drag force and the Reynolds number, resulting in a linear relationship between drag and slip velocity:

$$C_D = \frac{Re}{24}$$

$$F_{D,s} = 3\pi d_p \mu_f (\mathbf{u}_f - \mathbf{u}_p)$$

The flow is regarded as a creeping flow in which the inertial terms in the Navier-Stokes equations are unimportant. According to Stokes' theory, the pressure

3.2. Fluid-Particles Interactions Modeling

distribution contributes to a third of the total Stokes' drag (known as "form" drag), while two-thirds are due to the viscous stress on the sphere's surface (known as "friction" drag).

Intermediate region: This lies between the Stokes and Newton regions and is marked by an increased importance of inertial forces as the Reynolds number rises, resulting in a drag coefficient greater than that in Stokes' drag.

Newton's region: starting from Reynolds number of 100 the drag coefficient does not depend on the Reynolds number ($Cd \approx 0.445$). The flow begins to separate, forming vortices behind the sphere, which further reduces the pressure in the wake, enhancing the "form" drag. As the Cd versus Re curve flattens, the drag becomes predominantly "form" drag, with a marginal contribution from "friction" drag.

Boundary layer separation region: This region is typified by very high Reynolds numbers. At a critical Reynolds number ($Re \approx 3 \times 10^5$), the boundary layer becomes turbulent and the separation point moves to the rear, reducing the "form" drag and, thus, the drag coefficient. This behavior is solely due to boundary layer effects. Rough particles induce a transition to turbulence at a lower Reynolds number, lowering the critical Reynolds number. For particles with sharp edges, the separation is geometrically controlled (separation at sharp edges), and no critical Reynolds number effect is discerned.

The Lift force:

Lift forces occur due to velocity differences around the particle, leading to pressure differences that cause the particle to move perpendicular to the flow direction. When a particle undergoes rotational motion due to a velocity gradient or as a consequence of particle collisions, the hydrodynamic force manifests a transverse component referred to as the lift force or the Magnus force. The expression of the force is given by the relation proposed by Rubinow and Keller [98].

$$F_L = \frac{1}{8}\pi d_p^3 \rho_f \omega_p \times (\mathbf{u}_p - \mathbf{u}_f) \quad (3.17)$$

This force arises from the velocity asymmetry around the particle, which prompts a transverse pressure difference on the sphere's surface. The force follows a direction normal to the plane formed by the rotational velocity and relative velocity. To quantify the Magnus force, it is common to employ the lift coefficient C_L and the transverse section A :

$$F_L = \frac{1}{2}\rho_f C_L A |\mathbf{u}_p - \mathbf{u}_f| \frac{\omega_p}{|\omega_p|} \times (\mathbf{u}_p - \mathbf{u}_f) \quad (3.18)$$

3.2. Fluid-Particles Interactions Modeling

Several authors [77, 30, 5, 106] proposed correlations to estimate the lift coefficient at Reynolds numbers exceeding 2×10^3 . The correlation suggested by Oesterlé and Dinh [85] is commonly preferred for lift coefficient calculation:

$$C_L = 0.45 + (2\Omega - 0.45) \exp(-0.075\Omega^{0.4} Re_R^{0.7}) \quad (3.19a)$$

$$\Omega = \frac{d_p \omega_p}{2 |\mathbf{u}_f - \mathbf{u}_p|} \quad (3.19b)$$

where Ω refers to the spin parameters, and Re_R is the rotational Reynolds number. The correlation holds for $Re < 140$ and $1 < \Omega < 6$, reducing to the correct limit for low Reynolds numbers. Michaelides [80] posits that the results from Saffman's low Reynolds number analysis [101], often referred to as the Saffman force in the literature, is a specific instance of the Magnus force at low Reynolds numbers. Therefore, the lift force should only be considered once in particle dynamics computations.

Generally, the lift coefficient decreases with increasing Re_R and increases with increasing spin parameters Ω . However, experimental studies Tanaka, Yamagata, and Tsuji [106] demonstrated that the lift coefficient rises linearly with spin ratio at low spin ratios, then decreases sharply with increasing spin ratio, becoming negative at lower Reynolds numbers. This phenomenon is likely due to higher relative velocity on one side of the sphere and an early transition to turbulence in the boundary layer on that side. As a result, the wake behind the sphere deflects in an opposite direction than expected in rotating flow, reversing the direction of the lift force. A definitive explanation for the observed trends is still lacking.

Usually, the transverse lift force developed on a sphere is significantly weaker than the longitudinal drag force. However, in engineering applications the transverse lift can have a significant impact on the lateral migration and dispersion of particles towards cylindrical pipe walls. Due to the short radial distances involved, even small forces can effectively move particles close to the walls, thereby enhancing mixing.

The presence of other particles further enhances the lift force. In their numerical studies, Feng and Michaelides [44] demonstrated that the hydrodynamic force exerted by the suspension flow on a solid particle attached to a wall increases by 2-4 times when similar particles are present in the fluid.

Despite this observation, Hilton and Cleary [62] argued that there is currently no clear methodology to modify the expression for the Magnus force to account for the proximity of nearby particles and the non-spherical shape of the particles.

3.2.4 Transient Forces

Transient forces are acceleration-dependent and become significant when a particle's velocity changes within the fluid, i.e., during periods of acceleration or deceleration.

Virtual mass force:

When a particle is accelerated within a fluid medium, it necessarily imparts momentum to a portion of the surrounding fluid, causing it to accelerate as well. This interaction is governed by the virtual mass force, as demonstrated by Auton, Hunt, and Prud'Homme [4]. The force counteracts the particle's displacement and is described for a spherical particle with:

$$F_{AM} = \frac{\rho_f V_p}{2} \left(\frac{D\mathbf{u}}{Dt} - \frac{d\mathbf{u}_p}{dt} \right) \quad (3.20)$$

The virtual mass force can be conceptually understood as increasing the mass of the particle by the equivalent mass of the fluid that it displaces, hence its other name of "added mass force". While this effect is minimal in air-solid flows due to a small density ratio, it is significant in solid-liquid flows [63]. For non-spherical particles, the added mass force remains similar, but the displaced volume must be adjusted for the specific shape [28].

History force:

Also referred to as the Basset force accounts for the inherent delay in boundary layer development around the moving particle. The flow around a particle cannot adjust instantly to changes in the particle's motion due to the fluid's viscosity. Essentially, the fluid has a "memory" of the particle's past trajectory, hence the term of "history force". In the case of creeping flow around a sphere, Basset [6] derived the expression for this force as:

$$F_H = \frac{3}{2} d_p^2 \sqrt{\pi \rho_f \mu_f} \left[\int_0^t \frac{\frac{d}{dt'} (\mathbf{u}_f - \mathbf{u}_p)}{\sqrt{t - t'}} dt' + \frac{(\mathbf{u}_f - \mathbf{u}_p)_0}{\sqrt{t}} \right] \quad (3.21)$$

The second term within the brackets accounts for an initial particle velocity scenario [95]. This force hinges on the particle's entire acceleration history, making its evaluation challenging. While the history force has significant relevance in unsteady liquid-solid flow applications, its impact is minimal for small density ratios, like air-solid application [63]. The existing analytical expressions for the transient hydrodynamic force on particles are valid primarily for low Reynolds numbers. As we venture into higher Reynolds number regimes, these formulations become inadequate. For higher Reynolds, experimental data and semi-empirical correlations are used as a correction for the force [81].

As a summary, Eq. (3.22) consolidates all previously discussed forces into a unified

expression:

$$\begin{aligned}
 \mathbf{F}_{fpi} = & (\rho_p - \rho_f) V_p \mathbf{g} && \text{Body force} \\
 & + \frac{1}{2} \rho_f C_D A (\mathbf{u}_f - \mathbf{u}_p) |\mathbf{u}_f - \mathbf{u}_p| && \text{Drag force} \\
 & + \frac{1}{2} \rho_f C_L A |\mathbf{u}_p - \mathbf{u}_f| \frac{\boldsymbol{\omega}_p}{|\boldsymbol{\omega}_p|} \times (\mathbf{u}_p - \mathbf{u}_f) && \text{Lift force} \\
 & + \frac{\rho_f V_d}{2} \left(\frac{D\mathbf{u}}{Dt} - \frac{d\mathbf{u}_p}{dt} \right) && \text{Virtual mass force} \\
 & + \frac{3}{2} d_p^2 \sqrt{\pi \rho_f \mu_f} \left[\int_0^t \frac{\frac{d}{dt'}(\mathbf{u}_f - \mathbf{u}_p)}{\sqrt{t-t'}} dt' + \frac{(\mathbf{u}_f - \mathbf{u}_p)_0}{\sqrt{t}} \right] && \text{History force}
 \end{aligned} \tag{3.22}$$

This equation represents the totality of forces that influence a particle's motion within a fluid medium, each with its unique origins and effects. However, it is important to remember that this equation, in its full complexity, applies to isolated spherical particles in conditions of ambient temperature. As we attempt to extend this model to more complex scenarios such as non-spherical particle shapes, interaction among multiple particles, and thermal effects, the analytical characterizations of these forces tend to become increasingly convoluted. In fact, there are many situations where analytical expressions for these forces are not available at all. In these instances, empirical correlations, with their inherent limitations and scope of applicability, are often used as an approximation.

The challenging nature of these problems underscores the potential role of Direct Numerical Simulation (DNS) in the field of fluid-particle interaction. DNS methods have the capability to fully resolve the intricate dynamics of fluid-particle interactions, thereby eliminating the necessity for force models or correlations. In the next section, we will review DNS-based numerical methods capable of handling such complex configurations.

3.3 Numerical methods for BF-PRDNS

3.3.1 Immersed Boundary Methods

The Immersed Boundary Method (IBM) is a computational fluid dynamics approach originally proposed by Peskin [89] for solving fluid flow around heart valves.

In IBM, Lagrangian marker points are attached to the immersed solid object. These markers are advected with the local fluid velocity. In other words, they move along with the fluid flow. The deformation of these markers due to the fluid motion allows the calculation of a Lagrangian rigidity force, which is then spread back to the Eulerian

grid using a Dirac delta function.

For modeling totally rigid solids, the original IBM can be used with high spring stiffness. However, this continuous forcing approach severely limits the time step due to stability considerations. As a result, this approach is generally avoided in favor of a discrete version of the method. In the discrete version of IBM, the forcing term is calculated from a target rigid velocity field, which is determined by solving the Euler-Newton equation. The Euler-Newton equation describes the motion of a rigid body, taking into account the hydrodynamic forces computed from the Eulerian velocity and pressure fields. In this way, the discrete IBM allows for a more stable and efficient simulation of fluid flow around rigid bodies by directly imposing the rigidity constraint at the velocity level.

3.3.2 Distributed Lagrange Multiplier

The Distributed Lagrange Multiplier (DLM) method, otherwise known as the Implicit Fictitious Domain Method is based on the global variational formulation of fluid and particle momentum conservation equations. In this framework, the full computational domain is filled with the background fluid (ρ_f in both fluid and solid regions). Distributed Lagrange Multipliers are applied over both the particle surface and volume in the form of an additional body force to enforce the rigid body motion constraint and the no-slip condition at the same time. originally, the governing equations are discretized using a finite-element spatial discretization [50, 51]. However, if the equations are reformulated in a non-variational form, alternative discretization methods can be employed. For instance, finite-volume methods [94, 116, 43], or finite-difference methods [124, 123] can be utilized.

The system of equations derived from the variational formulation form a constrained minimization problem with a saddle point. The two constraint involved are the divergence-free of the fluid velocity, relaxed by pressure p as a Lagrange multiplier and the rigid body motion within particles, relaxed with the DLM λ . The divergence-free constraint is automatically imposed on the solid regions as the rigid body motion constraint is mass conserving by construction. The system of equations are usually solved with a fractional step time algorithm coupled to an iterative Uzawa algorithm / pre-conditioned conjugate gradient solver [50, 116].

Historically, the Distributed Lagrange Multiplier method was first introduced by Glowinski et al. [50], where the solid constraint on the velocity field was imposed using Eq. (3.6). However, it was demonstrated that this formulation was inadequate for neutrally buoyant and light particles ($R_\rho \leq 0$). Patankar et al. [87] made improvements to the method by employing Eq. (3.7) as a constraint instead of Eq. (3.6), thereby successfully allowing the simulation of light particles. This approach eliminated the need for the use of translational and angular velocities, as the solid constraint was now expressed in an

Eulerian manner, similar to a fluid.

To avoid the computational cost induced by the Uzawa algorithm, a number of researchers proposed an explicit equation for the DLM λ [114, 123, 49], making the method strikingly similar to the Direct Forcing Immersed Boundary methods. Sharma and Patankar [102] suggested using a projection technique to directly approximate the rigid velocity field and to impose it on a discrete level. Yang et al. [121] further enhanced this method by using a least-square projection method to derive an expression for the rigidity force explicitly written on a continuum level. This approach was found to be equivalent to the Newton-Euler formulation.

A key benefit of the Distributed Lagrange Multiplier (DLM) method lies in its well-established stability and efficiency, as it eliminates the need for direct calculation of hydrodynamic forces on particles, thereby saving significant computational time. However, this computational efficiency is offset by the additional computing overhead required to solve a large number of linear and non-linear equations that result from the implicit coupling between the fluid and particles.

3.3.3 Viscous Penalty Methods

Instead of adding an additional force source term to the governing equation as done in preceding techniques, the Viscous Penalty Method modifies the fluid properties in solid regions by assigning a very high viscosity value within these regions. This elevated viscosity serves as a penalization parameter, forcing the fluid in these regions to mimic the behavior of a rigid body.

The application of high viscosity promotes near-zero strain rates in the solid domain, implying virtually no deformations. Nonetheless, this does not impede the motion of the solid object within the fluid. The viscosity penalty method enables fluid-solid interaction while upholding the non-deformation criterion within the solid region.

The effect of this heightened viscosity is that the viscous stress tensor term becomes dominant in the discretized momentum equation within the penalized region. Once numerical convergence is achieved, the strain-rate tensor approximates zero.

While the original method is a first-order method, the Viscous Penalty Method was later advanced to a second order by Caltagirone and Vincent. They separated the different contributions of the deformation rate tensor into viscosities that are expressed on the pressure nodes and other contributions expressed on the velocity nodes, allowing for a more precise control over the penalization procedure.

3.3.4 Lattice Boltzmann Methods

Unlike the traditional Computational Fluid Dynamics (CFD) methods, which solve the Navier-Stokes equations, the LBM is based on the discrete Boltzmann equation, simulating the process of particles moving and colliding on a lattice. The method uses a simplified kinetic model with a limited number of particle velocities (corresponding to the lattice points) to recover the macroscopic hydrodynamic behavior. The advantage of LBM is its simplicity, as it provides a very simple and efficient way of incorporating the effect of complex boundaries, and it can be easily implemented on parallel computers due to its local dynamics.

3.4 Particle-Particle Interactions Modeling

In general, Non-Boundary-Fitted-Particle-Resolved (NBF-PR) methods are ideally suited to capture the long-range hydrodynamic interactions between the fluid and solid phases. However, they are not the best suited methods to capture the short-range interactions. The lubrication effects are under resolved, and the collisions are not taken into account intrinsically by NBF-PR methods. Additional modeling is required to take those interactions into account.

Three major types of forces contribute to these interactions: lubrication forces, direct contact forces, and cohesive forces.

3.4.1 Lubrication modeling

When two particles are brought into close proximity, a local pressure buildup in the inter-particle region forces the fluid out. Conversely, when the solid particles move apart, the fluid is pushed back into the gap during rebound. The friction generated by this motion of fluid is known as the lubrication force. This force, being purely dissipative, persistently resists the solids' motion. At low approach velocities, the lubrication force can prevent direct contact between solids, whereas at higher velocities, it acts as a damping mechanism, reducing the coefficient of restitution relative to the dry coefficient of restitution. This additional dissipation could potentially enhance secondary collisions by maintaining a close distance between the particles. The influence of the lubrication force becomes more pronounced as the solid volume fraction increases and the average interparticle distance decreases. In dense suspensions, it often becomes the dominant component of the total hydrodynamic force.

The NBF-PR method adequately captures these frictional forces provided that the distance between two solids is greater than two simulation cells. However, when the spacing becomes less than one cell, a large portion of the hydrodynamic force attributed to the lubrication effect remains unresolved. While a finer mesh can capture

3.4. Particle-Particle Interactions Modeling

the dissipative effect of the lubrication force more accurately, the computational cost incurred by such a mesh can be prohibitive. Some researchers have proposed using locally refined meshes to alleviate the calculation time, whereas others have used a corrective force based on lubrication theory.

According to [27], the analytical expression for the normal lubrication force experienced by two perfectly smooth and identical spheres can be represented as a Stokes drag law multiplied by an amplification factor $\lambda(\varepsilon)$:

$$F_l = -6\pi\mu_f r_s \Delta u_n \lambda(\varepsilon) \quad (3.23)$$

The amplification factor is a function of the dimensionless gap $\varepsilon = 2\delta_n/d_p$, expressed differently depending on whether particle-particle or particle-wall collisions are considered:

$$\lambda_{pp} = \frac{1}{2\varepsilon} - \frac{9}{20} \log(\varepsilon) - \frac{3}{56} \varepsilon \log(\varepsilon) + 1.346 + O(\varepsilon)$$

$$\lambda_{pw} = \frac{1}{\varepsilon} - \frac{1}{5} \log(\varepsilon) - \frac{1}{21} \varepsilon \log(\varepsilon) + 0.9713 + O(\varepsilon)$$

Where δ_n is the inter-particle distance. As this distance approaches zero, the analytical expression becomes singular, emphasizing that theoretically, perfectly smooth spherical particles never actually touch. However, this is unrealistic in practice, as particles are never entirely smooth, and surface asperities (surface roughness) are always present, causing the lubrication force to saturate or even break down when the continuum hypothesis is no longer valid. To account for this effect, a user-defined saturation distance is introduced, within which the lubrication force is held constant until deactivated. Since the NBF-PR methods do capture a part of the lubrication force, this force does not need to be continuously active, but rather only when grid resolution is lacking. This distance is referred to as the activation distance. In these models, lubrication forces are assumed to be pairwise additive. Similar force expressions can be derived for the tangential component of the lubrication force.

3.4.2 Direct Contact Modeling

Simulating direct contact between solids presents challenges. A comprehensive collision model based on elastic material properties would be computationally excessive, as the necessary ordinary differential equations are extremely stiff. This makes flow configurations with thousands of particles infeasible to simulate, even on high-performance computing platforms. Therefore, a macroscopic description of collisions is more appropriate. We will use the same classification as Kempe and Fröhlich [71] for the contact modeling families.

Repulsive Potential

Glowinski et al. [50] proposed the Repulsive Potential Model. Though not physically based, its main objective is to prevent particle overlap by applying a normal repulsive force on the interacting surfaces. The force expression is as follows:

$$\mathbf{F}_c = \begin{cases} 0 & \text{if } \delta > d_{act} \\ \frac{1}{\epsilon} (\mathbf{x}_p - \mathbf{x}_q) (\delta + d_{act})^2 & \text{if } \delta \leq d_{act} \end{cases} \quad (3.24)$$

Here, δ is the inter-particle distance for two particles p and q with radii r_p and r_q , and positions \mathbf{x}_p and \mathbf{x}_q respectively:

$$\delta = r_p + r_q - \|\mathbf{x}_p - \mathbf{x}_q\| \quad (3.25)$$

d_{act} is the threshold activation distance at which particles are repulsed, and ϵ is the stiffness parameter, which is set to a small value. In this model, particles can overlap. It has been successfully employed for simulating dilute suspensions, such as in [111]. However, the simplicity of this force results in poor physical fidelity, especially in high volume fraction flows where kinetic energy dissipation due to collisions cannot be neglected. It also fails to capture collision-induced rotation of spherical particles.

Hard Sphere Modeling

The hard-sphere model uses an impulsive interpretation of collision forces, defined by the integral of the collision force over time [47, 65]. It assumes binary, pairwise additive, momentum-conserving collisions that occur instantaneously, transitioning immediately from pre-collision to post-collision velocities. There is no time scale associated with the collision process. This model only requires the normal coefficient of restitution, the tangential coefficient of restitution, and the Coulomb (dynamic) friction coefficient. For a comprehensive derivation of the impulsive collision equation, readers are referred to [28]. In the context of multi-sphere simulations, the hard-sphere model is implemented in an event-driven manner. Collisions are processed sequentially in the order they occur, making the model efficient for systems that are not densely populated and where collision frequency is low. However, this model cannot account for multiple simultaneous collisions, a limitation that impacts its applicability in high particle volume fraction scenarios where collision frequency significantly increases. The hard-sphere model also cannot handle persistent contacts, a disadvantage in systems where many particles are either stationary (packed) or moving collectively (clustered). Moreover, in situations where the coefficient of normal restitution is low, collisions can lead to a dramatic decrease in kinetic energy, known as inelastic collapse [79]. In this regime, collision frequencies diverge as relative velocities disappear, rendering the hard-sphere method unsuitable. Lastly, while the hard-sphere model can accommodate non-spherical rigid bodies, it requires accurate determination or approximation of the

next collision time. However, accurately estimating the next collision for non-spherical bodies is challenging. Approaches for complex shapes like polyhedra or ellipsoids have been suggested [82, 34], but these involve a certain level of overlap and cannot strictly satisfy the non-penetration constraint geometrically.

Soft Sphere Modeling

Distinct from the hard-sphere model, the soft-sphere model, first introduced by [29], allows a minor degree of overlap between particles during collisions. The model derives contact forces from this overlap using a specific contact-force scheme, which is fundamental to the method. The model's equations of motion are explicitly integrated over time, with contact forces and torques stemming from the geometric properties of the overlap. This approach enables multiparticle collisions, with the total contact force determined by the summation of all pairwise interactions. Soft-sphere models primarily operate in a time-driven manner, necessitating a judicious selection of the time step to accurately calculate the contact force. For stability and precision, the chosen time step should be smaller than the contact duration (approximately 10 time steps per collision [71]). This requirement imposes the need for tiny time increments, given that the characteristic contact duration is several orders of magnitude shorter than the relevant time scales of macroscopic physics. Even though the soft-sphere model typically requires more computational time than the hard-sphere model, especially for dilute flows, it readily incorporates the integration of pairwise cohesive forces, which is not as straightforward in the hard-sphere approach. This feature enhances the versatility of the soft-sphere model, making it suitable for a broader range of simulation scenarios (multiple simultaneous contacts, dense regimes, low coefficients of restitution, etc.). Therefore, soft-sphere models are almost always preferred for simulating dense particulate flows, like those of interest in this work.

The main variation among different soft-sphere models found in literature resides in the contact-force scheme employed. These schemes represent repulsive interparticle forces using mechanical elements such as springs and dash-pots. The following section will concentrate on the contact models most frequently used in the context of particle-laden flows. As the scope of this thesis is limited to smooth spherical particles, tangential force models will not be addressed. For a more comprehensive overview of the soft-sphere model, readers can refer to [103, 73], among others.

Force-Displacement Laws

Many of the most commonly used force-displacement laws within the context of the Discrete Element Method (DEM) can be expressed as the sum of an elastic term and a dissipative term:

$$\mathbf{F}_c = k\delta^\alpha + \beta\eta\dot{\delta} \quad (3.26)$$

3.4. Particle-Particle Interactions Modeling

where k is the spring stiffness coefficient and η is the damping coefficient. Depending on the values of α and β , the collision model can be classified as linear ($\alpha = 1$), non-linear ($\alpha \neq 1$), elastic ($\eta = 0$), or viscoelastic ($\eta = 1$). δ is the normal inter-particle distance, and $\dot{\delta}$ is the normal relative velocity between the two colliding particles.

Linear Spring Model: ($\alpha = 1$ and $\beta = 0$) In its simplest form, the force-displacement relationship is expressed by Hook's law indicating a linear relationship between the force and displacement. This relationship suggests that the energy is conserved, and the collision is considered completely elastic. Analytical solutions are available for the corresponding harmonic oscillator motion.

Hertz Model: ($\alpha = 3/2$ and $\beta = 0$) By solving the linear elasticity equation for elastic bodies in contact, Hertz [60] showed that the collision force is proportional to the 1.5 power of the depth of indentation δ . This tendency was later confirmed by experimental studies and Finite Element Analysis (FEA) simulations [129, 93]. If the material properties of the particles, such as the Young's modulus E and the Poisson coefficient ν , are known, the spring stiffness can be expressed as:

$$k = \frac{4}{3} \sqrt{r_{\text{eff}}} E_{\text{eff}} \quad (3.27)$$

where r_{eff} and E_{eff} are the effective radius and the effective Young's modulus, respectively:

$$r_{\text{eff}} = \left(\frac{1}{r_p} + \frac{1}{r_q} \right)^{-1},$$

$$E_{\text{eff}} = \left(\frac{1 - \nu_p^2}{E_p} + \frac{1 - \nu_q^2}{E_q} \right)^{-1}.$$

Based on this spring stiffness, the collision duration predicted by the Hertz theory is given by [60, 71]:

$$T_c^H \approx 2.439 \left(\frac{m_{\text{eff}}^2}{\Delta u_r k^2} \right)^{\frac{1}{5}} \quad (3.28)$$

This model has the advantage of being analytically derived for spheres, but no generalization for arbitrary shapes is available. Like the preceding model, the collisions are assumed to be elastic and any material damping is neglected. Furthermore, in the presence of a viscous fluid, the fluid drainage decelerates the collision processes, resulting in longer collision durations compared to the dry regime. Based on the particle-wall collision experiments of [125], Legendre et al. [76] proposed a simple correlation to account for this effect on the collision time:

$$T_c = T_c^H \left(\frac{\rho_s + c_M \rho_f}{\rho_s} \right)^{\frac{2}{5}} \frac{1}{1 - 0.85St^{-0.1}} \quad (3.29)$$

3.4. Particle-Particle Interactions Modeling

where $c_M \approx 0.73$ is the added-mass coefficient for a spherical particle approaching a wall. For common materials such as rocks or steel, Eqs. (3.28) and (3.29) leads to collision durations of the order between 10^{-7} s to 10^{-6} s, which is an order of magnitude smaller than the relaxation time of inertial particles.

Nonlinear Viscoelastic ($\alpha = 3/2$ and $\beta = 1$) To account for energy loss by elastic waves during impact, a dissipative term is added to the Hertzian force. A large number of models for the dissipative term can be found in the literature. The simplest is the model proposed by Cundall and Strack, where the damping force is expressed as the product of the relative velocity and a dashpot coefficient responsible for dissipating some of the relative kinetic energy. However, a side effect of introducing the dashpot coefficient is a non-zero collision force at the start and end of the collision, which is physically unrealistic for non-adhering particles. The greater the relative velocity, the greater the non-zero force. To alleviate this, some authors have expressed the damping coefficient as a function of $\delta^{1/2}$. An analytical expression for the damping coefficient as a function of Poisson's ratio, Young's modulus, coefficients of shear, and bulk deformation viscosities can be found but it's more common to adjust the damping coefficient to best fit experimental results of the normal coefficient of restitution.

Linear Spring Dashpot ($\alpha = 1$ and $\beta = 1$) In the Linear Spring Dashpot model, the elastic term is computed using Hooke's Law like in the Linear Spring model, while the dissipative term is calculated using the dashpot model of Cundall and Strack. This model can be seen as a linearization of the Nonlinear Viscoelastic model. The motion of the system mirrors the motion of a damped harmonic oscillator, which accepts an analytical solution. Using the definition of the dry coefficient of restitution and appropriate boundary conditions, the dashpot coefficient can be expressed as:

$$\eta = -\frac{2 \ln e_{dry}}{\sqrt{\pi^2 + (\ln e_{dry})^2}}$$

The collision duration corresponding to half of the oscillation period is:

$$T_c = \sqrt{\frac{m_{eff} (\pi^2 + (\ln e_{dry})^2)}{k}}$$

According to [40], the spring coefficient of the system can be related to the material properties as:

$$k = \frac{4}{3} r_{eff} E_{eff}$$

Utilizing the above equation to compute the collision duration and solving the collision motion with an appropriate time step only leads to a very stiff system that over resolves the fluid motion.

Fortunately, it is possible to artificially stretch the collision duration to be larger than the fluid solver time step and still maintain the perceived separation of time

3.4. Particle-Particle Interactions Modeling

scales (or the discontinuity) in the motion of the particles as long as the maximum indentation is kept below 0.5% of the characteristic length of the particles [22, 118]. This procedure, however, renders the spring stiffness an ad hoc numerical parameter used to control the amount of geometric overlap, stripping it of any physical meaning.

Based on this principle, [45] manually reduced the value of the spring stiffness to obtain a satisfactory collision time. [71] while using a non-linear force-displacement relationship, suggested in their Adaptive Collision Model (ACM) to stretch the collision time to ten times the flow solver time step. In a similar fashion, [13, 12, 66, 26] used a stretching factor equal to eight.

Combined Modeling

In the presence of a viscous fluid, all the previously discussed collision models, when used in the context of NF-PRDNS methods, need to be coupled with a lubrication model to account for the unresolved dissipative effects of viscous drainage. As previously stated, the implementation of the lubrication model might result in a large number of ad hoc numerical parameters that must be calibrated. For instance, three separate parameters were required in [12]. Additionally, the provided amplification coefficients for the lubrication force are grid dependent. Moreover, [10] showed that dissipation may depend on the gap thickness, suggesting that more investigation is needed in this regard. Finally, for this procedure to be valid, the Stokes flow assumption must be fulfilled within the fluid film separating the two solids. This is only verified if the distance between the two interfaces is significantly smaller than the characteristic length scale of the particles [27]. To correctly solve for viscous dissipation in the fluid film, the mesh would need to be further refined, increasing the computation time.

To address the aforementioned challenges, [83] proposed an alternative strategy that simultaneously accounts for both the dissipative effect in the solid and in the fluid gap. The collision force is modelled using a piecewise linear spring model, i.e., using two different spring stiffness in the loading and unloading phases, vaguely similar to the Hysteretic class of models [117, 122]. To account for the global kinetic energy loss during the collision process, the spring stiffness in the unloading phase is reduced using the apparent coefficient of restitution, leading to the appropriate rebound velocity at the end of the collision.

The spring stiffness in the loading phase is computed using a prescribed maximal distance of indentation, making this distance the only numerical parameter of the model. The proposed model differs from other models in that the rebound velocity of the particles is known before the impact even occurs. This is because the coefficient of restitution used to correct the spring stiffness is calculated from a well-established experimental relationship between the restitution coefficient and the Stokes number [99]. By doing so, this model addresses many of the drawbacks of the previous collision

models. It allows the collision time to be stretched, enabling granular flow simulations to be run for extended times. The model's coefficients are provided explicitly, eliminating the requirement for an iterative solution. No dashpot coefficient is used, which eliminates the nonphysical non-zero collision force at the start and end of the collision. The number of numerical parameters is reduced to one (the maximum indentation distance), since no separate lubrication model is used. Considering the mentioned benefits of this model, we have opted for a modified version of this collision model. The details of our implementation are elaborated in the following chapter.

Collision Force Integration Methods

In the realm of the Discrete Element Method (DEM), the use of explicit methods for the integration of Euler's equations often proves more practical than their implicit counterparts. This preference primarily arises due to the simplicity and reduced computational burden that explicit methods provide, as they do not necessitate solving non-linear equations or inverting matrices - tasks that become computationally intensive for large systems.

Starting with the Explicit Euler method, its primary strength lies in its simplicity and easy implementation. It's a single-step method that needs just one force evaluation per time step. However, this simplicity comes with significant drawbacks. Its numerical stability is heavily dependent on the step size, and it is prone to significant errors in the conservation of energy over long simulations, which makes it less suitable for longer and more precise simulations. The semi-implicit Euler method, or Euler-Cromer, offers a step-up in terms of energy conservation while retaining the simplicity of explicit Euler. It is still a single-step method and uses one force evaluation per time step, but by updating the velocities before the positions, it provides better long-term energy conservation than the explicit Euler method.

The Leapfrog method, aptly named for its 'jumping' over data points, improves on this further. Leapfrog method that decouples position and velocity updates and offers superior stability and energy conservation over the explicit Euler and semi-implicit Euler methods. Permuting between the position and velocity leads to the position Verlet method.

The Velocity Verlet algorithm, an evolution of Position Verlet, reduces these errors by making velocities central to the integration. While it seems that the method requires two force evaluations, the second force evaluation can be stored and used as the first force evaluation in the next time step.

Classical Verlet stands out in terms of memory efficiency, as it only requires storing the current and previous positions. However, this comes with a cost as velocity is not explicitly calculated, which might be an issue if velocities are required for analysis.

3.4. Particle-Particle Interactions Modeling

The Beeman algorithm, a further enhancement of the Verlet family, optimizes the use of acceleration data for updating positions and velocities. It's a single-step method, providing high accuracy for oscillatory motion while using only one more force evaluation than the Velocity Verlet.

On the multi-step front, methods like Adams-Bashforth and Adams-Moulton present. They use information from more than one previous step to predict future values, which can increase accuracy but also memory usage and complexity. Adams-Bashforth is an explicit predictor method, benefiting from more straightforward implementation but suffering from stability issues. On the other hand, Adams-Moulton is an implicit corrector method, which brings increased stability at the cost of computational effort.

3.4. Particle-Particle Interactions Modeling

Table 3.1: Comparison of numerical integration methods

Method Name	Type	Order	Storage	Equation
Forward Euler	SS	1	+0	$\mathbf{u}^{n+1} = \mathbf{u}^n + \mathbf{a}^n \Delta t$ $\mathbf{x}^{n+1} = \mathbf{x}^n + \mathbf{u}^n \Delta t$
Semi-Implicit Euler	SS	1	+0	$\mathbf{u}^{n+1} = \mathbf{u}^n + \mathbf{a}^n \Delta t$ $\mathbf{x}^{n+1} = \mathbf{x}^n + \mathbf{u}^{n+1} \Delta t$
Leapfrog	SS	2	+0	$\mathbf{u}^{n+1/2} = \mathbf{u}^{n-1/2} + \mathbf{a}(\mathbf{x}, \mathbf{u}^{n-1/2}) \Delta t$ $\mathbf{x}^{n+1} = \mathbf{x}^n + \mathbf{u}^{n+1/2} \Delta t$
Position Verlet	SS	2	+0	$\mathbf{x}^{n+1/2} = \mathbf{x}^{n-1/2} + \mathbf{u}^n \Delta t$ $\mathbf{u}^{n+1} = \mathbf{u}^n + \mathbf{a}^n(\mathbf{x}^{n-1/2}, \mathbf{u}^n) \Delta t$
Velocity Verlet	SS	2	+1	$\mathbf{x}^{n+1} = \mathbf{x}^n + \mathbf{u}^n \Delta t + \frac{1}{2} \mathbf{a}^n \Delta t^2$ $\mathbf{u}^{n+1} = \mathbf{u}^n + \frac{1}{2} (\mathbf{a}^{n+1} + \mathbf{a}^n) \Delta t$
Classical Verlet	MS	2	+1	$\mathbf{x}^{n+1} = 2\mathbf{x}^n - \mathbf{x}^{n-1} + \mathbf{a}^n \Delta t^2$ $\mathbf{u}^{n+1} = \frac{\mathbf{x}^{n+1} - \mathbf{x}^{n-1}}{2\Delta t}$
Beeman	MS	2	+1	$\mathbf{x}^{n+1} = \mathbf{x}^n + \mathbf{u}^n \Delta t + \left(\frac{2}{3} \mathbf{a}^n - \frac{1}{6} \mathbf{a}^{n-1} \right) \Delta t^2$ $\mathbf{u}^{n+1} = \mathbf{u}^n + \left(\frac{1}{3} \mathbf{a}^{n+1} + \frac{5}{6} \mathbf{a}^n - \frac{1}{6} \mathbf{a}^{n-1} \right) \Delta t$
Adam Bashforth 2	MS	2	+2	$\mathbf{x}^{n+1} = \mathbf{x}^n + \frac{1}{2} (3\mathbf{u}^n - \mathbf{u}^{n-1}) \Delta t$ $\mathbf{u}^{n+1} = \mathbf{u}^n + \frac{1}{2} (3\mathbf{a}^n - \mathbf{a}^{n-1}) \Delta t$
Adam Moulton 3	PC	3	+5	$\mathbf{u}^{n+1} = \mathbf{u}^n + \frac{1}{12} (5\mathbf{a}^{n+1} + 8\mathbf{a}^n - \mathbf{a}^{n-1})$ $\mathbf{x}^{n+1} = \mathbf{x}^n + \frac{1}{12} (5\mathbf{u}^{n+1} + 8\mathbf{u}^n - \mathbf{u}^{n-1})$

3.4.3 Cohesive Forces

Cohesive forces occur due to the various short-range interactions between particles. These forces can cause particles to aggregate and significantly impact the overall behavior of the particles in the fluid. The primary types of cohesive forces include Van der Waals forces, electrostatic forces, and liquid bridge forces.

Van der Waals forces:

Van der Waals forces emerge from intermolecular interactions between solid surfaces. These forces become particularly significant when we bring very smooth surfaces into close proximity. The force acting between two spheres due to van der Waals interactions can be quantified using [56] :

$$F = \frac{d_e H}{12\pi z^2} \quad (3.30)$$

where F is the force per unit area, while H is the Hamaker constant. z represents the separation distance at the point of contact, a factor determined by the roughness of the sphere. Finally, d_e is the effective diameter:

$$d_e = \frac{d_{p1} d_{p2}}{d_{p1} + d_{p2}} \quad (3.31)$$

To get the force between a sphere and a flat plate, the same equation can be used with $d_e = d_p$ (the plate is considered as a sphere of infinite diameter). The Hamaker constant H for different materials in a fluid medium can be expressed as:

$$H = \left(\sqrt{H_{p1}} - \sqrt{H_f} \right) \left(\sqrt{H_{p2}} - \sqrt{H_f} \right) \quad (3.32)$$

Electrostatic forces:

Electrostatic forces originate from interactions between charged particles. In fluids, particles can gain a surface charge via ion adsorption, resulting in either attractive or repulsive interactions, depending on the sign of the charges. The force between two charged particles can be calculated using Coulomb's law:

$$F = \frac{1}{4\pi\epsilon_0} \frac{q_1 q_2}{L^2} \quad (3.33)$$

Where q_1 and q_2 are the charges on the particles, ϵ_0 is the vacuum permittivity, and L is the distance between particle centers. For identically-sized particles in direct contact, the cohesive force between them is given by:

$$F = \frac{\pi\sigma_1\sigma_2}{\epsilon_0} d_p^2 \quad (3.34)$$

3.4. Particle-Particle Interactions Modeling

Here, σ_1 and σ_2 represent the charge densities of the particles. This equation assumes uniformly charged particles with effective charge concentrated at their centers. Interestingly, particle size has a greater effect on the Coulomb cohesive force than the van der Waals force [28].

Liquid bridge forces:

Under conditions of high humidity, condensation can lead to the formation of a liquid bridge between particles. The surface of this liquid exhibits a concave shape due to surface tension, creating a region of negative pressure within the bridge. The force exerted on a particle is a combination of this negative pressure force and the cohesive force generated by capillarity. The magnitude of this force can be calculated using the Laplace-Young equation:

$$F = \pi a_2^2 f_\sigma \left(\frac{1}{a_1} + \frac{1}{a_2} \right) + 2\pi a_2 f_\sigma \cos \theta \quad (3.35)$$

In this equation, a_1 denotes the radius of curvature of the bridge, while a_2 refers to the radius of the liquid bridge itself. f_σ is the capillary force, and θ is the contact angle between the liquid and the surface of the particle.

4

NUMERICAL METHOD

4.1 Presentation of the TrioCFD Framework

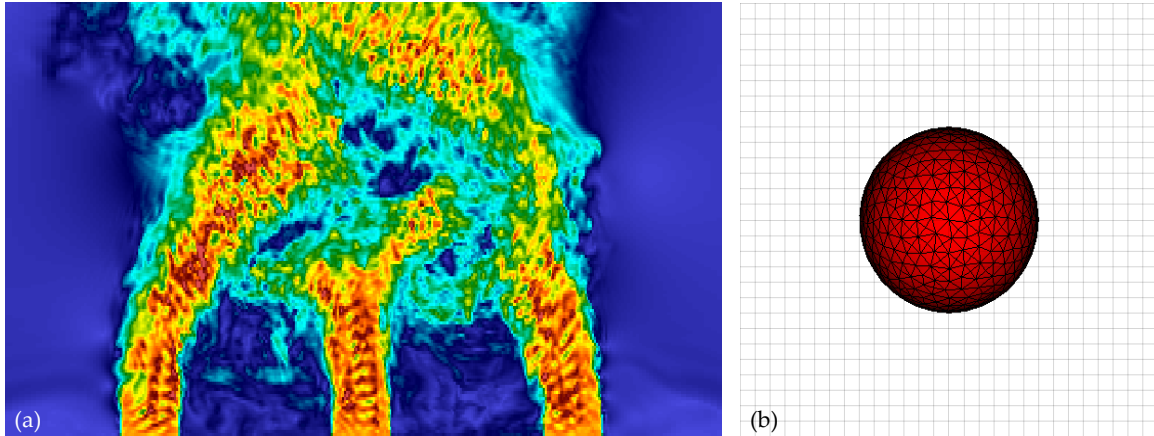


Figure 4.1: Illustration of mixed method FT/VOF in TrioCFD

In this work, the TrioCFD simulation software (formerly known as TrioU) is utilized. This code is based on the TRUST platform and is an open-source, object-oriented code written in C++ that features an intrinsic management of parallelism. Developed by the CEA, it is specifically designed for industrial CFD applications on structured (parallelepipeds) or unstructured (tetrahedrons) meshes containing up to several hundred million elements (Fig 4.1a). TrioCFD has been proven to be successful in simulations on supercomputers, with the ability to perform LES simulations, single-phase DNS, and two-phase DNS (liquid-gas) simulations utilizing up to 10,000 processors [109, 3, 39, 38, 35, 37, 36].

To simulate multiphase flow, the TrioCFD simulation code utilizes the one-fluid formalism of the Navier-Stokes equations combined with a Front-Tracking/VOF techniques for managing the transport of interfaces.

In this work, the governing equations are solved with a VDF discretization on a staggered mesh (Fig. 4.1b).

4.2 Deriving the One-Fluid Formulation

In order to derive the One-Fluid equations for the fluid-solid problem, we will first derive individual fluid equations for each phase, considering them both as fluids. The appropriate jump conditions at the interface dividing the two phases will also be derived.

4.2.1 Two-fluids equations derivation

Let's consider Ω_0 , an immaterial control volume of arbitrary shape, *fixed in space* such that it is intersected by the biphasic interface, as illustrated in the Fig. 4.2:

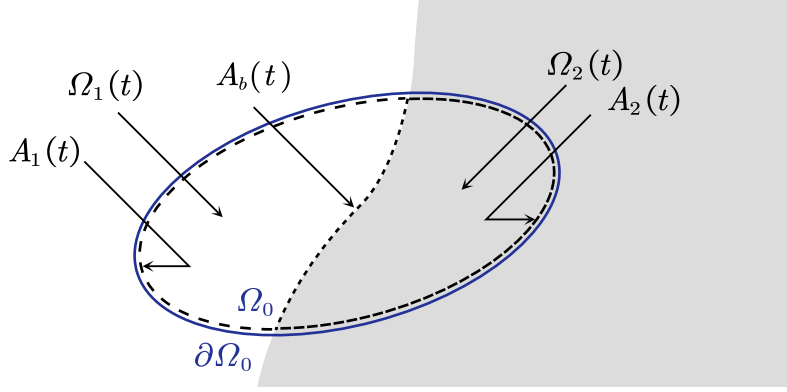


Figure 4.2: Biphasic control volume.

The control volume Ω_0 is constituted of two sub-volumes: $\Omega_1(t)$ and $\Omega_2(t)$, corresponding respectively to fluid 1 and fluid 2. These two sub-volumes are separated by an immaterial interface of surface area $A_b(t)$, which is free to move with velocity \mathbf{u}_b . The closed boundaries, $\partial\Omega_1(t)$ and $\partial\Omega_2(t)$, for the sub-volumes $\Omega_1(t)$ and $\Omega_2(t)$ respectively, are described through the following relations:

$$\begin{aligned}
 \Omega_0 &= \Omega_1(t) + \Omega_2(t) \\
 \partial\Omega_0 &= A_1(t) + A_2(t) \\
 \partial\Omega_1(t) &= A_1(t) + A_b(t) \\
 \partial\Omega_2(t) &= A_2(t) + A_b(t)
 \end{aligned} \tag{4.1}$$

To derive the phase equations and the corresponding jump conditions, we will apply the conservation principle over the control volume Ω_0 , and express the balance for the two sub-volumes, Ω_1 and Ω_2 , using the general balance equation provided by Delhaye [31]:

$$\{\text{Rate of change}\} = \{\text{Net convection}\} + \{\text{Net diffusion}\} + \{\text{Production/Destruction}\}$$

$$\sum_{k=1,2} \frac{d}{dt} \int_{\Omega_k(t)} \rho_k \Psi_k dV = - \sum_{k=1,2} \int_{\partial\Omega_k(t)} \rho_k \Psi_k (\mathbf{u}_k \cdot \mathbf{n}_k) dS + \sum_{k=1,2} \int_{\partial\Omega_k(t)} \mathbf{J}_k dS + \sum_{k=1,2} \int_{\Omega_k(t)} \rho_k \Phi_k dV \tag{4.2}$$

4.2. Deriving the One-Fluid Formulation

Conserved quantity	Ψ_k	Φ_k	J_k
Mass	1	0	0
Linear momentum	\mathbf{u}_k	\mathbf{f}	\mathbf{t}_k

Table 4.1: Term expression for the equation balance

The terms Ψ_k , Φ_k , and J_k are selected from Table 4.1, and their choice depends on the particular type of balance we aim to express. In this table, \mathbf{f} represents body forces, $\mathbf{t}_k = \boldsymbol{\sigma}_k \cdot \mathbf{n}_k$ is the traction vector or the surface forces while $\boldsymbol{\sigma}_k$ is the total stress tensor, given by:

$$\boldsymbol{\sigma}_k = -p_k \mathbf{I} + \boldsymbol{\tau}_k \quad (4.3)$$

In this formulation, p_k is the phase pressure, \mathbf{I} the identity tensor, and $\boldsymbol{\tau}_k$ the viscous stress tensor, expressed for an incompressible Newtonian fluid as:

$$\boldsymbol{\tau}_k = 2\mu_k \mathbf{D}[\mathbf{u}_k] \quad (4.4)$$

μ_k is the dynamic viscosity and $\mathbf{D}[\mathbf{u}_k]$ is the strain rate tensor that quantifies the rate of deformation:

$$\mathbf{D}[\mathbf{u}_k] = \frac{1}{2} (\nabla \mathbf{u}_k + \nabla^t \mathbf{u}_k) \quad (4.5)$$

Conservation of mass

To derive the conservation of mass equation, we use 4.2 along with the parameters from the first line of 4.1.

$$\sum_{k=1,2} \frac{d}{dt} \int_{\Omega_k(t)} \rho_k dV = - \sum_{k=1,2} \int_{A_k(t)} \rho_k \mathbf{u}_k \cdot \mathbf{n}_k dS \quad (4.6)$$

Next, by employing Leibniz's rule on the rate of change, we obtain the following expression:

$$\frac{d}{dt} \int_{\Omega_k(t)} \rho_k dV = \int_{\Omega_k(t)} \frac{\partial \rho_k}{\partial t} dV + \int_{A_b(t)} \rho_k \mathbf{u}_b \cdot \mathbf{n}_k dS$$

We then apply Gauss's theorem to the convective term. This allows us to transform the surface integral into a volume integral, as shown below:

$$\int_{A_k(t)} \rho_k \mathbf{u}_k \cdot \mathbf{n}_k dS = \int_{\Omega_k(t)} \nabla \cdot \rho_k \mathbf{u}_k dV - \int_{A_b(t)} \rho_k \mathbf{u}_k \cdot \mathbf{n}_k dS$$

4.2. Deriving the One-Fluid Formulation

Substituting these results back into our initial mass conservation Eq. (4.6) and rearranging:

$$\sum_{k=1,2} \int_{\Omega_k(t)} \left(\frac{\partial \rho_k}{\partial t} + \nabla \cdot \rho_k \mathbf{u}_k \right) dV = \int_{A_b(t)} \sum_{k=1,2} [\rho_k (\mathbf{u}_k - \mathbf{u}_b) \cdot \mathbf{n}_k] dS \quad (4.7)$$

Given that the control volumes and the boundary separating them are arbitrary, the integrands of Eq. (4.7) must be equal to zero. This leads us to two important equations, one for local mass balance within each phase and another for the balance of mass equation at the interface, often referred to as the jump condition:

$$\left\{ \begin{array}{l} \frac{\partial \rho_k}{\partial t} + \nabla \cdot \rho_k \mathbf{u}_k = 0 \\ \sum_{k=1,2} \rho_k (\mathbf{u}_k - \mathbf{u}_b) \cdot \mathbf{n}_k = 0 \end{array} \right. \quad (k = 1, 2) \quad (4.8a)$$

$$(4.8b)$$

The quantity $\rho_k (\mathbf{u}_k - \mathbf{u}_b) \cdot \mathbf{n}_k$ represents the mass flux per unit area \dot{m}_k . Hence, we can rewrite the jump condition in terms of the mass fluxes from the two phases:

$$\dot{m}_1 = -\dot{m}_2 \quad (4.9)$$

If there's no phase change occurring in the system, the mass flux will be zero, which results in the following condition for the velocities:

$$(\mathbf{u}_k - \mathbf{u}_b) \cdot \mathbf{n}_k = 0 \quad (4.10)$$

Summing over k we get:

$$\sum_{k=1,2} \mathbf{u}_k \cdot \mathbf{n}_k = 0 \quad (4.11)$$

This equation shows that in the absence of phase change, the normal phase velocities at the interface must be equal:

$$\mathbf{u}_1 \cdot \mathbf{n}_k = \mathbf{u}_2 \cdot \mathbf{n}_k \quad (4.12)$$

This relationship is also referred to as the no-penetration boundary condition.

Lastly, if we assume a no-slip condition at the interface (tangential velocities at the interface are equal), which is applicable for the types of flows discussed in this study, we obtain the kinematic boundary condition on the velocity.:

$$\mathbf{u}_1 = \mathbf{u}_2 \quad (4.13)$$

4.2. Deriving the One-Fluid Formulation

Conservation of Linear momentum

Following the approach used in the previous section, we will establish equations for the conservation of linear momentum. We start by using Eq. (4.2) and the parameters from the second line of Table 4.1:

$$\begin{aligned} \sum_{k=1,2} \frac{d}{dt} \int_{\Omega_k(t)} \rho_k \mathbf{u}_k dV &= - \sum_{k=1,2} \int_{A_k(t)} \rho_k \mathbf{u}_k (\mathbf{u}_k \cdot \mathbf{n}_k) dS + \sum_{k=1,2} \int_{A_k(t)} \boldsymbol{\sigma}_k \cdot \mathbf{n}_k dS \\ &+ \sum_{k=1,2} \int_{\Omega_k(t)} \rho_k \mathbf{f} dV \end{aligned} \quad (4.14)$$

Next, Leibniz's rule is applied to the rate of change, yielding the following expression:

$$\frac{d}{dt} \int_{\Omega_k(t)} \rho_k \mathbf{u}_k dV = \int_{\Omega_k(t)} \frac{\partial \rho_k \mathbf{u}_k}{\partial t} dV + \int_{A_b(t)} \rho_k \mathbf{u}_k (\mathbf{u}_b \cdot \mathbf{n}_k) dS \quad (4.15)$$

Afterwards, we invoke Gauss's theorem on the convective and diffusive terms to transform the surface integrals into volume integrals:

$$\begin{aligned} \int_{A_k(t)} \rho_k \mathbf{u}_k (\mathbf{u}_k \cdot \mathbf{n}_k) dS &= \int_{A_k(t)} (\rho_k \mathbf{u}_k \mathbf{u}_k) \cdot \mathbf{n}_k dS \\ &= \int_{\Omega_k(t)} \nabla \cdot (\rho_k \mathbf{u}_k \mathbf{u}_k) dV - \int_{A_b(t)} \rho_k \mathbf{u}_k (\mathbf{u}_k \cdot \mathbf{n}_k) dS \\ \int_{A_k(t)} \boldsymbol{\sigma}_k \cdot \mathbf{n}_k dS &= \int_{\Omega_k(t)} \nabla \cdot \boldsymbol{\sigma}_k dV - \int_{A_b(t)} \boldsymbol{\sigma}_k \cdot \mathbf{n}_k dS \end{aligned}$$

Substituting these results back and rearranging:

$$\begin{aligned} \sum_{k=1,2} \int_{\Omega_k(t)} \left(\frac{\partial \rho_k \mathbf{u}_k}{\partial t} + \nabla \cdot (\rho_k \mathbf{u}_k \mathbf{u}_k) - \rho_k \mathbf{f} - \nabla \cdot \boldsymbol{\sigma}_k \right) dV \\ = \int_{A_b(t)} \sum_{k=1,2} [\rho_k \mathbf{u}_k (\mathbf{u}_k - \mathbf{u}_b) \cdot \mathbf{n}_k - \boldsymbol{\sigma}_k \cdot \mathbf{n}_k] dS \end{aligned} \quad (4.16)$$

Given that the control volumes and the boundary separating them are arbitrary, the integrands of this equation must be null.

$$\left\{ \begin{aligned} \frac{\partial \rho_k \mathbf{u}_k}{\partial t} + \nabla \cdot (\rho_k \mathbf{u}_k \mathbf{u}_k) - \rho_k \mathbf{f} - \nabla \cdot \boldsymbol{\sigma}_k &= 0 & (k = 1, 2) & \quad (4.17a) \end{aligned} \right.$$

$$\left\{ \begin{aligned} \sum_{k=1,2} [\rho_k \mathbf{u}_k (\mathbf{u}_k - \mathbf{u}_b) \cdot \mathbf{n}_k - \boldsymbol{\sigma}_k \cdot \mathbf{n}_k] &= 0 & \quad (4.17b) \end{aligned} \right.$$

The first equation is the local linear momentum balance within each phase, and the second is the jump condition at the interface, also known as the dynamic boundary condition. Again, in the absence of phase change, the jump condition simplifies to:

$$\boldsymbol{\sigma}_1 \cdot \mathbf{n}_1 = -\boldsymbol{\sigma}_2 \cdot \mathbf{n}_2 \quad (4.18)$$

4.2.2 One-fluid equations derivation

The individual phase equations for each separate phase and the corresponding boundary conditions are given in Eq. (4.19). We consider the fluid phase as an incompressible fluid (Eq. (4.19b)), whereas the solid phase is modeled as a fluid adhering to rigidity constraints (Eq. (4.19d)). The no-slip and no-penetration conditions give rise to the corresponding kinematic and dynamic boundary conditions (Eqs. (4.19e) and (4.19f) respectively):

$\frac{\partial \rho_f \mathbf{u}_f}{\partial t} + \nabla \cdot (\rho_f \mathbf{u}_f \mathbf{u}_f) = \nabla \cdot \boldsymbol{\sigma}_f + \rho_f \mathbf{f}$	in Ω_f ,	(4.19a)
$\nabla \cdot \mathbf{u}_f = 0$	in Ω_f ,	(4.19b)
$\frac{\partial \rho_s \mathbf{u}_s}{\partial t} + \nabla \cdot (\rho_s \mathbf{u}_s \mathbf{u}_s) = \nabla \cdot \boldsymbol{\sigma}_s + \rho_s \mathbf{f}$	in Ω_s ,	(4.19c)
$\mathbf{D}[\mathbf{u}_s] = 0$	in Ω_s ,	(4.19d)
$\mathbf{u}_f = \mathbf{u}_s$	on $\partial\Omega_s$,	(4.19e)
$\boldsymbol{\sigma}_f \cdot \mathbf{n}_f = -\boldsymbol{\sigma}_s \cdot \mathbf{n}_s$	on $\partial\Omega_s$	(4.19f)

To extend these equations to the entire domain, we introduce the phase indicator function, defined as:

$$\chi_k = \begin{cases} 1 & \text{in } \Omega_k \\ 0 & \text{elsewhere} \end{cases} \quad (4.20)$$

This function serves as a flag for the phase presence. Several key properties of the indicator function include Kataoka [70] and Tryggvason, Scardovelli, and Zaleski [110]:

$$\nabla \chi_k = -\mathbf{n}_k \delta_b \quad (4.21a)$$

$$\chi_k \chi_k = \chi_k \quad (4.21b)$$

$$\sum_k \chi_k = 1 \quad (4.21c)$$

As the interface moves, each fluid's occupied region shape alters, and χ_k adjusts accordingly. This means the material derivative of χ_k is zero, providing the transport equation for χ_k :

$$\frac{\partial \chi_k}{\partial t} + \mathbf{u}_b \cdot \nabla \chi_k = 0 \quad (4.22)$$

4.2. Deriving the One-Fluid Formulation

To establish the one-fluid formulation, we first multiply each phase's governing equation with its corresponding phase indicator function:

$$\chi_k \nabla \cdot \mathbf{u}_k = 0 \quad (4.23a)$$

$$\chi_k \frac{\partial \rho_k \mathbf{u}_k}{\partial t} + \chi_k \nabla \cdot (\rho_k \mathbf{u}_k \mathbf{u}_k) = \chi_k \nabla \cdot \boldsymbol{\sigma}_k + \chi_k \rho_k f \quad (4.23b)$$

We can refer to the following identity of the divergence operator:

$$\nabla \cdot (\varphi \mathbf{A}) = \varphi \nabla \cdot \mathbf{A} + \mathbf{A} \cdot \nabla \varphi \quad (4.24)$$

φ represents a scalar function, and \mathbf{A} can be either a vector or a second-order tensor. By utilizing Eq. (4.24) alongside the transport equation of χ_k Eq. (4.22), we can rework each term in Eq. (4.23) as follows:

$$\begin{aligned} \chi_k \nabla \cdot \mathbf{u}_k &= \nabla \cdot (\chi_k \mathbf{u}_k) - \mathbf{u}_k \cdot \nabla \chi_k \\ \chi_k \frac{\partial \rho_k \mathbf{u}_k}{\partial t} &= \frac{\partial \chi_k \rho_k \mathbf{u}_k}{\partial t} - \rho_k \mathbf{u}_k \frac{\partial \chi_k}{\partial t} \\ &= \frac{\partial \chi_k \rho_k \mathbf{u}_k}{\partial t} + \rho_k \mathbf{u}_k (\mathbf{u}_b \cdot \nabla \chi_k) \\ \chi_k \nabla \cdot (\rho_k \mathbf{u}_k \mathbf{u}_k) &= \nabla \cdot (\chi_k \rho_k \mathbf{u}_k \mathbf{u}_k) - \rho_k \mathbf{u}_k \mathbf{u}_k \cdot \nabla \chi_k \\ \chi_k \nabla \cdot \boldsymbol{\sigma}_k &= \nabla \cdot (\chi_k \boldsymbol{\sigma}_k) - \boldsymbol{\sigma}_k \cdot \nabla \chi_k \end{aligned}$$

By inserting these terms back into Eq. (4.23), replacing $\nabla \chi_k$ using Eq. (4.21a), summing the phase equation over $k = 1, 2$, and rearranging, we obtain:

$$\nabla \cdot \left(\sum_{k=1,2} \chi_k \mathbf{u}_k \right) + \sum_{k=1,2} [\mathbf{u}_k \cdot \mathbf{n}_k] \delta_b = 0 \quad (4.25a)$$

$$\begin{aligned} \frac{\partial}{\partial t} \left(\sum_{k=1,2} \chi_k \rho_k \mathbf{u}_k \right) + \nabla \cdot \left(\sum_{k=1,2} \chi_k \rho_k \mathbf{u}_k \mathbf{u}_k \right) &= \nabla \cdot \left(\sum_{k=1,2} \chi_k \boldsymbol{\sigma}_k \right) + \sum_{k=1,2} \chi_k \rho_k f \\ &\quad - \sum_{k=1,2} [\rho_k \mathbf{u}_k (\mathbf{u}_k - \mathbf{u}_b) \cdot \mathbf{n}_k - \boldsymbol{\sigma}_k \cdot \mathbf{n}_k] \delta_b \end{aligned} \quad (4.25b)$$

We introduce a "One-fluid" property, ϕ , based on the single-phase properties, ϕ_k (where ϕ can be \mathbf{u} , $\boldsymbol{\sigma}$, ρ , μ , p):

$$\phi = \sum_{k=1,2} \chi_k \phi_k \quad (4.26)$$

To simplify the notation in the case of a two-phase flow between a solid phase s and a fluid phase f , we introduce a color function I called the phase indicator function, set equal to $I = \chi_s = 1 - \chi_f$. This leads to the following definition for I :

$$I(\mathbf{x}) = \begin{cases} 1 & \text{if } \mathbf{x} \in \Omega_s \\ 0 & \text{if } \mathbf{x} \in \Omega_f \end{cases} \quad (4.27)$$

4.2. Deriving the One-Fluid Formulation

The one-fluid properties are then expressed as a function of I with:

$$\begin{aligned}\rho(I) &= I\rho_s + (1 - I)\rho_f \\ \mu(I) &= I\mu_s + (1 - I)\mu_f\end{aligned}\tag{4.28}$$

Utilizing the property from Eq. (4.21b), we rewrite the equation in terms of the one-fluid properties, and by simultaneously applying the jump equations (Eqs. (4.8b), (4.11) and (4.17b)) to remove the Dirac delta function, δ_b , we finally derive the one-fluid equations system:

$$\nabla \cdot \mathbf{u} = 0 \tag{4.29a}$$

$$\frac{\partial \rho \mathbf{u}}{\partial t} + \nabla \cdot (\rho \mathbf{u} \mathbf{u}) = -\nabla p + \nabla \cdot \left(\mu \left(\nabla \mathbf{u} + \nabla^T \mathbf{u} \right) \right) + \rho \mathbf{f} \tag{4.29b}$$

$$\frac{\partial I}{\partial t} + \mathbf{u}_b \cdot \nabla I = 0 \tag{4.29c}$$

4.2.3 Advection of the interface: The front-tracking method.

Despite the apparent simplicity of Eq 4.29c, numerically integrating the transport equation of a piecewise constant function is a challenging task. To address this challenge, several methods such as the volume-of-fluid (VOF) method, the level-set method have emerged. The reader is referred to Tryggvason, Scardovelli, and Zaleski [110] for a review on the subject. In this work we will focus on one method in particular, i.e. the Front Tracking method [15]. To solve the transport equation of the phase indicator function, the Front-Tracking method utilizes two distinct meshes: a fixed, Eulerian mesh for computing velocity and pressure, and a moving, Lagrangian mesh composed of massless markers nodes. The triangles (segments in 2D) formed by the interconnection of the markers points are called the elements of the mesh (see Fig. 4.3). The interface velocity is computed by interpolating the Eulerian velocities at the Lagrangian marker locations. This uses a tri-linear interpolation in 3D (or bi-linear in 2D, as seen in Fig. 4.3a). The resulting element velocities are given by $\hat{\mathbf{u}}_j^{n+1}$:

$$\hat{\mathbf{u}}_j^{n+1} = \frac{1}{3} \sum_{i=1}^3 \hat{\mathbf{u}}_i^{n+1} \tag{4.30}$$

where $\hat{\mathbf{u}}_i^{n+1}$ is the velocity vector associated to the i^{th} marker of the Lagrangian mesh after interpolation. The element velocities are then combined into a single global mesh velocity \mathbf{u}_m^{n+1} through an Area Weighted Average:

$$\mathbf{u}_m^{n+1} = \frac{\sum S_j \hat{\mathbf{u}}_j^{n+1}}{\sum S_j} \tag{4.31}$$

4.2. Deriving the One-Fluid Formulation

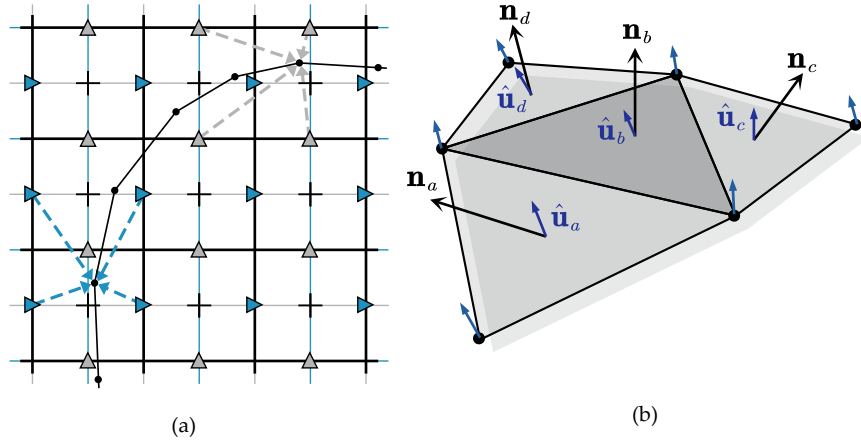


Figure 4.3: Graphical representation of resolution meshes (a) fixed mesh, (b) moving mesh

where S_j is the area of the j^{th} Lagrangian element. This velocity is then used to translate the markers to their new position:

$$\mathring{\mathbf{x}}_i^{n+1} = \mathring{\mathbf{x}}_i^n + \Delta t \mathbf{u}_m^{n+1} \quad (4.32)$$

The phase indicator function is calculated from the new front position, and the thermo-physical property fields of each phase are updated accordingly.

In TrioCFD, the Front-Tracking method, which alone lacks conservation properties, is paired with a VOF algorithm to ensure the mass is preserved during the transport of interfaces. However, as the focus of this study is on solid-fluid flows with rigid two-phase interfaces, the volume of the dispersed phase is automatically conserved and the VOF component is not necessary. Additionally, the bulk translation of the Lagrangian markers eliminates the need for the expensive remeshing algorithms for which the Front-Tracking algorithm is infamous.

Moreover, the software was designed primarily for gas and liquid simulations, where it handled air bubbles as a collective group and assigned a random and temporary ID to each bubble at every timestep. However, as we transitioned to solid and fluid simulations, it became crucial to continuously track each particle over time for accurate force calculations. To accomplish this, we ensured that every particle maintained a unique and consistent ID throughout the simulation. We implemented a caching system that stored each particle's previous position along with its ID and resolved any labeling inconsistencies. This approach is based on the assumption that particles undergo relatively small movements between timesteps compared to their radii.

4.2.4 Solid Rigidity Constraint: Viscous Penalization

In order to impose the constraint of non-deformation within the solid phase, we utilized the Eulerian formulation of this constraint (Eq. (3.7)). This formulation represents a local constraint that can be directly imposed on the conservation of momentum equations (Eq. (4.29b)) without requiring prior knowledge of the velocity of the solid. By imposing a high value of viscosity, it is possible to make the deformation tensor tend towards zero, effectively treating the solid as a highly viscous fluid. The constraint is most effectively imposed when the ratio between solid viscosity and fluid viscosity, $R_\mu = \mu_s / \mu_f$, is large. This approach greatly simplifies the coupling between the dispersed and carrier phases, as the solid's inertia is implicitly accounted for by the fluid solver. Additionally, the rigidity constraint is stricter than the continuity constraint, as a consequence the later is automatically satisfied within the solid phase.

4.2.5 Modeling of the one-fluid physical properties at the interface

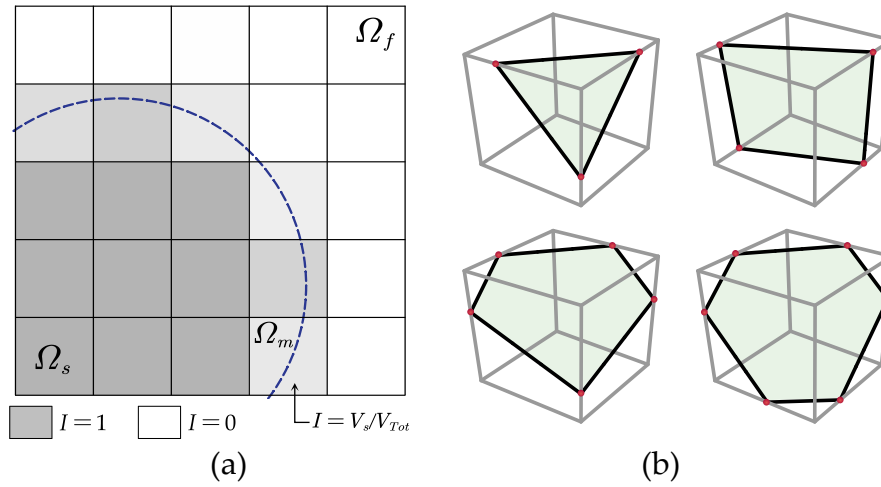


Figure 4.4: (a) Phase indicator schematic for the Front Tracking algorithm: purely solid cells (dark grey), purely fluid cells (white), and interface-crossed cells or mixed cells (gradient grey based on solid volume fraction). (b) Intersection of the Lagrangian and Eulerian meshes, demonstrating the determination of volume fractions from their relative positioning.

In the current method, the interface between the solid and fluid phases is smoothed over one grid cell, resulting in the formation of a third zone that contains both phases simultaneously. We will refer to it in this text as the mixed zone Ω_m . The solid phase indicator function is calculated by evaluating geometrically the solid volume fraction at that location Fig. 4.4:

$$I(\mathbf{x}) = \frac{V_s}{V_c} \quad \text{if } \mathbf{x} \in \Omega_m \quad (4.33)$$

4.3. Particle-particle interactions: Collision modeling

Where, V_c and V_s are the volume of the mixed cell and the volume of the solid phase present in that cell respectively. The evaluation of physical properties over Ω_m is crucial for mass conservation and the calculation of the viscous stresses. The density calculation is straightforward and identical to Eq. (4.28):

$$\rho = I\rho_s + (1 - I)\rho_f$$

However, the viscosity calculation is more challenging due to the high viscosity ratio required by the viscous penalization method. Using an arithmetic average, like for the density will result in $\mu \approx I\mu_s$, regardless of the volume fraction of solid in the mixed cells. This leads to the diffusion of the interface from a hydrodynamic perspective, resulting in an apparent particle surface that is larger than the actual surface. A more accurate approach, which ensures the stress tensor continuity and a proper representation of the hydraulic surface, consist in using a harmonic average [110, 90]:

$$\mu = \frac{\mu_s\mu_f}{I\mu_f + (1 - I)\mu_s} \quad (4.34)$$

While this formulation is an improvement over the previous one, its implementation in our calculation code occasionally led to an overestimation of the hydraulic diameter (interpreted as the effective diameter influencing the fluid drag on the particle). To reduce the drag force exerted on the particle, we used the step function, defined by Eq. (4.35), to calculate the local viscosity. This approach, when paired with the appropriate mesh resolution, allows for a more precise calibration of the hydrodynamic drag, especially in scenarios where harmonic averaging fell short of achieving the desired accuracy.

$$\mu = \begin{cases} \mu_s & \text{if } I = 1 \\ \mu_f & \text{if } I < 1 \end{cases} \quad (4.35)$$

4.3 Particle-particle interactions: Collision modeling

The solid phase has a much shorter characteristic time than the fluid phase, which ordinarily would necessitate an extremely small simulation time step for accurate representation. However, as discussed in [13, 12, 26] the collision time can be extended up to several times the fluid simulation time step without sacrificing physical realism. This approach, combined with the simultaneous modeling of both the collision and lubrication forces proposed by Mohaghegh and Udaykumar [83], serves as the basis for the collision model that was implemented in this work.

4.3.1 Particle-particle collisions

The model is built on a harmonic oscillator, which is a mass-spring system with no damping. Consider an *elastic collision* between two particles, p and q , with radii R_p and R_q , respectively. For clarity, particle q will be maintained stationary in space ($\mathbf{u}_q = 0$). The collision force, $F_{c,q \rightarrow p}$, exerted by particle q on particle p in the normal direction is modeled as a force of the following form:

$$\mathbf{F}_{c,q \rightarrow p} = -k\delta_n \mathbf{n} \quad (4.36)$$

where k represents the stiffness constant of the oscillator, δ_n is the normal distance separating the surfaces of the two particles defined by:

$$\delta_n = \|\mathbf{x}_p - \mathbf{x}_q\| - (R_p + R_q) \quad (4.37)$$

where \mathbf{x}_p and \mathbf{x}_q are the centers of gravity of particles p and q , respectively. The vector \mathbf{n} represents the normal to the contact plane of the two surfaces:

$$\mathbf{n} = \frac{\mathbf{x}_p - \mathbf{x}_q}{\|\mathbf{x}_p - \mathbf{x}_q\|} \quad (4.38)$$

The equation of motion for the overlapping distance δ_n in the normal direction is:

$$m_{eff} \ddot{\delta}_n + k\delta_n = 0 \quad (4.39)$$

where m_{eff} is the reduced mass of the two interacting particles:

$$\frac{1}{m_{eff}} = \frac{1}{m_p} + \frac{1}{m_q}$$

The solution of the differential equation Eq. (4.39) is:

$$\delta_n(t) = \delta_{max} \sin(\omega_0 t + \phi) \quad (4.40)$$

δ_{max} and ϕ are the amplitude and the phase of the harmonic oscillator:

$$\delta_{max} = \frac{\sqrt{\omega_0^2 x_0^2 + v_0^2}}{\omega_0} \quad \phi = \tan^{-1} \left(\frac{\omega_0 x_0}{v_0} \right)$$

$x_0 = \delta_n(t = 0s)$ and $v_0 = \dot{\delta}_n(t = 0s)$ are the initial conditions for the displacement and the velocity respectively.

ω_0 is the natural frequency of the oscillator given by:

$$\omega_0 = \frac{2\pi}{T} = \sqrt{\frac{k}{m_{eff}}}$$

4.3. Particle-particle interactions: Collision modeling

where T is the oscillation period of the system. By noting the collision period τ_c equal to $\tau_c = T/2$ we can deduce the expression of the spring constant k :

$$k = m_{eff} \left(\frac{\pi}{\tau_c} \right)^2 \quad (4.41)$$

From a physical point of view, collisions are never purely elastic. A portion of the initial kinetic energy is lost both as vibrational energy in the solid and as viscous dissipation in the fluid (when they are not negligible). To account for these *inelastic losses*, the combined modeling approach of Mohaghegh and Udaykumar [83] was preferred. In this approach, we rely on the existing relationship between the St number and the coefficient of restitution e to predict the particle speed at the end of the collision. The difference in kinetic energy between the impact and the rebound will serve to relax the stiffness constant k to obtain the desired speed at the end of the collision. The derivation of the correction factor for the spring stiffness is detailed in the following:

The motion of the particle during the collision goes through three key moments (see Fig. 4.5):

- The start of the collision, represented by t_{imp} , which marks the moment when the surfaces of two particles first come into contact, and the overlapping distance δ_n becomes negative ($\delta_n(t_{imp}) < 0$).
- The spring correction time, represented by t_{corr} , which marks the moment during the collision when the particle's velocity reaches zero as its kinetic energy is completely converted into elastic potential energy stored in spring k . At this point, $\delta_n(t_{corr}) = \delta_{max}$, and the spring stiffness is reduced from k to k' .
- The end of the collision, represented by t_{reb} , when the surfaces of the two particles are no longer in contact, and thus the overlapping distance δ_n becomes positive again ($\delta_n(t_{reb}) > 0$).

By noting $u_{imp} = \|\mathbf{u}_p(t_{imp})\|$ the velocity of the particle p when it's impacting the particle q , we can compute the St at that instant:

$$St_{imp} = \frac{2 R_{eff} \rho_s}{9 \mu_f} u_{imp} \quad (4.42)$$

Here, R_{eff} is the effective diameter, which is calculated by $R_{eff} = (R_p^{-1} + R_q^{-1})^{-1}$. Using the definition of coefficient of restitution, $e = u_{reb}/u_{imp}$ we can deduce the rebound velocity $u_{reb} = \|\mathbf{u}_p(t_{reb})\|$ of the particle p at the end of the collision:

$$\mathbf{u}_{reb}(St_{imp}) = e(St_{imp}) \mathbf{u}_{imp} \quad (4.43)$$

The kinetic energy lost by the particle p after the collision is given by:

$$\Delta E_k = \frac{1}{2} m_p (u_{imp}^2 - u_{reb}^2) = \frac{1}{2} m_p u_{imp}^2 (1 - e^2) \quad (4.44)$$

4.3. Particle-particle interactions: Collision modeling

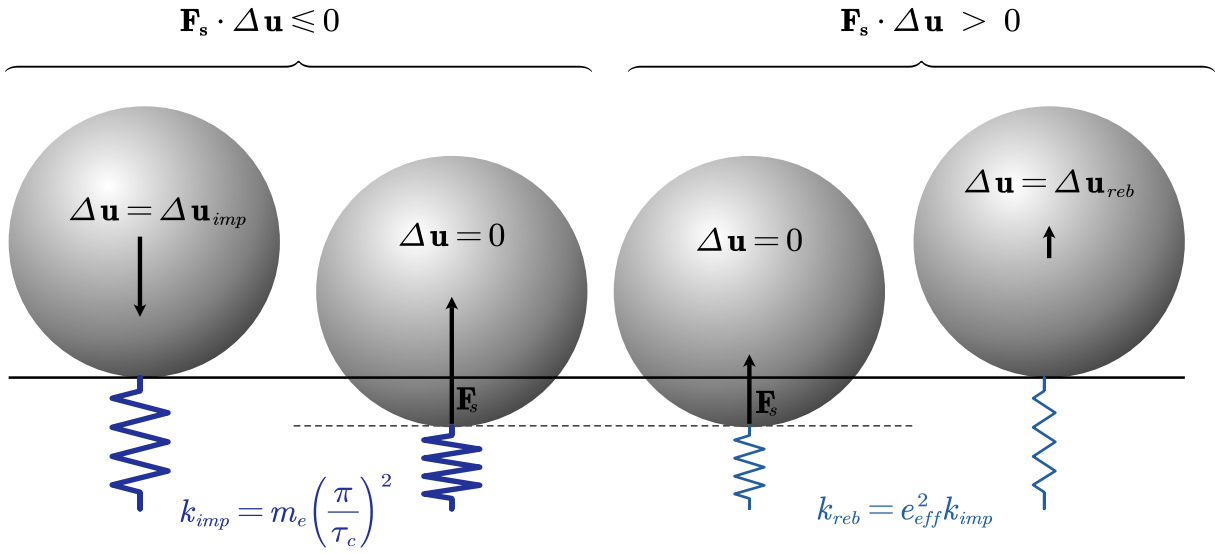


Figure 4.5: Explanatory diagram of the collision model.

The corresponding elastic potential energy reduction is given by:

$$\Delta E'_e = \frac{1}{2} (k - k') \delta_{max}^2 \quad (4.45)$$

Where k' is the reduced spring stiffness we are looking for.

The value of δ_{max}^2 can be obtained from an energy balance between t_{imp} and t_{corr} :

$$\frac{1}{2} m_p u_{imp}^2 = \frac{1}{2} k \delta_{max}^2 \quad (4.46)$$

By equating $\Delta E_k = \Delta E'_e$ and replacing δ_{max}^2 into Eq 4.45 we can write:

$$\frac{1}{2} m_p u_{imp}^2 (1 - e^2) = \frac{1}{2} m_p u_{imp}^2 \left(1 - \frac{k'}{k}\right) \quad (4.47)$$

Finally, solving for k' we find:

$$k' = k e^2 \quad (4.48)$$

Numerically, to identify the moment t_{corr} , we rely on the change of sign of the scalar product $\mathbf{u}_p \cdot \mathbf{n} > 0$. Indeed, when $t < t_{corr}$, the collision force acts against the velocity, resulting in a negative product. While, the product is positive when $t > t_{corr}$ as the collision force acts in the same direction as the velocity. The stiffness can be considered as a piecewise function of the scalar product $\mathbf{u}_p \cdot \mathbf{n}$:

$$k_i = \begin{cases} m_{eff} \left(\frac{\pi}{\tau_c}\right)^2 & \text{if } \mathbf{u}_p \cdot \mathbf{n} \leq 0 \\ e^2 m_{eff} \left(\frac{\pi}{\tau_c}\right)^2 & \text{if } \mathbf{u}_p \cdot \mathbf{n} > 0 \end{cases} \quad (4.49)$$

4.3. Particle-particle interactions: Collision modeling

According to the third Newton law of motion, the reaction force to be applied to the particle q is of equal intensity and opposite direction to the force applied to the particle p :

$$\mathbf{F}_{c,p \rightarrow q} = -\mathbf{F}_{c,q \rightarrow p} \quad (4.50)$$

The forces acting on a particle are summed up and divided by the volume of the particle. Using the corresponding particle phase indicator function, the resulting force is then applied to the purely solid cells belonging to that particle. For the particle p this gives:

$$\mathbf{F}(\mathbf{x}) = I_p(\mathbf{x}) \sum_q \frac{\mathbf{F}_{c,q \rightarrow p}}{V_p} \quad \text{with } \mathbf{x} \in \Omega_{s,p} \quad (4.51)$$

4.3.2 Time integration of the collision force

For each pair of particles, we test for collisions by calculating the overlap distance ($\delta_n \leq 0$), and the forces are updated until no overlapping is observed. The time integration of the collision force is done using a variant of the Semi-Implicit Euler time scheme (SIE) to prevent numerical divergences caused by the Forward Euler scheme (FE):

$$\mathbf{F}_c^{n+1} = -k_i^n \delta_n^{n+1} \mathbf{n} \quad (4.52)$$

where k_i^n is the piecewise stiffness evaluated with the scalar product ($\mathbf{u}_p \cdot \mathbf{n}$) at time n . \mathbf{n} is given by Eq. (4.38) and δ_n^{n+1} is the normal overlapping distance of the two colliding particles evaluated at the time $n + 1$:

$$\delta_n^{n+1} = \left\| (\mathbf{x}_p^n - \mathbf{x}_q^n) + (\mathbf{u}_p^n - \mathbf{u}_q^n) \Delta t \right\| - (R_p + R_q) \quad (4.53)$$

4.3.3 Particle-wall collisions

Particle-wall collisions are handled by introducing a virtual particle on the opposite side of the wall, effectively acting as a mirror image of the colliding particle. This approach follows the methodology proposed in [50]. Dynamically speaking the wall is considered as a particle with infinite radius. The center of mass \mathbf{x}_v of the virtual particle is conventionally positioned so that the contact plane of the two particles coincides with the wall. However, we have chosen to slightly shift the contact plane by a small distance ε_{wp} in order to prevent the Lagrangian marker, composing the moving mesh, to leave the simulation domain - which results in small particle deformation. In all simulations carried out, ε_{wp} was set equal to one quarter of the Eulerian grid cell.

4.4. Numerical implementation

	Two identical particles	Particle-wall
\mathbf{n}	$\frac{\mathbf{x}_p - \mathbf{x}_q}{\ \mathbf{x}_p - \mathbf{x}_q\ }$	$\frac{\mathbf{x}_p - \mathbf{x}_v}{\ \mathbf{x}_p - \mathbf{x}_v\ }$
m_{eff}	$m/2$	m_p
R_{eff}	$R/2$	R_p
St_{imp}	$\frac{1}{9} \frac{R\rho_s}{\mu_f} \Delta u(t_{imp})$	$\frac{2}{9} \frac{R_p\rho_s}{\mu_f} u_p(t_{imp})$
δ_n^{n+1}	$\left\ (\mathbf{x}_p^n - \mathbf{x}_q^n) + \Delta \mathbf{u}^n \Delta t \right\ - 2R$	$\left\ (\mathbf{x}_p^n - \mathbf{x}_v^n) + \mathbf{u}_p^n \Delta t \right\ - 2R_p$

Table 4.2: Numerical parameters for the collision model in the case of a collision between two identical particles, and a particle-wall collision.

Table 4.2 shows the numerical parameters of the model for both collisions between a particle and a wall and between two identical freely moving particles p and q , with the same radius $R_p = R_q = R$ and mass $m_p = m_q = m$. The relative velocity of the two particles is defined as $(\Delta \mathbf{u} = \mathbf{u}_p - \mathbf{u}_q)$.

4.4 Numerical implementation

The primary difficulty in solving the Navier-Stokes equations lies in the nonlinearity and the coupling between the pressure and velocity fields. The momentum equation includes both velocity and pressure, and is nonlinear due to the convective acceleration term. Meanwhile, the continuity equation involves only the velocity field, but it must be satisfied for the pressure field to be accurate. The pressure does not appear as a primary variable in either equation, yet it indirectly influences both through its role in the momentum equation. Casting the equations onto matrix form further emphasizes this points:

$$\begin{bmatrix} \mathbf{A} & \mathbf{G} \\ \mathbf{G}^T & 0 \end{bmatrix} \begin{bmatrix} \mathbf{u}^{n+1} \\ \mathbf{p}^{n+1} \end{bmatrix} = \begin{bmatrix} \boldsymbol{\Sigma} \\ 0 \end{bmatrix} \quad (4.54)$$

where \mathbf{A} , \mathbf{G} and \mathbf{G}^T , are the terms associated with the advection, gradient, and divergence operators respectively. $\boldsymbol{\Sigma}$ regroup the remaining terms (surface and body forces). This formulation highlight the saddle point nature of the problem, characterized by a zero diagonal block. It also underscores that without an explicit equation for pressure, it is impossible to directly solve for the pressure and velocity fields using standard iterative methods. Given the inherent complexities, it appears necessary to devise an algorithm that resolves these equations in the right sequence, making all the necessary information available when needed. In this work, we used a splitting operator approach based on the projection method of Chorin [21] and Yanenko [119]

4.4.1 The projection method

The projection method decomposes a complex problem into the sum of simpler sub-problems. This allows us to address each subproblem separately, applying a solution method tailored to each one. Consider the semi discretize form of the Naviers stokes euqations:

$$\frac{\mathbf{u}^{n+1} - \mathbf{u}^n}{\Delta t} = -\mathbf{A}^n - \frac{1}{\rho^{n+1}} \nabla p^{n+1} + \frac{1}{\rho^{n+1}} (\mathbf{D}^{n+1} + \mathbf{F}^{n+1}) + \mathbf{g} \quad (4.55)$$

where the convection term is represented by \mathbf{A}^n , the diffusion term by \mathbf{D}^{n+1} , the collisional source term by \mathbf{F}^{n+1} , and the gravitational source term by \mathbf{g} . We follow the procedure of [21, 119] to subdivide the equation into two subproblems:

Convection-Diffusion problem

$$\frac{\mathbf{u}^* - \mathbf{u}^n}{\Delta t} = -\mathbf{A}^n + \frac{1}{\rho^{n+1}} (\mathbf{D}^{n+1} + \mathbf{F}^{n+1}) + \mathbf{g} \quad (4.56)$$

The evaluation of the diffusion term is implicit in time and computed iteratively using an Uzawa algorithm. Due to the large viscosity ratio required by the viscous penalty method, an explicit evaluation would result in impractically small integration time steps.

Degenerate Stokes problem

$$\frac{\mathbf{u}^{n+1} - \mathbf{u}^*}{\Delta t} = -\frac{1}{\rho^{n+1}} \nabla p^{n+1} \quad (4.57a)$$

$$\nabla \cdot \mathbf{u}^{n+1} = 0 \quad (4.57b)$$

Taking the divergence of equation Eq. (4.57a) and combining it with Eq. (4.57b) results in the Poisson equation for pressure:

$$\nabla \cdot \left(\frac{\nabla p^{n+1}}{\rho^{n+1}} \right) = \frac{1}{\Delta t} \nabla \cdot \mathbf{u}^* \quad (4.58)$$

In the first stage of the projection method, we predict a temporary velocity field \mathbf{u}^* by solving the advection-diffusion subproblem without considering the pressure. In the next stage, we use the obtained velocity field to solve the Poisson equation for pressure. Finally, once the pressure field is known, the temporary velocity field is corrected by projecting it onto a divergence-free velocity field.

4.4.2 Solving the advection-diffusion problem

Spatial discretisation

To solve the advection-diffusion problem, we first discretize the governing equations - that is, we transform the continuous mathematical expressions into a form suitable for numerical computation. This process is done using the finite volume discretization (FVD) approach, which works by applying the conservation principles of mass and momentum over small control volumes. The fluid properties at the center of each control volume are approximated by their average value over the control volume. For instance, the average velocity is calculated as:

$$\mathbf{u} = \frac{1}{\Omega} \int_{\Omega} \mathbf{u}(x) dV \quad (4.59)$$

Ω denotes the control volume associated with the variable. In a 2D scenario, $\Omega = \Delta x \Delta y$ is effectively a surface area, yet we consider it as a volume. While we assume a two-dimensional flow for clarity, the extension to three dimensions is straightforward.

The computational domain is subdivided using a structured staggered grid, similar to the one introduced by Harlow and Welch [58] for the MAC method. Typically, control volumes assigned to the velocities are centered over the boundaries of the pressure control volume as shown in Fig. 4.6. This arrangement is inspired by the nature of the conservation equations, which require a balance between the rate of change in the volume and the net outflow through the boundaries. This setup offers greater accuracy compared to a collocated grid, particularly for pressure gradients, by computing differences between adjacent points. Moreover, it ensures a tighter coupling between the variables than if they were all located at the same grid node. The continuity equation on a staggered grid links every other grid point, which can lead to exactly satisfying continuity even for highly fluctuating velocities [110]. The control volumes associated with pressure p , the x -component of velocity u , and the y -component of velocity v , are denoted by Ω , Ω_u , and Ω_v respectively. Each control volume has bounding surfaces labeled as \mathcal{E} , \mathcal{W} , \mathcal{N} , and \mathcal{S} for the east, west, north, and south boundaries, respectively. Their normal vectors are denoted as:

$$\mathbf{n}_{\mathcal{E}} = \begin{pmatrix} 1 \\ 0 \end{pmatrix}, \quad \mathbf{n}_{\mathcal{W}} = \begin{pmatrix} -1 \\ 0 \end{pmatrix}, \quad \mathbf{n}_{\mathcal{N}} = \begin{pmatrix} 0 \\ 1 \end{pmatrix}, \quad \mathbf{n}_{\mathcal{S}} = \begin{pmatrix} 0 \\ -1 \end{pmatrix}$$

When discretizing the continuity equation over Ω , we apply Gauss's theorem to convert the volume integral into a surface integral over the boundary of the control volume $\partial\Omega$, with the integrals evaluated numerically as:

$$\begin{aligned} \frac{1}{\Omega} \int_{\Omega} \nabla \cdot \mathbf{u} dV &= \frac{1}{\Omega} \oint_{\partial\Omega} \mathbf{u} \cdot \mathbf{n} dS = 0 \\ &= \frac{1}{\Delta x \Delta y} \{ [(u)_{\mathcal{E}} - (u)_{\mathcal{W}}] \Delta y + [(v)_{\mathcal{N}} - (v)_{\mathcal{S}}] \Delta x \} \end{aligned} \quad (4.60)$$

4.4. Numerical implementation

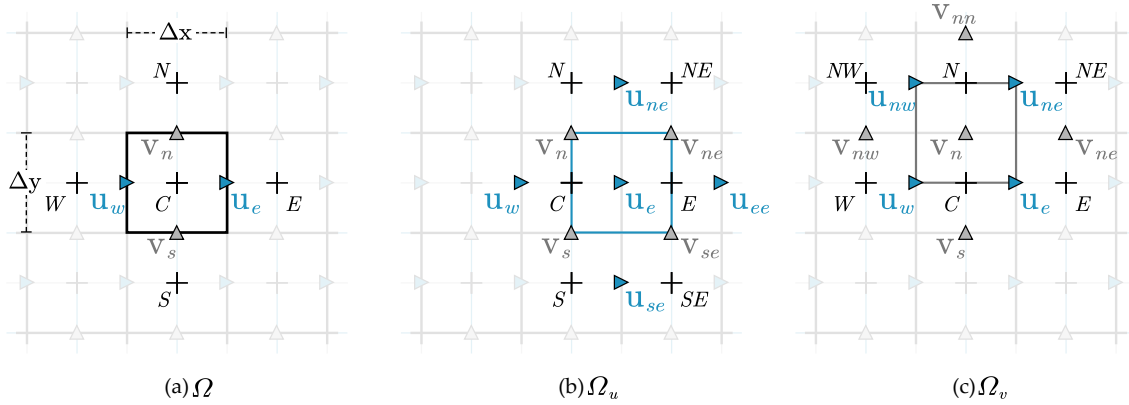


Figure 4.6: (a) Control volume for the pressure calculation. (b) Control volume for the x-direction velocity calculation. (c) Control volume for the y-direction velocity calculation.

By expressing the velocities according to the notation shown in Fig. 4.6a, we derive the discretized equation:

$$\frac{u_e - u_w}{\Delta x} + \frac{v_n - v_s}{\Delta y} = 0 \quad (4.61)$$

The advection and diffusion terms are computed with a similar procedure.

Discretization of the advection term

The computation of the average value of the advection terms is achieved by recasting the volume integral as a net flux across the boundaries of the velocity control volume:

$$\mathbf{A} = \frac{1}{\Omega_{u,v}} \int_{\Omega_{u,v}} \nabla \cdot (\mathbf{u}\mathbf{u}) dV = \frac{1}{V} \oint_{\partial\Omega_{u,v}} \mathbf{u}(\mathbf{u} \cdot \mathbf{n}) dS \quad (4.62)$$

Even though velocities are centered within their individual control volumes, momentum fluxes are calculated at the control volumes' boundaries. To evaluate the flux, a second-order centered scheme is employed, which involves the linear interpolation of velocities at the boundary locations associated with Ω_u and Ω_v . The x -component of the advection term is derived by approximating the flux across the boundaries of Ω_u :

$$(\mathbf{A}_x)_{\Omega_u} = \frac{1}{\Delta x \Delta y} \{ [(uu)_E - (uu)_W] \Delta y + [(uv)_N - (uv)_S] \Delta x \}$$

Using the discretized velocities, the flux approximation becomes:

$$\begin{aligned} (\mathbf{A}_x)_{\Omega_u} = & \frac{1}{\Delta x} \left[\left(\frac{u_{ee} + u_e}{2} \right)^2 - \left(\frac{u_e + u_w}{2} \right)^2 \right] \\ & + \frac{1}{\Delta y} \left[\left(\frac{u_{ne} + u_e}{2} \right) \left(\frac{v_{ne} + v_n}{2} \right) - \left(\frac{u_e + u_{se}}{2} \right) \left(\frac{v_{se} + v_s}{2} \right) \right] \end{aligned} \quad (4.63)$$

4.4. Numerical implementation

Likewise, the y -component of the advection term is computed by evaluating the flux across the boundaries of Ω_v :

$$(A_y)_{\Omega_v} = \frac{1}{\Delta x \Delta y} \{ [(uv)_{\mathcal{E}} - (uv)_{\mathcal{W}}] \Delta y + [(vv)_{\mathcal{N}} - (vv)_{\mathcal{S}}] \Delta x \}$$

And the flux approximation with discretized velocities is given by:

$$(A_y)_{\Omega_v} = \frac{1}{\Delta x} \left[\left(\frac{\mathbf{u}_{ne} + \mathbf{u}_e}{2} \right) \left(\frac{\mathbf{v}_{ne} + \mathbf{v}_n}{2} \right) - \left(\frac{\mathbf{u}_{nw} + \mathbf{u}_w}{2} \right) \left(\frac{\mathbf{v}_n + \mathbf{v}_{nw}}{2} \right) \right] + \frac{1}{\Delta y} \left[\left(\frac{\mathbf{v}_{nn} + \mathbf{v}_n}{2} \right)^2 - \left(\frac{\mathbf{v}_n + \mathbf{v}_s}{2} \right)^2 \right] \quad (4.64)$$

Discretization of the diffusion term

The average value of diffusion terms is computed by reinterpreting it as a net flux over the boundaries of the velocity control volume:

$$\mathbf{D} = \frac{1}{\Omega_{u,v}} \int_{\Omega_{u,v}} \nabla \cdot \mu (\nabla \mathbf{u} + \nabla^T \mathbf{u}) dV = \frac{1}{V} \oint_{\partial \Omega_{u,v}} \mu (\nabla \mathbf{u} + \nabla^T \mathbf{u}) \cdot \mathbf{n} dS \quad (4.65)$$

The x -component of the diffusion term is determined by assessing the flux at the boundaries of Ω_u :

$$(D_x)_{\Omega_u} = \frac{1}{\Delta x \Delta y} \left\{ \left[2 \left(\mu \frac{\partial u}{\partial x} \right)_{\mathcal{E}} - 2 \left(\mu \frac{\partial u}{\partial x} \right)_{\mathcal{W}} \right] \Delta y + \left[\mu \left(\frac{\partial u}{\partial y} + \frac{\partial v}{\partial x} \right)_{\mathcal{N}} - \mu \left(\frac{\partial u}{\partial y} + \frac{\partial v}{\partial x} \right)_{\mathcal{S}} \right] \Delta x \right\}$$

The velocity derivatives appearing in the viscous stress tensor are evaluated using the second-order centered differences scheme. Using discrete velocities, we obtain:

$$(D_x)_{\Omega_u} = \frac{1}{\Delta x} \left[2\mu_E \left(\frac{\mathbf{u}_{ee} - \mathbf{u}_e}{\Delta x} \right) - 2\mu_C \left(\frac{\mathbf{u}_e - \mathbf{u}_w}{\Delta x} \right) \right] + \frac{1}{\Delta y} \left[\mu_N \left(\frac{\mathbf{u}_{ne} - \mathbf{u}_e}{\Delta y} + \frac{\mathbf{v}_{ne} - \mathbf{v}_n}{\Delta x} \right) - \mu_S \left(\frac{\mathbf{u}_e - \mathbf{u}_{se}}{\Delta y} + \frac{\mathbf{v}_{se} - \mathbf{v}_s}{\Delta x} \right) \right] \quad (4.66)$$

At the north and south boundaries of $\partial \Omega_u$, where viscosities are not defined, we approximate them by taking the mean of the four nearest neighbors:

$$\mu_N = \frac{1}{4} (\mu_{NE} + \mu_N + \mu_C + \mu_E), \quad \mu_S = \frac{1}{4} (\mu_E + \mu_C + \mu_S + \mu_{SE}).$$

Similarly, the y -component of the diffusion term is determined by assessing the flux at the boundaries of Ω_v :

$$(D_y)_{\Omega_v} = \frac{1}{\Delta x \Delta y} \left\{ \left[\left(\mu \frac{\partial v}{\partial x} + \mu \frac{\partial u}{\partial y} \right)_{\mathcal{E}} - \left(\mu \frac{\partial v}{\partial x} + \mu \frac{\partial u}{\partial y} \right)_{\mathcal{W}} \right] \Delta y + \left[2 \left(\mu \frac{\partial v}{\partial y} \right)_{\mathcal{N}} - 2 \left(\mu \frac{\partial v}{\partial y} \right)_{\mathcal{S}} \right] \Delta x \right\}$$

4.4. Numerical implementation

Utilizing the discretized velocities, the flux estimation becomes:

$$\begin{aligned} (D_y)_{\Omega_v} = & \frac{1}{\Delta x} \left[\mu_{\mathcal{E}} \left(\frac{v_{ne} - v_n}{\Delta x} + \frac{u_{ne} - u_e}{\Delta y} \right) - \mu_{\mathcal{W}} \left(\frac{v_n - v_{nw}}{\Delta x} + \frac{u_{nw} - u_w}{\Delta y} \right) \right] \\ & + \frac{1}{\Delta y} \left[2\mu_N \left(\frac{v_{nn} - v_n}{\Delta y} \right) - 2\mu_C \left(\frac{v_n - v_s}{\Delta y} \right) \right] \end{aligned} \quad (4.67)$$

For the undefined viscosities at the east and west boundaries of $\partial\Omega_v$, we calculate:

$$\mu_{\mathcal{E}} = \frac{1}{4} (\mu_{NE} + \mu_N + \mu_C + \mu_E), \quad \mu_{\mathcal{W}} = \frac{1}{4} (\mu_N + \mu_{NW} + \mu_W + \mu_C).$$

Prediction step

With the advection and diffusion terms available, Eq. (4.56) can be used to compute the temporary velocity field \mathbf{u}^* .

$$\mathbf{u}_e^* = \mathbf{u}_e^n + \Delta t \left\{ -(\mathbf{A}_x)_{\Omega_u}^n + \frac{1}{\rho_u^{n+1}} (\mathbf{D}_x)_{\Omega_u}^{n+1} + (\mathbf{F}_x)_{\Omega_u}^{n+1} + (\mathbf{g}_x)_{\Omega_u} \right\} \quad (4.68a)$$

$$\mathbf{v}_n^* = \mathbf{v}_n^n + \Delta t \left\{ -(\mathbf{A}_y)_{\Omega_v}^n + \frac{1}{\rho_v^{n+1}} (\mathbf{D}_y)_{\Omega_v}^{n+1} + (\mathbf{F}_y)_{\Omega_v}^{n+1} + (\mathbf{g}_x)_{\Omega_v} \right\} \quad (4.68b)$$

The densities at the centers of the control volumes Ω_u , and Ω_v are respectively:

$$\rho_u = \frac{1}{2} (\rho_E + \rho_C), \quad \rho_v = \frac{1}{2} (\rho_N + \rho_C).$$

4.4.3 Solving the degenerate Stokes problem

The velocity field \mathbf{u}^* obtained from the prediction step isn't divergence-free, so it's corrected using the pressure field in the following step. The equation for pressure is obtained by discretizing the Poisson equation Eq. (4.58).

Discretization of the pressure equation

The average value of the left-hand side terms in Eq. (4.58) is calculated by reinterpreting it as a net flux over the boundaries of the pressure control volume Ω :

$$(LHS)_{\Omega} = \frac{1}{\Omega} \int_{\Omega} \nabla \cdot \left(\frac{1}{\rho} \nabla p \right) dV = \frac{1}{V} \oint_{\partial\Omega} \left(\frac{1}{\rho} \nabla p \right) \cdot \mathbf{n} dS \quad (4.69)$$

4.4. Numerical implementation

Evaluating the flux at the boundaries of Ω and approximating the pressure differential using a centered difference yields:

$$\begin{aligned} (\text{LHS})_{\Omega} &= \frac{1}{\Delta x \Delta y} \left\{ \left[\left(\frac{1}{\rho} \frac{\partial p}{\partial x} \right)_{\varepsilon} - \left(\frac{1}{\rho} \frac{\partial p}{\partial x} \right)_{\omega} \right] \Delta y + \left[\left(\frac{1}{\rho} \frac{\partial p}{\partial y} \right)_{\mathcal{N}} - \left(\frac{1}{\rho} \frac{\partial p}{\partial y} \right)_{\mathcal{S}} \right] \Delta x \right\} \\ &= \left[\frac{1}{\rho_{\varepsilon}} \frac{p_E - p_C}{\Delta x} - \frac{1}{\rho_{\omega}} \frac{p_C - p_W}{\Delta x} \right] + \left[\frac{1}{\rho_{\mathcal{N}}} \frac{p_N - p_C}{\Delta y} - \frac{1}{\rho_{\mathcal{S}}} \frac{p_C - p_S}{\Delta y} \right] \end{aligned} \quad (4.70)$$

Since the pressures aren't available at the boundaries of Ω , we evaluate them using linear interpolations:

$$\rho_{\varepsilon} = \frac{1}{2} (\rho_E + \rho_C), \quad \rho_{\omega} = \frac{1}{2} (\rho_C + \rho_W), \quad \rho_{\mathcal{N}} = \frac{1}{2} (\rho_N + \rho_C), \quad \rho_{\mathcal{S}} = \frac{1}{2} (\rho_C + \rho_S).$$

Discretizing the right-hand side of the Poisson equation (4.58) results in:

$$(\text{RHS})_{\Omega} = \frac{1}{\Delta t} \left(\frac{u_e^* - u_w^*}{\Delta x} + \frac{v_n^* - v_s^*}{\Delta y} \right) \quad (4.71)$$

Equating the derived expressions gives the fully discretized equation for the pressure:

$$\frac{2}{\Delta x^2} \left(\frac{p_E - p_C}{\rho_E + \rho_C} - \frac{p_C - p_W}{\rho_C + \rho_W} \right) + \frac{2}{\Delta y^2} \left(\frac{p_N - p_C}{\rho_N + \rho_C} - \frac{p_C - p_S}{\rho_C + \rho_S} \right) = \frac{1}{\Delta t} \left(\frac{u_e^* - u_w^*}{\Delta x} + \frac{v_n^* - v_s^*}{\Delta y} \right) \quad (4.72)$$

Solving Eq. (4.72) tends to be the most time-consuming step in any CFD simulation. In this work, an efficient SSOR-preconditioned GCP solver is employed to solve the elliptic equation.

Projection step

With the pressure field known, the temporary velocity field \mathbf{u}^* can be corrected by projecting it onto a divergence-free velocity field using:

$$u_e^{n+1} = u_e^* - \frac{\Delta t}{\Delta x} \frac{p_E^{n+1} - p_C^{n+1}}{\rho_e^{n+1}} \quad (4.73a)$$

$$v_n^{n+1} = v_n^* - \frac{\Delta t}{\Delta y} \frac{p_N^{n+1} - p_C^{n+1}}{\rho_n^{n+1}} \quad (4.73b)$$

The semi-explicit projection method presented in this section is first-order in time. Furthermore, the integration time step needs to satisfy:

$$\Delta t_{conv} = \frac{CFL}{\frac{\max(|u|)}{\Delta x} + \frac{\max(|v|)}{\Delta y} + \frac{\max(|w|)}{\Delta z}} \quad (4.74)$$

4.5 Complete Algorithm

1. Initialize the front position, the solid phase indicator function I , fluid velocity \mathbf{u} , density ρ , and viscosity μ .
2. Loop over time:

(a) Prediction step:

- i. Compute the Collision force:

$$\mathbf{F}_c^{n+1} = -k_i^n \delta_n^{n+1} \mathbf{n}$$

- ii. Compute the Advection term \mathbf{A}^n using Eqs. (4.63) and (4.64).
- iii. Compute the implicit Diffusion term \mathbf{D}^{n+1} using Eqs. (4.66) and (4.67).
- iv. Compute the intermediate velocity field:

$$\frac{\mathbf{u}^* - \mathbf{u}^n}{\Delta t} = -\mathbf{A}^n + \frac{1}{\rho^{n+1}} (\mathbf{D}^{n+1} + \mathbf{F}^{n+1}) + \mathbf{g}$$

(b) Projection step:

- i. Compute the pressure field:

$$\nabla \cdot \left(\frac{\nabla \mathbf{p}^{n+1}}{\rho^{n+1}} \right) = \frac{1}{\Delta t} \nabla \cdot \mathbf{u}^*$$

- ii. Apply velocity correction:

$$\frac{\mathbf{u}^{n+1} - \mathbf{u}^*}{\Delta t} = -\frac{1}{\rho^{n+1}} \nabla \mathbf{p}^{n+1}$$

(c) Interface transport:

- i. Interpolate the velocity field at the Lagrangian nodes i :

$$\hat{\mathbf{u}}_i^{n+1} = \mathcal{I}(\hat{\mathbf{x}}_i^n, \mathbf{u}^{n+1})$$

- ii. Compute the mean velocity of the Lagrangian elements j :

$$\hat{\mathbf{u}}_j^{n+1} = \frac{1}{3} \sum_{i=1}^3 \hat{\mathbf{u}}_i^{n+1}$$

- iii. Compute the mean velocity of the front:

$$\mathbf{u}_m^{n+1} = \frac{\sum S_j \hat{\mathbf{u}}_j^{n+1}}{\sum S_j}$$

- iv. Translate the Lagrangian nodes with the mean velocity:

$$\hat{\mathbf{x}}_i^{n+1} = \hat{\mathbf{x}}_i^n + \Delta t \mathbf{u}_m^{n+1}$$

- v. Reconstruct the phase indicator function:

$$I^{n+1} = \mathcal{R}(\hat{\mathbf{x}}^{n+1})$$

(d) Update the "one-fluid" fields:

$$\phi^{n+1} = \mathcal{F}(\phi_s, \phi_f, I^{n+1})$$

5

NUMERICAL SIMULATIONS RESULTS

In this chapter, the validity of the present numerical method will be thoroughly evaluated by comparing its performance against the experimental data of two well-established test cases in the field, namely the sedimentation of a spherical particle in a fluid at rest made by Cate et al. 2002 [18] and the normal collision of a spherical particle with a wall made by Gondret et al. 2002 [53]. The High Performance Computing capabilities of our approach are finally tested by reproducing the liquid-solid fluidized bed of [1] - involving ~ 2100 particles. The results presented in this chapter form the core of an article published in the *International Journal of Multiphase Flow*: [57].

5.1 Hydrodynamic validation: Sedimentation of a solid particle in a finite size domain

In the first validation case, we consider the settling of a spherical particle in a three-dimensional box at different Reynolds numbers. This test case is based on the experimental configuration of Cate et al. [18], where a single sphere with a diameter of $d_p = 15$ mm is released at rest in an open quiescent container. This numerical benchmark has also been performed by Vincent et al. [115], Zhou et al. [130], and Chen and Müller [19] among others.

The Reynolds numbers, $Re_t = \rho_f V_t R_p / \mu_f$ based on the terminal velocity V_t considered in this study are 1.5, 4.1, 11.6, and 32.2. These are achieved by adjusting the fluid type inside the box, as shown in Table 5.1. The container dimensions are $0.10 \text{ m} \times 0.16 \text{ m} \times 0.10 \text{ m}$ in the x , y , and z -directions, respectively. The gravity $g = 9.81 \text{ m} \cdot \text{s}^{-1}$ acts in the negative y -direction. The release position of the particle's gravity center is positioned 12.75 cm above the bottom of the tank, and is centered on the x and z directions. The density of the solid particle is $\rho_p = 1120 \text{ kg/m}^3$.

Case	Re	R_ρ	ρ_f [$\text{kg} \cdot \text{m}^{-3}$]	μ_f [$\text{Pa} \cdot \text{s}$]	U_t [$\text{m} \cdot \text{s}^{-1}$]
1.1	1.5	1.115	970	0.373	0.038
1.2	4.1	1.161	965	0.212	0.060
1.3	11.6	1.164	962	0.113	0.091
1.4	31.9	1.167	960	0.058	0.128

Table 5.1: Physical parameters for a spherical particle settling in viscous fluid

Our numerical domain corresponds to the experimental container size. No-slip boundary conditions are imposed on the walls of the domain, while outflow boundary conditions (with a null reference pressure) are applied on the upper boundary. Initially, the fluid is at rest in the domain. The viscosity ratio is set to $R_\mu = 1000$ for all four cases. Finally, an integration time step equal to $\Delta t = 10^{-4} \text{ s}$ is used for the pressure solver.

Fig. 5.1 depicts the time evolution of the normalized vertical position and velocity of the particle at $Re = 31.9$. Results are presented for two mesh resolutions, $R_\Delta = 15$ and 30 cells per diameter, using both arithmetic and harmonic viscosity averaging at interface-crossing cells. The harmonic method proves more accurate, with the arithmetic approach overestimating drag and thus underestimating settling velocity. While refining the mesh improves the arithmetic method's accuracy, it cannot match the correct settling velocity even at $R_\Delta = 30$. Conversely, the harmonic method achieves great accuracy at $R_\Delta = 15$. Further refinement to $R_\Delta = 30$ offers negligible accuracy gains, suggesting

5.1. Hydrodynamic validation: Sedimentation of a solid particle in a finite size domain

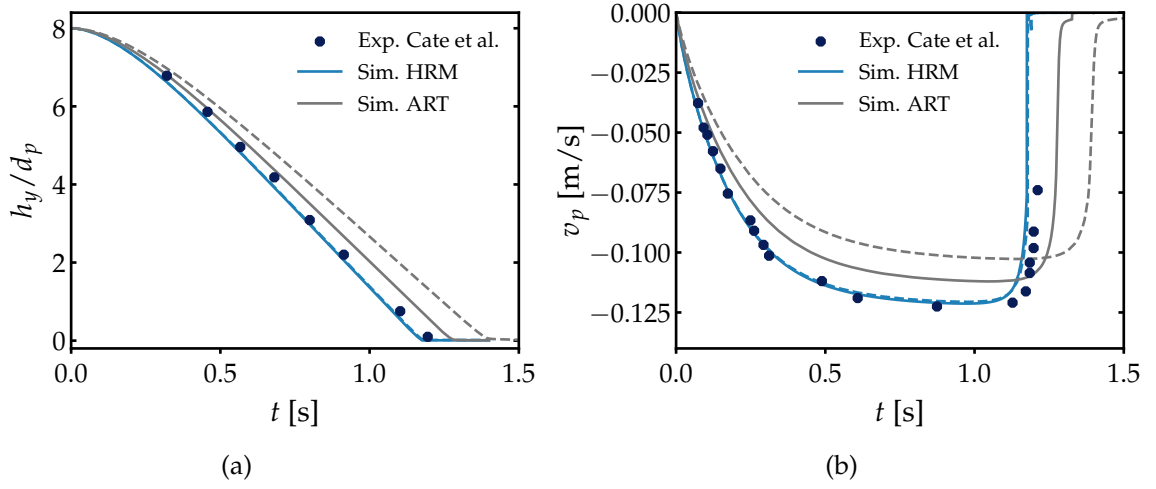


Figure 5.1: Time evolution of the simulated (a) vertical position and (b) vertical velocity for the case 1.4, $Re = 31.9$ as a function of mesh resolution and mixed cells viscosity modeling. Dashed line: resolution of 15 grid cells per diameter; continuous line: resolution of 30 grid cells per diameter. Blue line: harmonic averaging; gray line: arithmetic averaging. Vertical position normalized with the particle diameter.

convergence.

In subsequent simulations, the harmonic average and a grid resolution of $R_\Delta = 15$ were employed for all four Reynolds numbers listed in Table 5.1. The outcomes of these simulations are compared with the experimental results from ten Cate et al. in Figs. 5.2 and 5.3. As seen from the comparison, the dynamics of a settling particle at Reynolds numbers up to 31.9 are faithfully captured by our simulations. In conclusion, by reproducing this test case, we demonstrate that our method is able to accurately simulate the hydrodynamics of a solid sphere settling in a viscous fluid and the collision model for the no-bouncing contact regime. The subsequent section will be dedicated to further validating the collision model, specifically within the context of the bouncing regime.

5.1. Hydrodynamic validation: Sedimentation of a solid particle in a finite size domain

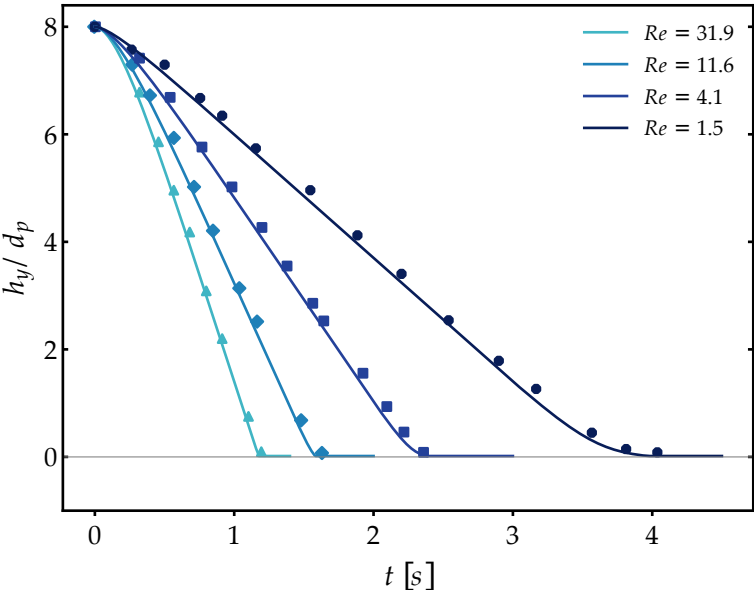


Figure 5.2: Time histories of the normalized gap height h_y/d_p for a particle settling in a small container. Symbols: experimental data of Cate et al. [18], lines: present simulations

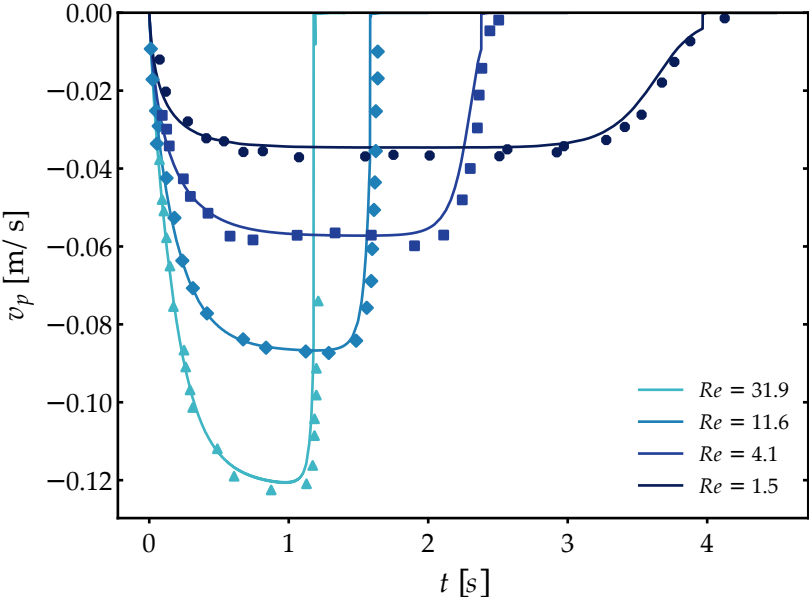


Figure 5.3: Time histories of the Settling Velocity v_p for a particle settling in a small container. Symbols: experimental data of Cate et al. [18], lines: present simulations

5.2 Collisional response validation: Normal collision of a particle with a planar wall

The simulation of the bouncing motion of a solid sphere colliding onto a planar surface in a viscous fluid is a challenging task, as it involves capturing the complex dynamics of the particle's motion, including its acceleration, multiple collisions, and deceleration. To validate our method, we reproduce the experimental data of Gondret, Lance, and Petit [53]. The setup of the simulation involves a stainless steel particle that is released into a tank filled with silicon oil RV10. Under the effect of gravity, the particle accelerates towards the bottom of the tank, colliding multiple times. We simulated the time evolution of the trajectory and vertical velocity profiles and compared them to the experimental data.

In the conducted experiment, the properties of the fluid and particles, as well as the particle's release position are carefully selected to ensure the particle reaches its terminal velocity of approximately $0.6 \text{ m} \cdot \text{s}^{-1}$ upon contacting the bottom wall. Simulating the entire acceleration distance can be computationally expensive.

Furthermore, accurately capturing the sequential bouncing motion of the particle is challenging. Errors from initial rebounds can compound, leading to significant discrepancies in subsequent bounces. Hence, establishing accurate starting conditions is of paramount importance. To address these challenges we reduced the simulation domain by releasing the particle from a height that corresponds to the maximum elevation it would reach after its first collision with the bottom wall in the experimental setup. This approach is justified by the observation that fluid perturbations caused by the initial rebound have negligible effects on subsequent bounces, as indicated in [53]. As a result, the Stokes numbers for the ensuing rebounds are $St = 75, 41, 20,$ and 5 . The simulation is conducted in a $9 \text{ mm} \times 12 \text{ mm} \times 9 \text{ mm}$ domain with a mesh resolution of $R_\Delta = 16$. The particle diameter is $d_p = 3 \text{ mm}$ and the center of the particle is positioned at the coordinates $(4.5 \text{ mm}, 8.88 \text{ mm}, 4.5 \text{ mm})$. The densities of the fluid and the solid are equal to 935 kg/m^3 and 7800 kg/m^3 respectively. The fluid viscosity is equal to $0.01 \text{ Pa} \cdot \text{s}$ and the viscosity ratio is kept at $R_\mu = 1000$. No-slip boundary conditions are imposed on all the walls of the domain, and the time step is set to $\Delta t = 5 \times 10^{-5} \text{ s}$.

Figures 5.4 and 5.5 display the time-dependent behavior of the particle's normalized distance to the wall and its settling velocity. The simulations use both harmonic average and step function approaches for calculating viscosity at interface-crossing cells, as detailed in the previous chapter (Eqs. (4.34) and (4.35)). Both methods show strong alignment with experimental data during the initial settling phase, providing an accurate representation of the particle's path. However, post-rebound inconsistencies become apparent. Specifically, after the particle's first interaction with its wake, the drag force is overestimated, resulting in reduced rebound heights. Using the step function method for viscosity calculation improves the simulation results. While doing so, we numerically

5.2. Collisional response validation: Normal collision of a particle with a planar wall

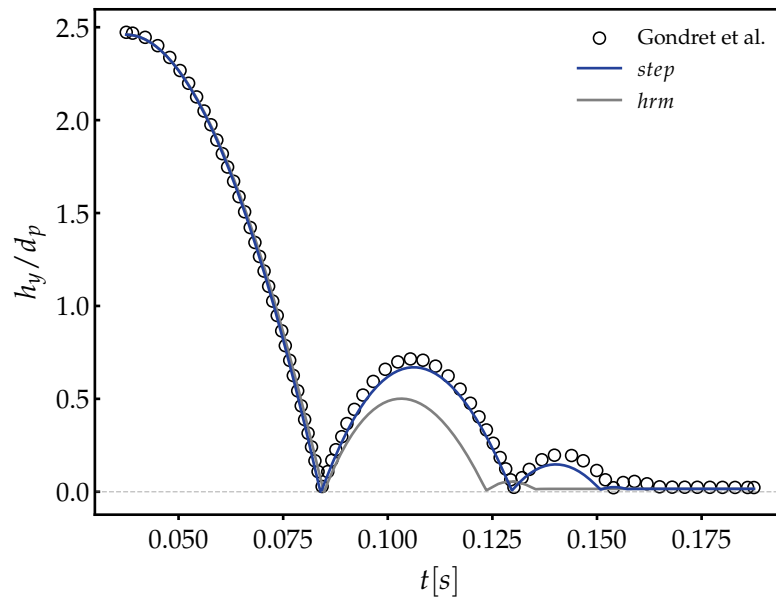


Figure 5.4: Time histories of the normalized gap height h_y/d_p . Symbols: experimental data of Gondret, Lance, and Petit [53], lines: present simulations

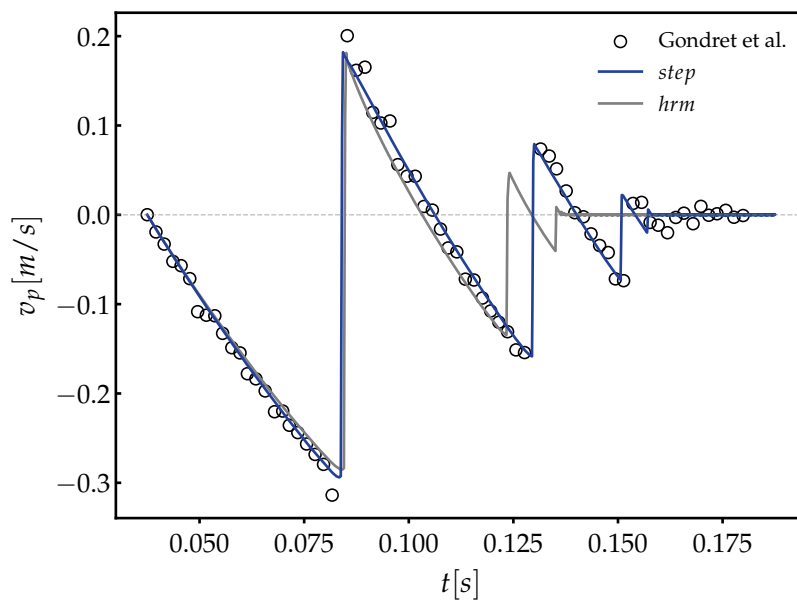


Figure 5.5: Time histories of the y-component of the particle velocity v_p . Symbols: experimental data of Gondret, Lance, and Petit [53], lines: present simulations

5.2. Collisional response validation: Normal collision of a particle with a planar wall

decrease the particle's hydrodynamic diameter, thereby lowering the drag.

As the simulation progresses and the particle rebounds multiple times, minor deviations between the simulated and experimental data emerge. These deviations cause the simulated particle to settle earlier than its real-world counterpart. The discrepancies can be linked to cumulative errors in the rebound simulations and variability in the experimental data used for the collision model, particularly noticeable at lower Stokes numbers (Fig. 3.1). Optimizing the collision model for specific materials could enhance accuracy but would limit its broader applicability, which is not ideal. Therefore, we consider the current results to be adequate for our purposes. This validation strengthens our confidence in the collision model, particularly for binary collisions. In the subsequent section, we will assess the model's performance in simulating complex flows involving multiple interacting particles.

5.3 Particle resolved direct numerical simulation of a 2100 liquid–solid fluidized bed

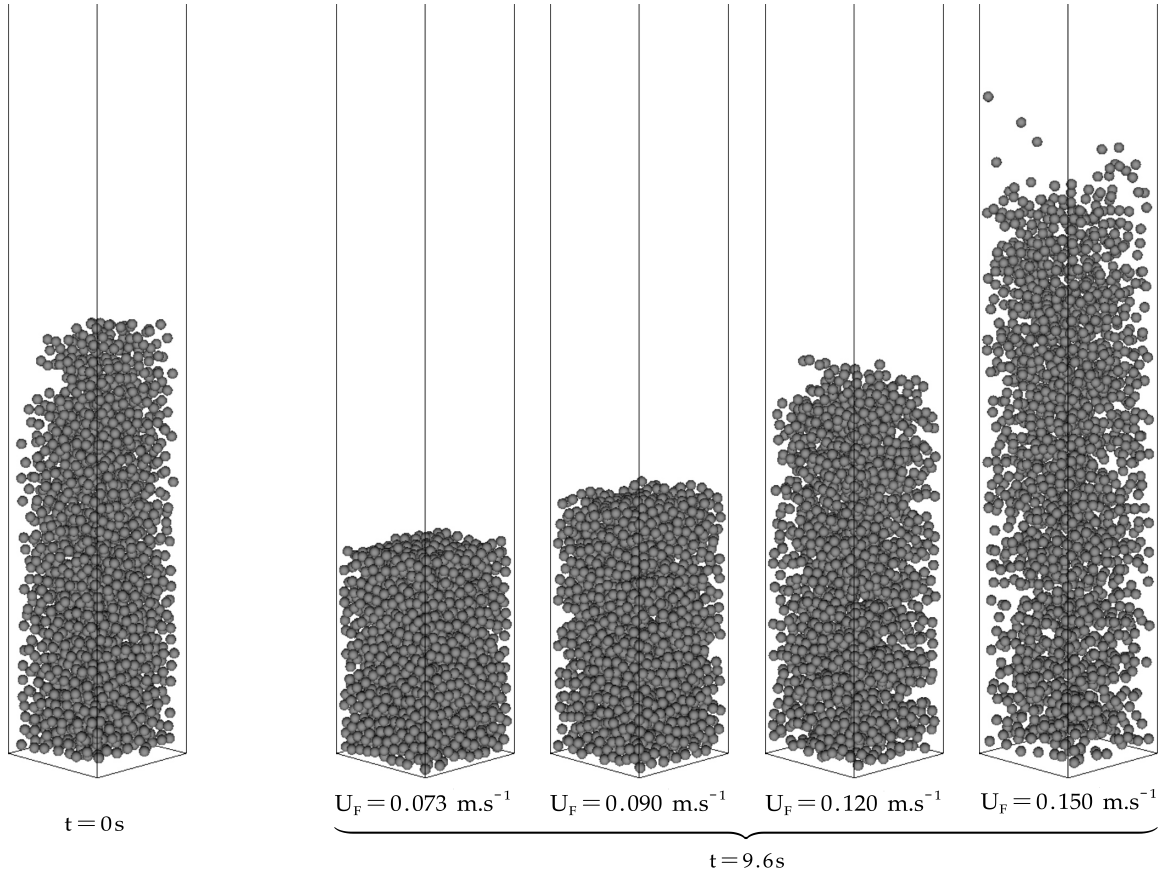


Figure 5.6: 3D views of the particles' position distribution in the domain at $t = 0$ s and 9.6 s for the four fluidization velocities tested.

In this section, we aim to evaluate the accuracy of our framework in reproducing the global behavior of a liquid–solid fluidized bed. To do so, we present simulation results of a 2100-particle system at four different fluidization velocities. The parameters for the simulation are based on the experiment of Aguilar-Corona [1], who studied the fluidization of 6 mm monodisperse spherical Pyrex particles ($\rho_p = 2230 \text{ kg/m}^3$) in a concentrated aqueous solution of potassium thiocyanate ($\rho_f = 1400 \text{ kg/m}^3$, $\mu_f = 3.8 \times 10^{-3} \text{ Pas}$). The particle terminal velocity is $V_t = 0.24 \text{ m/s}$.

The experimental setup was specifically designed with numerical method validation in mind, as the refractive index of both phases was chosen to allow for non-intrusive optical measurement techniques. These techniques are used to characterize the fluid velocity field and particle agitation. This configuration was already studied numerically by Ozel et al. [86], using the Implicit Tensorial Penalty Method of Vincent et al. [115], with a mesh resolution of $R_\Delta = 12$. The Reynolds number based on the terminal velocity is $Re_t = 530$ and the associated Stokes number is $St_t = 94$. However, in [86], the authors reported a value of $St_t = 5.3$ based on the Reynolds number in the creeping flow regime.

5.3. Particle resolved direct numerical simulation of a 2100 liquid–solid fluidized bed

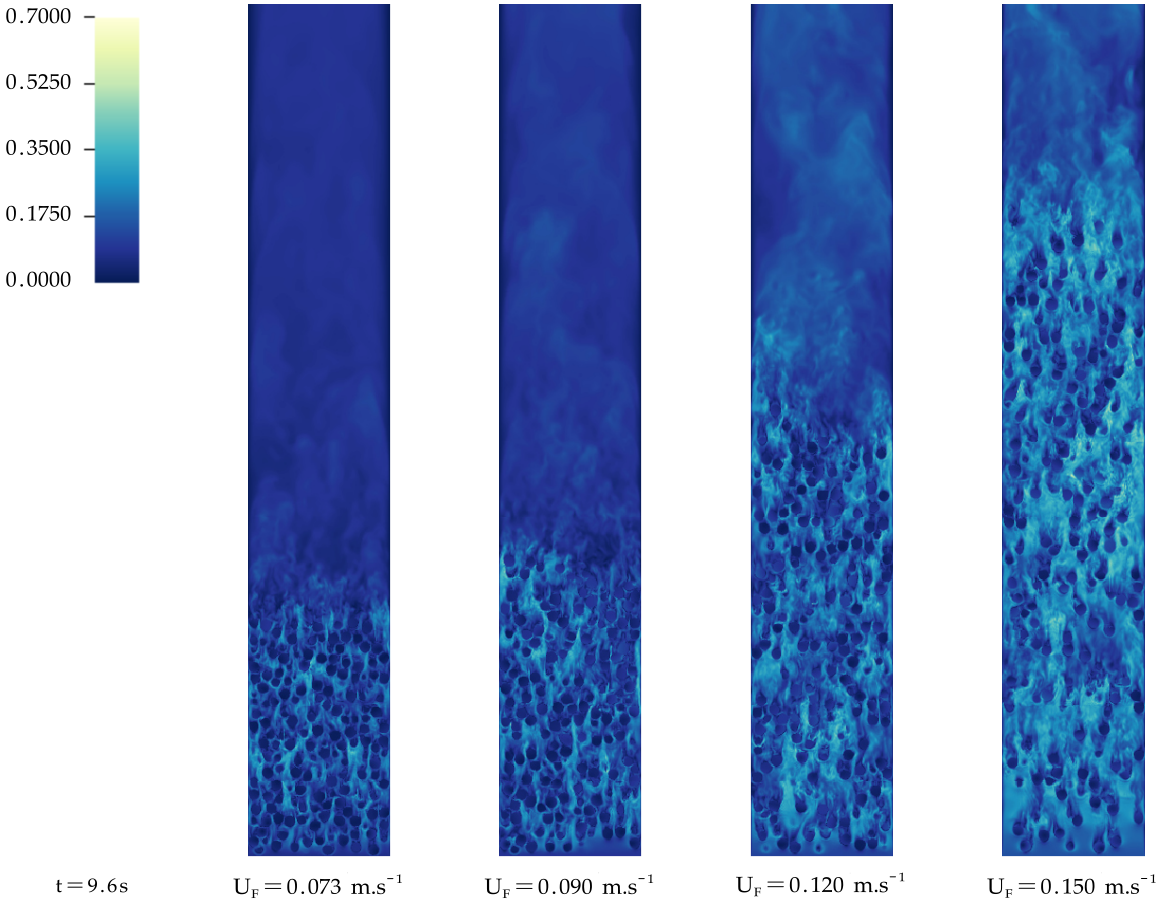
We aim to evaluate the performance of our approach by reproducing the numerical configuration of Ozel for four different fluidization velocities: $U_F = 0.15$ m/s, 0.12 m/s, 0.09 m/s, 0.073 m/s. However, as our code does not utilize O-grid mesh, we have adapted the initial container geometry from a cylinder to a cuboid of dimensions 0.072 m \times 0.648 m \times 0.072 m, which matches the experimental cross-section area. To maintain consistency with the original study, we have also imposed a mesh resolution of $R_\Delta = 12$, which is slightly coarser than the resolution used in previous cases but is considered a fair balance between computational cost and accuracy.

Additionally, we have set the viscosity ratio to $R_\mu = 1 \times 10^4$. To expedite the initial transient phase, we initially positioned the particles to closely correspond with the bed height obtained in case number 3 of [86] (where $U_F = 0.12$ m/s and the bed height is attained in the stationary regime). The initial bed was generated using the Bridson algorithm [14]. Fig. 5.6 illustrates the initial bed as well as its state near the end of the simulation for the four cases.

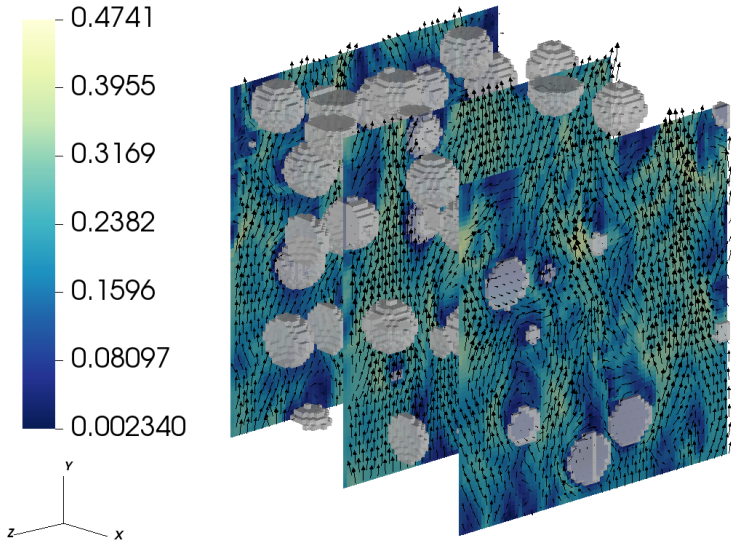
Fig. 5.7 provides both a macroscopic and microscopic view of fluidized bed dynamics. The top figure illustrates the velocity magnitude at the domain’s central plane at $t = 9.6$ seconds, spanning various fluidization velocities U_F . Notably, velocities within particles are significantly lower than in the surrounding fluid. As U_F increases, we observe the emergence of larger pseudo-turbulent structures forming in the wake of particles.

Focusing on the microscopic level, the vector plot in the bottom figure reveals the formation of dynamic boundary layers around each particle. Fluid velocity changes from the velocity of the particle at its surface to values exceeding the fluidization velocity further away. The non-uniform particle distribution is also evident, leading to velocity disparities between particle-dense and particle-sparse regions. As particles move through the fluid, their boundary layers disturb the flow, creating low-velocity wake zones right behind them. The interaction and superposition of these wakes from multiple particles add a layer of complexity to the flow dynamics. A more detailed, quantitative analysis of these complex flow patterns will be elaborated in the following sections.

5.3. Particle resolved direct numerical simulation of a 2100 liquid–solid fluidized bed



(a) Color map of the velocity magnitude, in a plane centered in the domain of the x-direction, during the established regime ($t = 9.6\text{ s}$) and for the four fluidization velocities U_F . Fluidization velocity is in positive y-direction, gravity is in negative y-direction



(b) Vector plot of the velocity magnitude, in the bottom central region of the case $U_F = 0.120\text{ m/s}$

Figure 5.7: Fluid flow structure visualization.

5.3.1 Solid Phase Statistics

The particle average of any particle-related quantity $\phi_p(p, t)$ is computed using the particle ensemble averaging operator defined as follows:

$$\langle \phi_p \rangle_p(t) = \frac{1}{N_p} \sum_1^{N_p} \phi_p \quad (5.1)$$

where N_p is the number of particles in the ensemble. Fig. 5.8 shows the time evolution of the particle-averaged streamwise velocity component $\langle v_p \rangle_p$ (y-direction), while Fig. 5.9 shows the transverse components $\langle u_p \rangle_p$ and $\langle w_p \rangle_p$ (x- and z-directions, respectively). The streamwise velocity component first undergoes a transient phase before stabilizing around 0 m/s. As expected, the transient period for $U_F = 0.12$ m/s is the shortest, as the expected bed height for this case was chosen to initialize the bed height for all cases. The lower-velocity cases undergo a more pronounced compression (larger downward average velocity), while the higher-velocity cases undergo an expansion that spans a longer period compared to the other cases. No transition period can be observed for both transverse average velocity components. All velocity components fluctuate around zero 0 m/s, indicating no net movement of the fluidized bed.

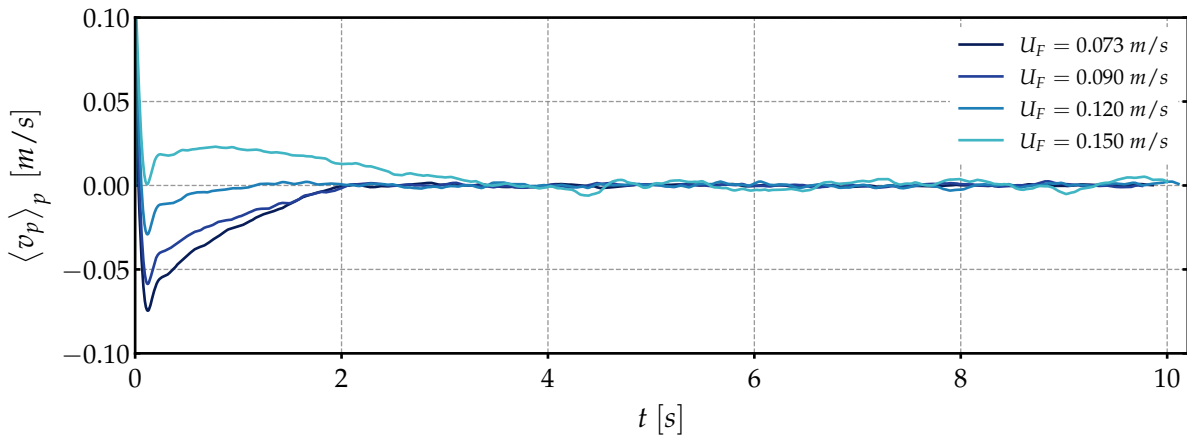


Figure 5.8: Time evolution of the particle average streamwise velocity component, y-direction

5.3. Particle resolved direct numerical simulation of a 2100 liquid–solid fluidized bed

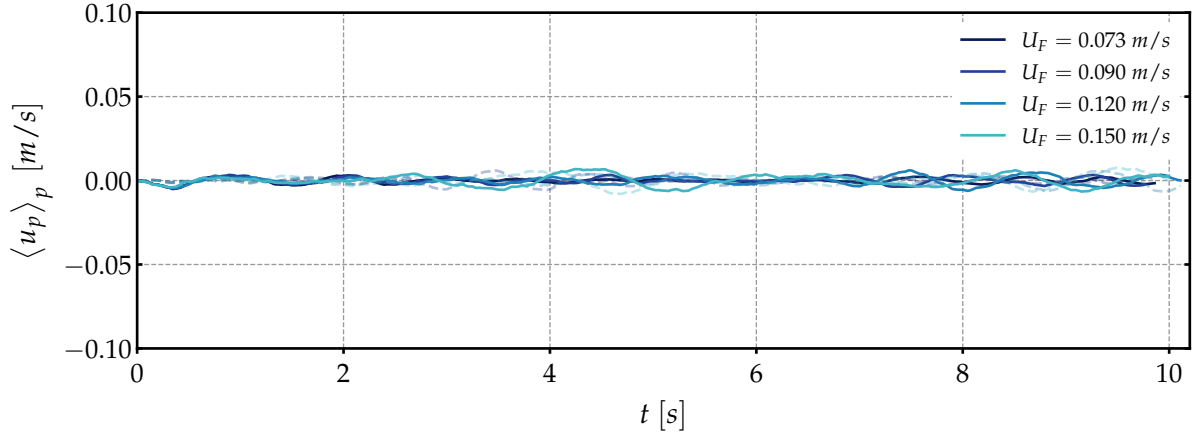


Figure 5.9: Time evolution of the particle average transverse velocity component, continuous line x-direction, dashed lines z-direction

To investigate the solid phase fluctuation, we define the particle variance operator for a particle-related quantity $\phi_p(p, t)$ as follows:

$$\langle \phi_p'^2 \rangle_p(t) = \frac{1}{N_p} \sum_1^{N_p} (\phi_p')^2 \quad (5.2)$$

where ϕ_p' is the fluctuation or the deviation from the particle mean:

$$\phi_p'(p, t) = \phi_p - \langle \phi_p \rangle_p \quad (5.3)$$

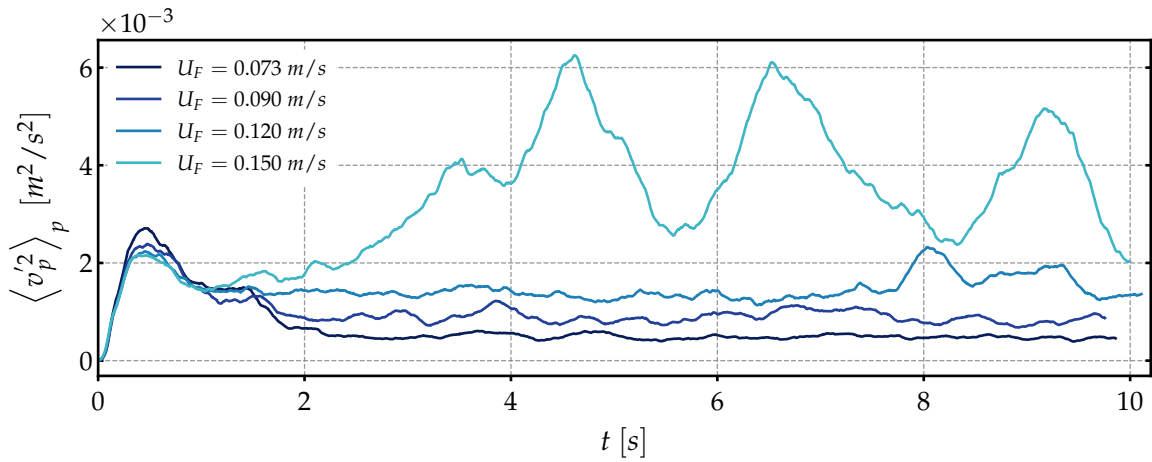
Fig. 5.10 shows the time evolution of the particle variance for the three components of the particle velocity. Overall, the velocity variance increases with increasing fluidization velocity. The transverse component of the velocity variances exhibits low-amplitude, high-frequency fluctuations (Fig. 5.10b), while the streamwise component is much smoother (Fig. 5.10a). On the other hand, higher amplitude, lower frequency are observed for the streamwise variance component, particularly prominent for the $U_F = 0.150$ m/s fluidization velocity.

Another important observation is that the streamwise velocity variance is always greater than the lateral components, regardless of the fluidization velocity. This behavior is best captured using the anisotropy coefficient K_{anis} :

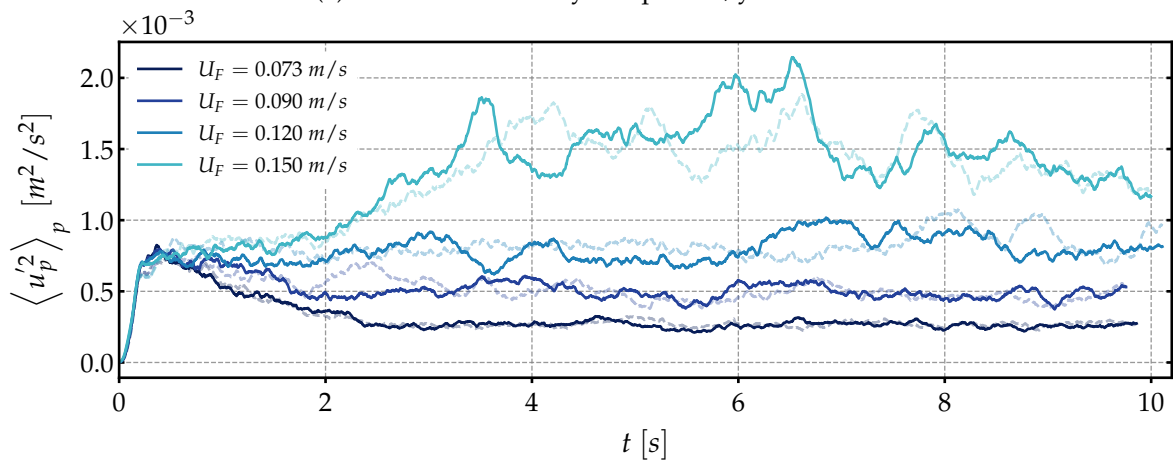
$$K_{\text{anis}} = \sqrt{\frac{\langle v_p'^2 \rangle_p}{\frac{1}{2} (\langle u_p'^2 \rangle_p + \langle w_p'^2 \rangle_p)}} \quad (5.4)$$

Its time evolution is displayed in Fig. 5.11. After the initial transient period, we can see that the value of the anisotropy coefficient oscillates around the same value for the

5.3. Particle resolved direct numerical simulation of a 2100 liquid–solid fluidized bed



(a) Streamwise velocity component, y-direction



(b) Transverse velocity component, continuous line x-direction, dashed lines z-direction

Figure 5.10: Time evolution of the particle velocity variance

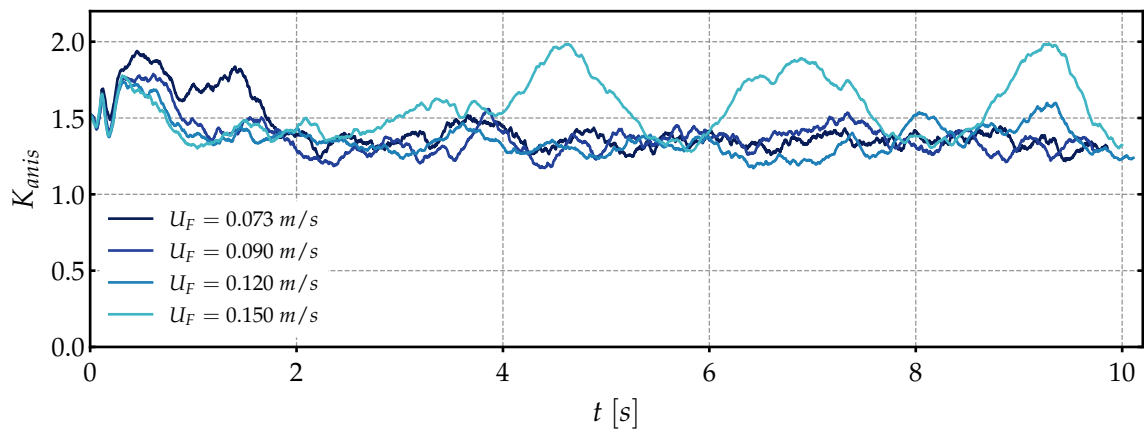


Figure 5.11: Anisotropy coefficient

5.3. Particle resolved direct numerical simulation of a 2100 liquid–solid fluidized bed

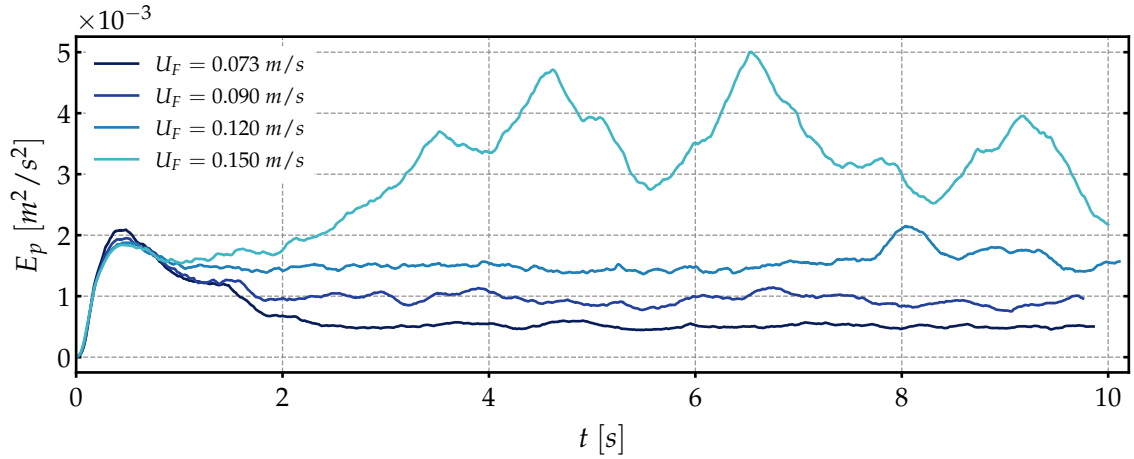


Figure 5.12: Fluctuating kinetic energy

fluidization velocities 0.073 m/s, 0.090 m/s, and 0.120 m/s, while at $U_F = 0.150$ m/s, the amplitude of the oscillations is higher.

The time evolution of the total fluctuating kinetic energy of the particles is depicted in Fig. 5.12, as calculated using Eq. (5.5). Not surprisingly, the graph closely mirrors the behavior of the variance in the streamwise velocity component, which carries most of the kinetic energy in this flow configuration.

$$E_p = \frac{1}{2} \left(\langle v_p'^2 \rangle_p + \langle u_p'^2 \rangle_p + \langle w_p'^2 \rangle_p \right) \quad (5.5)$$

In order to compare our results with the experimental data of Aguilar-Corona, Zenit, and Masbarnat [2] and the numerical results of Ozel et al. [86], the average solid fraction in the fluidized bed (α_b) must be calculated. This was accomplished by taking transversal slices (perpendicular to the streamwise direction) of the fluidized bed at regular intervals. The areas of the disks, formed by the intersection of each plane with the spherical particles, were summed up and divided by the cross-sectional area of the domain to obtain the average solid volume fraction at that elevation.

This procedure was repeated for each time step, generating a profile of the solid volume fraction at different times ($\bar{\alpha}(t, y)$). These profiles were then averaged over time, resulting in the time-averaged profile shown in Fig. 5.13. For the time-averaging process, the operations were conducted over a timeframe that started at $t_0 = 5$ s:

$$\langle \bar{\alpha} \rangle_t (y_j) = \frac{1}{|T|} \sum_{t_m \geq t_0} \bar{\alpha}(t_m, y_j) \quad (5.6)$$

where $|T|$ is the cardinality of the set T representing the set of time values $t_m \geq 5$ s. This decision was based on the time evolution depicted in the previous figures, which indicated that the transition phase was complete around this time. However, for a

5.3. Particle resolved direct numerical simulation of a 2100 liquid–solid fluidized bed

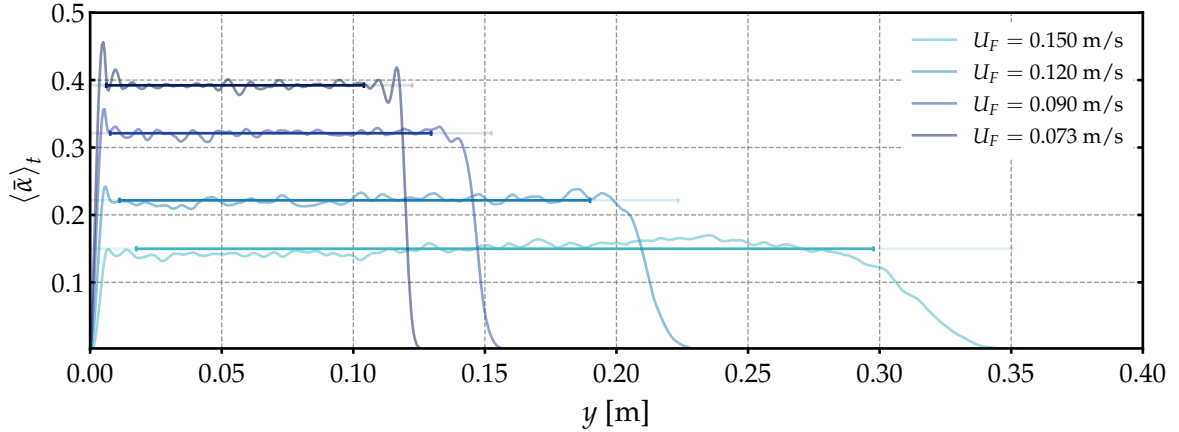


Figure 5.13: Time-averaged profile of solid volume fraction

flow velocity $U_F = 0.150$ m/s, more simulation time might be necessary to confirm the establishment of the flow.

As evident from Fig. 5.13, the volume fraction is relatively uniform throughout the height of the bed. However, a transition zone can be observed between the bed and the pure fluid region. The thickness of this transition zone is directly proportional to the fluidization speed: the lower the fluidization velocity, the narrower the transition zone. The thickness of this transition zone makes it challenging to precisely estimate the height of the bed, which is needed to compute the averaged solid volume fraction α within the bed. We chose to approximate the bed height h_b as the time average of the maximal vertical position of the particles:

$$h_b = \frac{1}{|T|} \sum_{t_m \geq t_0} y_{max}(t_m)$$

$$y_{max}(t_m) = \max\{y_p(t_m) \mid p \in [1, N_p]\}$$

Fig. 5.14 shows the time evolution of y_{max} alongside a box plot to showcase its fluctuation range. In order to exclude the influence of bed boundaries and inhomogeneities when calculating the average volume fraction, the time-averaged value $\langle \bar{\alpha} \rangle_t(y_j)$ is spatially averaged over a specific range in the vertical direction, denoted as H . This range is defined as $H = \{y_j \mid 0.05 \times h_b \leq y_j \leq 0.85 \times h_b\}$. This selection filters out edge effects, such as the wide transition zones seen at high fluidization speeds or particle accumulation at the bed's bottom when the fluidization speed is low.

$$\alpha_b = \frac{1}{|H|} \sum_{y_j \in H} \langle \bar{\alpha} \rangle_t(y_j) \quad (5.7)$$

The resulting average volume fractions are displayed in Fig. 5.15 as a function of the fluidization velocity. The results are then compared with experimental data from Aguilar-Corona [1], numerical results from [86], and the empirical correlation proposed by Richardson and Zaki [96] with $n = 2.4$ and $U_{F0} = 0.24$ m/s as suggested by Aguilar-Corona [1]. As shown in Figure 5.15, our results align well with both the numerical and

5.3. Particle resolved direct numerical simulation of a 2100 liquid–solid fluidized bed

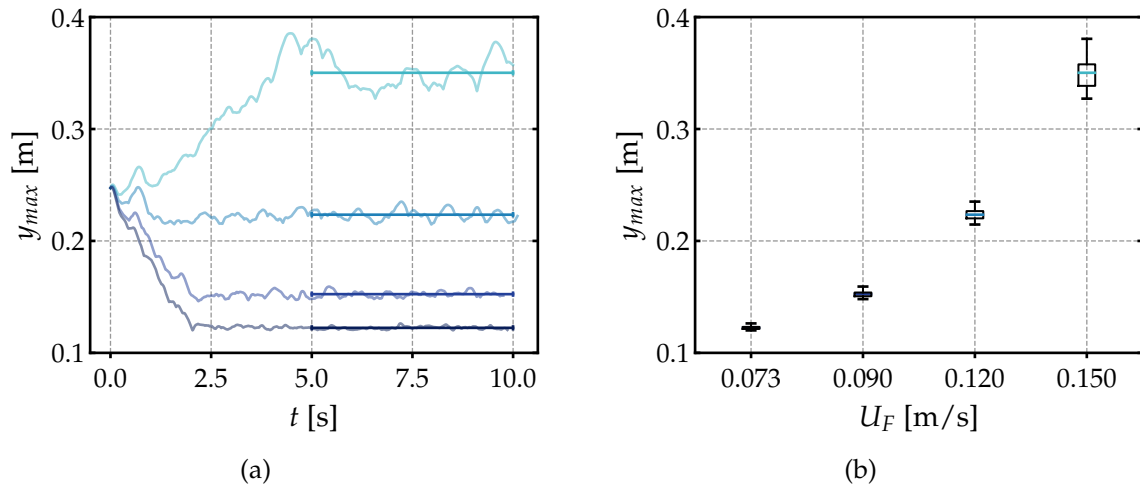


Figure 5.14: (a): Time evolution of maximum axial particle position at different fluidization velocities: $U_F = 0.073$ m/s, 0.090 m/s, 0.120 m/s, and 150 m/s. The continuous lines represent the average mean value of y_{max} over the range $t = [5 \text{ s}, 10 \text{ s}]$ (b) Box plot of the distribution of y_{max} (m). The box represents the interquartile range (IQR), the line inside the box is the mean, the whiskers extend to the minimum and maximum values.

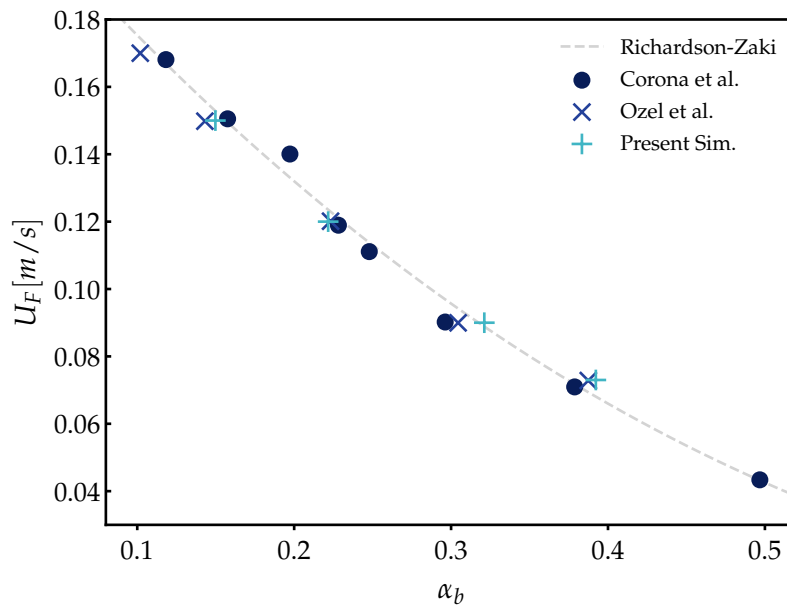


Figure 5.15: Fluidization velocity with respect to the bed solid concentration.

5.3. Particle resolved direct numerical simulation of a 2100 liquid–solid fluidized bed

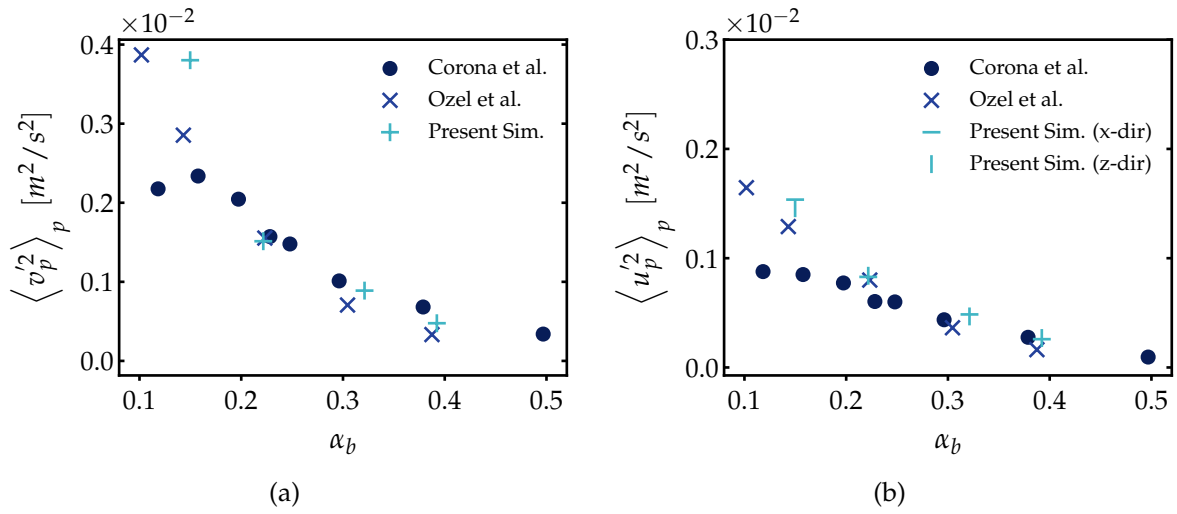


Figure 5.16: Variance of axial (a) and transverse (b) particle velocity with respect to the bed solid concentration.

experimental references. They also agree with the prediction of the fluidization law, as given by the empirical correlation with $n = 2.4$ and $U_{F0} = 0.24$ m/s, which accurately predicts the observed trends in the data.

The time average of the variance of the particle velocities is computed for all directions and displayed in Fig. 5.16, alongside previous experimental and numerical results. Our method accurately predicts the velocity variance for the three components, for solid fractions $\alpha > 0.2$. The superimposition of the two transverse components, x and z, attests the convergence of the statistics. For the lowest volume fraction (highest fluidization speed), our simulation overestimates the variance of the three components and the two transverse components no longer match.

The anisotropy coefficient and the total kinetic energy for the particles are plotted as a function of volume fraction in Fig. 5.17a. From the graph, we observe that the values obtained are slightly lower than those of [86]. However, we also find that there is no dependence of the anisotropy coefficient, k_{anis} , on the averaged particle volume fraction. This is true except for the non-converged case, which corresponds to the highest fluidization velocity of $U_F = 0.15$ m/s. Similar trends are observed for the kinetic energy.

Finally, this analysis demonstrates that the original approach developed during this PhD allows simulating liquid-solid fluidized bed with the same accuracy that [86, 115].

5.3. Particle resolved direct numerical simulation of a 2100 liquid–solid fluidized bed

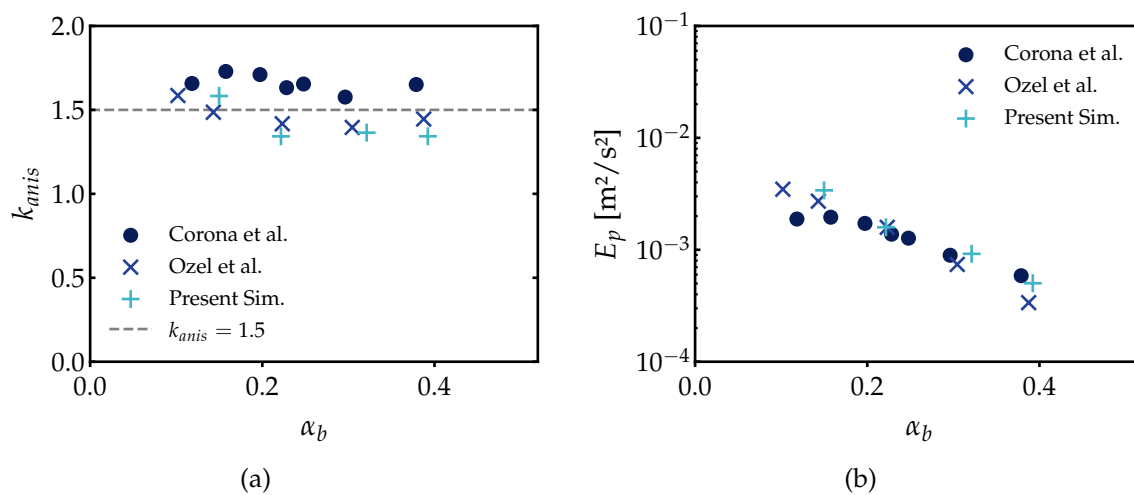


Figure 5.17: Anisotropy coefficient of the particle velocity fluctuations as a function of the bed solid concentration

6

CONCLUSIONS AND FUTURE WORK

Solid-fluid flows are fundamental to a wide array of industrial operations and natural phenomena, yet their inherent complexity makes them notoriously challenging to study and predict. While traditional analytical and experimental techniques offer some insights, they have distinct limitations in terms of scope and resolution. The advent of improved computational capabilities and numerical methodologies has opened a new frontier, making Direct Numerical Simulations (DNS) an increasingly essential tool for gaining deeper understanding of the intricate dynamics involved in these flows.

Within the context of this thesis, we have carried out a series of modifications to the Front Tracking method implemented in the TrioCFD software, specifically to enable the simulation of dense fluid-particles flows. The method is based on the one-fluid formalism, where the rigidity constraint is handled through a viscous penalty method. In practical terms, this means that a large viscosity ratio between the fluid and the particles is imposed. This maneuver ensures that the deformation tensor in the simulation approaches zero in an asymptotic manner, effectively treating the solid phase as a highly viscous fluid. As a result, phase coupling between the solid and fluid phases is seamlessly carried out by the pressure solver without the need for any added forcing terms in the governing equations to enforce the rigid body motion.

Our approach falls under the broader category of non-boundary-fitted methods, commonly referred to as Fictitious Domains methods. Utilizing a non-conforming and fixed simulation mesh offers computational advantages but comes with a downside: it provides a less accurate description of the interface between the fluid and solid phases. Even when using the front-tracking method, where the interface is represented by a massless surface mesh, its projection onto the simulation grid tends to diffuse the interface over a thickness equivalent to one grid cell. To address this issue and ensure precise momentum coupling, it's crucial to accurately model how fluid properties are represented in grid cells intersected by the interface. To address this and ensure accurate momentum coupling, special care must be taken when modeling fluid properties in the grid cells that are intersected by the interface.

For that purpose, we adopted two specific methods for calculating the equivalent viscosity in cells that are crossed by the interface. The first method uses harmonic

averaging, which produces significantly better outcomes than a simple arithmetic average at comparable grid resolutions. The second method employs a step function, which, when used in conjunction with the appropriate grid resolution, can improve simulation accuracy even at coarser grid scales. Importantly, these approach also counteract some of the shortcomings associated with the viscous penalty approach, particularly the issue of artificially increasing viscous dissipation. This is achieved by allowing a degree of control over the apparent hydrodynamic diameter of the particle, which in turn influences the drag forces acting upon it.

For modeling short-range particle interactions, we employed a combined collision model that integrates both the solid energy dissipation aspects and the viscous effects arising from fluid drainage during the collision events. The model is based on a harmonic oscillator model where the spring stiffness is adjusted mid-collision to achieve the desired rebound velocity. This adjustment is determined using empirical relationships between the Stokes number at the point of collision impact and the apparent coefficient of restitution. This approach negates the necessity for additional closure laws specifically for lubrication effects, thereby minimizing the number of numerical parameters that need to be adjusted during simulations.

We subjected our simulation framework to rigorous testing against established experimental benchmarks to validate its accuracy and reliability. For the hydrodynamics, we simulated the motion of a settling sphere based on the seminal work of Cate et al. [18], observing good agreement across a range of terminal Reynolds numbers from 1 to 32. Following that, we focused on validating our collision model by simulating the trajectory of a bouncing spherical particle based on experiments conducted by Gondret, Lance, and Petit [53]. Again, our simulations were consistent with the experimental findings.

Expanding upon this, we demonstrated the method's capability to simulate dense granular flows involving numerous interacting particles. Specifically, we reproduced the fluidized bed experiments of Aguilar-Corona [1], involving more than 2000 particles at various fluidization velocities. Key parameters such as particle velocity variance, coefficient of anisotropy, and the governing fluidization laws were all calculated and analyzed. Our results showed good quantitative agreement with the experimental data for solid fractions ranging from 0.2 to 0.4, aligning well with the performances reported in the study by Ozel et al. [86].

For future research, several areas can be further explored to enhance the capabilities and reliability of the proposed numerical methodology for simulating solid-fluid flows.

Firstly, improved stability can be attained by incorporating a more sophisticated time integration method and/or convective discretization scheme. The current model employs an Euler explicit method combined with second-order differences for handling the convective term in the equations. While this scheme has been sufficient for the flow regimes studied in this work, it's worth noting that Euler explicit methods are known for their susceptibility to numerical oscillations. Such oscillations have not been observed in this thesis work but could potentially become a concern when moving into regimes with higher Stokes numbers. It's plausible that switching to a higher-order integration method could significantly enhance numerical stability in such cases. Another option could be to implement a higher-order scheme for the convective term specifically, such as the Quadratic Upstream Interpolation for Convective Kinematics (QUICK) scheme.

Secondly, in terms of parallelism and efficiency the implementation of a contact detection algorithm is worth investigating. In the scope of this thesis work, the number of particles simulated was relatively small, making the computational time spent on collision detection less critical compared to the time spent on the viscous penalization aspect. However, as we aim to extend the model to handle larger numbers of particles, the computational time needed for collision detection may become a bottleneck. This shift in computational focus highlights the need for efficient contact detection algorithms to identify potential collisions among particles quickly and accurately.

The third point to consider is the issue of non-sphericity and particle rotation. Real-world particles are seldom perfectly smooth and spherical, and the behavior of irregular particles is quite different from that of idealized spheres. Thus, extending the model to handle non-spherical particles and incorporating rotation dynamics would bring the simulations closer to real-life scenarios. This would make the model vastly more useful for industrial applications where particle shapes can vary significantly.

Fourthly, the current work confines particles within a box, limiting the types of systems that can be modeled. The next logical step is to allow particles to freely exit and enter the simulation domain. This would facilitate the simulation of more complex systems like circulating beds. However, achieving this will necessitate the development of new techniques for handling boundary conditions.

Finally, the influence of temperature on flow dynamics remains an unexplored avenue in the present work. We expect different dynamics at higher temperatures but lack sufficient data to predict how exactly it will affect the flow. Incorporating thermal effects into the model would enable a more comprehensive understanding of flow characteristics under varying temperature conditions. This is particularly relevant for processes where temperature gradients exist or where thermal effects play a pivotal role in the system's overall performance.



BIBLIOGRAPHY

- [1] A. Aguilar-Corona. "Agitation des particules dans un lit fluidisé liquide. Etude expérimentale". PhD thesis. Institut National Polytechnique de Toulouse, 2008.
- [2] A. Aguilar-Corona, R. Zenit, and O. Masbernat. "Collisions in a Liquid Fluidized Bed". In: *International Journal of Multiphase Flow* 37 (2011), pp. 695–705. doi: [10.1016/j.ijmultiphaseflow.2011.02.004](https://doi.org/10.1016/j.ijmultiphaseflow.2011.02.004).
- [3] F. Aulery et al. "Energy Transfer Process of Anisothermal Wall-Bounded Flows". In: *Physics Letters A* 379 (2015), pp. 1520–1526. doi: [10.1016/j.physleta.2015.03.022](https://doi.org/10.1016/j.physleta.2015.03.022).
- [4] T. R. Auton, J. C. R. Hunt, and M. Prud'Homme. "The Force Exerted on a Body in Inviscid Unsteady Non-Uniform Rotational Flow". In: *Journal of Fluid Mechanics* 197 (1988), pp. 241–257. doi: [10.1017/S0022112088003246](https://doi.org/10.1017/S0022112088003246).
- [5] H. M. Barkla and L. J. Auchterlonie. "The Magnus or Robins Effect on Rotating Spheres". In: *Journal of Fluid Mechanics* 47 (1971), pp. 437–447. doi: [10.1017/S0022112071001150](https://doi.org/10.1017/S0022112071001150).
- [6] A. B. Basset. *A Treatise on Hydrodynamics, with Numerous Examples*. Cambridge [Eng.] Deighton, Bell and co.; 1888.
- [7] O. Behar, B. Grange, and G. Flamant. "Design and Performance of a Modular Combined Cycle Solar Power Plant Using the Fluidized Particle Solar Receiver Technology". In: *Energy Conversion and Management* 220 (2020), p. 113108. doi: [10.1016/j.enconman.2020.113108](https://doi.org/10.1016/j.enconman.2020.113108).
- [8] H. Benoit et al. "On-Sun Demonstration of a 750°C Heat Transfer Fluid for Concentrating Solar Systems: Dense Particle Suspension in Tube". In: *Solar Energy* 118 (2015), pp. 622–633. doi: [10.1016/j.solener.2015.06.007](https://doi.org/10.1016/j.solener.2015.06.007).
- [9] H. Benoit et al. "Review of Heat Transfer Fluids in Tube-Receiver Used in Concentrating Solar Thermal Systems: Properties and Heat Transfer Coefficients". In: *Renewable and Sustainable Energy Reviews* 55 (2016), pp. 298–315. doi: [10.1016/j.rser.2015.10.059](https://doi.org/10.1016/j.rser.2015.10.059).
- [10] E. Biegert, B. Vowinckel, and E. Meiburg. "A Collision Model for Grain-Resolving Simulations of Flows over Dense, Mobile, Polydisperse Granular Sediment Beds". In: *Journal of Computational Physics* 340 (2017), pp. 105–127. doi: [10.1016/j.jcp.2017.03.035](https://doi.org/10.1016/j.jcp.2017.03.035).
- [11] B. Boissiere et al. "Experimental Hydrodynamic Study of Gas-Particle Dense Suspension Upward Flow for Application as New Heat Transfer and Storage Fluid". In: *The Canadian Journal of Chemical Engineering* 93 (2015), pp. 317–330. doi: [10.1002/cjce.22087](https://doi.org/10.1002/cjce.22087).

- [12] J. C. Brändle de Motta et al. “Numerical Modelling of Finite-Size Particle Collisions in a Viscous Fluid”. In: *Physics of Fluids* 25 (2013), p. 083302. doi: [10.1063/1.4817382](https://doi.org/10.1063/1.4817382).
- [13] W. P. Breugem. “A Combined Soft-Sphere Collision/Immersed Boundary Method for Resolved Simulations of Particulate Flows”. In: *ASME 2010 3rd Joint US-European Fluids Engineering Summer Meeting: Volume 1, Symposia – Parts A, B, and C*. Montreal, Quebec, Canada: ASME, 2010, pp. 2381–2392. doi: [10.1115/FEDSM-ICNMM2010-30634](https://doi.org/10.1115/FEDSM-ICNMM2010-30634).
- [14] R. Bridson. “Fast Poisson Disk Sampling in Arbitrary Dimensions.” In: *SIGGRAPH sketches* 10 (2007), p. 1. doi: [10.1145/1278780.1278807](https://doi.org/10.1145/1278780.1278807).
- [15] B. Bunner and G. Tryggvason. “Effect of Bubble Deformation on the Properties of Bubbly Flows”. In: *Journal of Fluid Mechanics* 495 (2003), pp. 77–118. doi: [10.1017/S0022112003006293](https://doi.org/10.1017/S0022112003006293).
- [16] Jean-Paul Caltagirone and Stéphane Vincent. “Sur une méthode de pénalisation tensorielle pour la résolution des équations de Navier–Stokes”. In: *Comptes Rendus de l’Académie des Sciences - Series IIB - Mechanics* 329 (2001), pp. 607–613.
- [17] C. S. Campbell and C. E. Brennen. “Computer Simulation of Granular Shear Flows”. In: *Journal of Fluid Mechanics* 151 (1985), pp. 167–188. doi: [10.1017/S002211208500091X](https://doi.org/10.1017/S002211208500091X).
- [18] A. ten Cate et al. “Particle Imaging Velocimetry Experiments and Lattice-Boltzmann Simulations on a Single Sphere Settling under Gravity”. In: *Physics of Fluids* 14 (2002), pp. 4012–4025. doi: [10.1063/1.1512918](https://doi.org/10.1063/1.1512918).
- [19] Y. Chen and C. R. Müller. “A Dirichlet Boundary Condition for the Thermal Lattice Boltzmann Method”. In: *International Journal of Multiphase Flow* 123 (2020), p. 103184. doi: [10.1016/j.ijmultiphaseflow.2019.103184](https://doi.org/10.1016/j.ijmultiphaseflow.2019.103184).
- [20] N. S. Cheng. “Comparison of Formulas for Drag Coefficient and Settling Velocity of Spherical Particles”. In: *Powder Technology* 189 (2009), pp. 395–398. doi: [10.1016/j.powtec.2008.07.006](https://doi.org/10.1016/j.powtec.2008.07.006).
- [21] A. J. Chorin. “Numerical Solution of the Navier-Stokes Equations”. In: *Mathematics of Computation* 22 (1968), pp. 745–762. doi: [10.1090/S0025-5718-1968-0242392-2](https://doi.org/10.1090/S0025-5718-1968-0242392-2).
- [22] P. Cleary. “DEM Prediction of Industrial and Geophysical Particle Flows”. In: *Particuology* 8 (2010), pp. 106–118. doi: [10.1016/j.partic.2009.05.006](https://doi.org/10.1016/j.partic.2009.05.006).
- [23] R. Clift, John R. Grace, and Martin E. Weber. *Bubbles, Drops, and Particles*. New York: Academic Press, 1978.
- [24] COP28 Agreement Signals “Beginning of the End” of the Fossil Fuel Era | UNFCCC. 2024. URL: <https://unfccc.int/news/cop28-agreement-signals-beginning-of-the-end-of-the-fossil-fuel-era>.
- [25] Copernicus: 2023 Is the Hottest Year on Record, with Global Temperatures Close to the 1.5°C Limit | Copernicus. 2024. URL: <https://climate.copernicus.eu/copernicus-2023-hottest-year-record>.

- [26] P. Costa et al. "Collision Model for Fully Resolved Simulations of Flows Laden with Finite-Size Particles". In: *Physical Review E* 92 (2015), p. 053012. doi: [10.1103/PhysRevE.92.053012](https://doi.org/10.1103/PhysRevE.92.053012).
- [27] R. G. Cox and H. Brenner. "The Slow Motion of a Sphere through a Viscous Fluid towards a Plane Surface—II Small Gap Widths, Including Inertial Effects". In: *Chemical Engineering Science* 22 (1967), pp. 1753–1777. doi: [10.1016/0009-2509\(67\)80208-2](https://doi.org/10.1016/0009-2509(67)80208-2).
- [28] C. T. Crowe et al. *Multiphase Flows with Droplets and Particles*. 0th ed. CRC Press, 2011. doi: [10.1201/b11103](https://doi.org/10.1201/b11103).
- [29] P. A. Cundall and O. D. L. Strack. "A Discrete Numerical Model for Granular Assemblies". In: *Géotechnique* 29 (1979), pp. 47–65. doi: [10.1680/geot.1979.29.1.47](https://doi.org/10.1680/geot.1979.29.1.47).
- [30] J. M. Davies. "The Aerodynamics of Golf Balls". In: *Journal of Applied Physics* 20 (1949), pp. 821–828. doi: [10.1063/1.1698540](https://doi.org/10.1063/1.1698540).
- [31] J. M. Delhaye. *Thermohydraulique des réacteurs nucléaires*. Les Ulis: EDP sciences, 2008.
- [32] Y. Deng et al. "Dense Upflow Fluidized Bed (DUFb) Solar Receivers of High Aspect Ratio: Different Fluidization Modes through Inserting Bubble Rupture Promoters". In: *Chemical Engineering Journal* 418 (2021), p. 129376. doi: [10.1016/j.cej.2021.129376](https://doi.org/10.1016/j.cej.2021.129376).
- [33] R. Di Felice. "The Voidage Function for Fluid-Particle Interaction Systems". In: *International Journal of Multiphase Flow* 20 (1994), pp. 153–159. doi: [10.1016/0301-9322\(94\)90011-6](https://doi.org/10.1016/0301-9322(94)90011-6).
- [34] A. Donev, S. Torquato, and F. H. Stillinger. "Neighbor List Collision-Driven Molecular Dynamics Simulation for Nonspherical Hard Particles.: II. Applications to Ellipses and Ellipsoids". In: *Journal of Computational Physics* 202 (2005), pp. 765–793. doi: [10.1016/j.jcp.2004.08.025](https://doi.org/10.1016/j.jcp.2004.08.025).
- [35] A. du Cluzeau, G. Bois, and A. Toutant. "Analysis and Modelling of Reynolds Stresses in Turbulent Bubbly Up-Flows from Direct Numerical Simulations". In: *Journal of Fluid Mechanics* 866 (2019), pp. 132–168. doi: [10.1017/jfm.2019.100](https://doi.org/10.1017/jfm.2019.100).
- [36] A. du Cluzeau et al. "Analysis and Modeling of Bubble-Induced Agitation from Direct Numerical Simulation of Homogeneous Bubbly Flows". In: *Physical Review Fluids* 7 (2022), p. 044604. doi: [10.1103/PhysRevFluids.7.044604](https://doi.org/10.1103/PhysRevFluids.7.044604).
- [37] A. du Cluzeau et al. "On Bubble Forces in Turbulent Channel Flows from Direct Numerical Simulations". In: *Journal of Fluid Mechanics* 882 (2020), A27. doi: [10.1017/jfm.2019.807](https://doi.org/10.1017/jfm.2019.807).
- [38] D. Dupuy, A. Toutant, and F. Bataille. "Effect of the Reynolds Number on Turbulence Kinetic Energy Exchanges in Flows with Highly Variable Fluid Properties". In: *Physics of Fluids* 31 (2019), p. 015104. doi: [10.1063/1.5080769](https://doi.org/10.1063/1.5080769).

- [39] D. Dupuy, A. Toutant, and F. Bataille. “Turbulence Kinetic Energy Exchanges in Flows with Highly Variable Fluid Properties”. In: *Journal of Fluid Mechanics* 834 (2018), pp. 5–54. doi: [10.1017/jfm.2017.729](https://doi.org/10.1017/jfm.2017.729).
- [40] A. Džiugys and B. Peters. “An Approach to Simulate the Motion of Spherical and Non-Spherical Fuel Particles in Combustion Chambers”. In: *Granular Matter* 3 (2001), pp. 231–266. doi: [10.1007/PL00010918](https://doi.org/10.1007/PL00010918).
- [41] M. Ebert et al. “Operational Experience of a Centrifugal Particle Receiver Prototype”. In: *AIP Conference Proceedings* 2126 (2019), p. 030018. doi: [10.1063/1.5117530](https://doi.org/10.1063/1.5117530).
- [42] S. Elghobashi. “Particle-Laden Turbulent Flows: Direct Simulation and Closure Models”. In: *Applied Scientific Research* 48 (1991), pp. 301–314. doi: [10.1007/BF02008202](https://doi.org/10.1007/BF02008202).
- [43] A. Esteghamatian et al. “Particle Resolved Simulations of Liquid/Solid and Gas/Solid Fluidized Beds”. In: *Physics of Fluids* 29 (2017). doi: [10.1063/1.4979137](https://doi.org/10.1063/1.4979137).
- [44] Z. G. Feng and E. E. Michaelides. “Interparticle Forces and Lift on a Particle Attached to a Solid Boundary in Suspension Flow”. In: *Physics of Fluids* 14 (2002), pp. 49–60. doi: [10.1063/1.1426389](https://doi.org/10.1063/1.1426389).
- [45] Z. G. Feng, E. E. Michaelides, and S. Mao. “A Three-Dimensional Resolved Discrete Particle Method for Studying Particle-Wall Collision in a Viscous Fluid”. In: *Journal of Fluids Engineering* 132 (2010). doi: [10.1115/1.4002432](https://doi.org/10.1115/1.4002432).
- [46] *Final Report Summary - CSP2 (Concentrated Solar Power in Particles) | FP7 | CORDIS | European Commission*. <https://cordis.europa.eu/project/id/282932/reporting>.
- [47] S. F. Foerster et al. “Measurements of the Collision Properties of Small Spheres”. In: *Physics of Fluids* 6 (1994), pp. 1108–1115. doi: [10.1063/1.868282](https://doi.org/10.1063/1.868282).
- [48] W. Fuqiang et al. “Progress in Concentrated Solar Power Technology with Parabolic Trough Collector System: A Comprehensive Review”. In: *Renewable and Sustainable Energy Reviews* 79 (2017), pp. 1314–1328. doi: [10.1016/j.rser.2017.05.174](https://doi.org/10.1016/j.rser.2017.05.174).
- [49] S. Gallier et al. “A Fictitious Domain Approach for the Simulation of Dense Suspensions”. In: *Journal of Computational Physics* 256 (2014), pp. 367–387. doi: [10.1016/j.jcp.2013.09.015](https://doi.org/10.1016/j.jcp.2013.09.015).
- [50] R. Glowinski et al. “A Distributed Lagrange Multiplier/Fictitious Domain Method for Particulate Flows”. In: *International Journal of Multiphase Flow* 25 (1999), pp. 755–794. doi: [10.1016/S0301-9322\(98\)00048-2](https://doi.org/10.1016/S0301-9322(98)00048-2).
- [51] R. Glowinski et al. “A Fictitious Domain Approach to the Direct Numerical Simulation of Incompressible Viscous Flow Past Moving Rigid Bodies: Application to Particulate Flow”. In: *Journal of Computational Physics* 169 (2001), pp. 363–426. doi: [10.1006/jcph.2000.6542](https://doi.org/10.1006/jcph.2000.6542).

Bibliography

- [52] H. Goldstein, C. P. Poole, and J. Safko. *Classical Mechanics*. Tercera edición. Estados Unidos: Pearson Education, Inc., 2002.
- [53] P. Gondret, M. Lance, and L. Petit. “Bouncing Motion of Spherical Particles in Fluids”. In: *Physics of Fluids* 14 (2002), p. 643. doi: [10.1063/1.1427920](https://doi.org/10.1063/1.1427920).
- [54] W. R. A. Goossens. “Review of the Empirical Correlations for the Drag Coefficient of Rigid Spheres”. In: *Powder Technology* 352 (2019), pp. 350–359. doi: [10.1016/j.powtec.2019.04.075](https://doi.org/10.1016/j.powtec.2019.04.075).
- [55] Ronny Gueguen et al. “Gas-Solid Flow in a Fluidized-Particle Tubular Solar Receiver: Off-Sun Experimental Flow Regimes Characterization”. In: *Energies* 14 (2021), p. 7392. doi: [10.3390/en14217392](https://doi.org/10.3390/en14217392).
- [56] H. C. Hamaker. “The London—van Der Waals Attraction between Spherical Particles”. In: *Physica* 4 (1937), pp. 1058–1072. doi: [10.1016/S0031-8914\(37\)80203-7](https://doi.org/10.1016/S0031-8914(37)80203-7).
- [57] M. S. Hamidi et al. “Assessment of a Coupled Vof-Front-Tracking/Dem Method for Simulating Fluid-Particles Flows”. In: *International Journal of Multiphase Flow* 165 (2023).
- [58] F. H. Harlow and J. E. Welch. “Numerical Calculation of Time-Dependent Viscous Incompressible Flow of Fluid with Free Surface”. In: *The Physics of Fluids* 8 (1965), pp. 2182–2189. doi: [10.1063/1.1761178](https://doi.org/10.1063/1.1761178).
- [59] Y. L. He et al. “Perspective of Concentrating Solar Power”. In: *Energy* 198 (2020), p. 117373. doi: [10.1016/j.energy.2020.117373](https://doi.org/10.1016/j.energy.2020.117373).
- [60] H. Hertz. “Über die Berührung Fester Elastischer Körper (on the contact of elastic solids).” In: *J. Reine Angew. Math.* 1882 (1882), pp. 156–171. doi: [10.1515/crll.1882.92.156](https://doi.org/10.1515/crll.1882.92.156).
- [61] *High Temperature Concentrated Solar Thermal Power Plan with Particle Receiver and Direct Thermal Storage | NEXT-CSP Project | Fact Sheet | H2020 | CORDIS | European Commission*. <https://cordis.europa.eu/project/id/727762>.
- [62] J. E. Hilton and P. W. Cleary. “The Influence of Particle Shape on Flow Modes in Pneumatic Conveying”. In: *Chemical Engineering Science* 66 (2011), pp. 231–240. doi: [10.1016/j.ces.2010.09.034](https://doi.org/10.1016/j.ces.2010.09.034).
- [63] A. T. Hjelmfelt and L. F. Mockros. “Motion of Discrete Particles in a Turbulent Fluid”. In: *Applied Scientific Research* 16 (1966), pp. 149–161. doi: [10.1007/BF00384062](https://doi.org/10.1007/BF00384062).
- [64] C. K. Ho et al. “Highlights of the High-Temperature Falling Particle Receiver Project: 2012 - 2016”. In: *AIP Conference Proceedings* 1850 (2017), p. 030027. doi: [10.1063/1.4984370](https://doi.org/10.1063/1.4984370).
- [65] B. P. B. Hoomans et al. “Discrete Particle Simulation of Bubble and Slug Formation in a Two-Dimensional Gas-Fluidised Bed: A Hard-Sphere Approach”. In: *Chemical Engineering Science* 51 (1996), pp. 99–118. doi: [10.1016/0009-2509\(95\)00271-5](https://doi.org/10.1016/0009-2509(95)00271-5).

- [66] E. Izard, T. Bonometti, and L. Lacaze. “Modelling the Dynamics of a Sphere Approaching and Bouncing on a Wall in a Viscous Fluid”. In: *Journal of Fluid Mechanics* 747 (2014), pp. 422–446. doi: [10.1017/jfm.2014.145](https://doi.org/10.1017/jfm.2014.145).
- [67] R. Jacob et al. “Embodied Energy and Cost of High Temperature Thermal Energy Storage Systems for Use with Concentrated Solar Power Plants”. In: *Applied Energy* 180 (2016), pp. 586–597. doi: [10.1016/j.apenergy.2016.08.027](https://doi.org/10.1016/j.apenergy.2016.08.027).
- [68] G. G. Joseph et al. “Particle–Wall Collisions in a Viscous Fluid”. In: *Journal of Fluid Mechanics* 433 (2001), pp. 329–346. doi: [10.1017/S0022112001003470](https://doi.org/10.1017/S0022112001003470).
- [69] Q. Kang et al. “Particles in a Circulation Loop for Solar Energy Capture and Storage”. In: *Particuology* 43 (2019), pp. 149–156. doi: [10.1016/j.partic.2018.01.009](https://doi.org/10.1016/j.partic.2018.01.009).
- [70] I. Kataoka. “Local Instant Formulation of Two-Phase Flow”. In: *International Journal of Multiphase Flow* 12 (1986), pp. 745–758. doi: [10.1016/0301-9322\(86\)90049-2](https://doi.org/10.1016/0301-9322(86)90049-2).
- [71] T. Kempe and J. Fröhlich. “Collision Modelling for the Interface-Resolved Simulation of Spherical Particles in Viscous Fluids”. In: *Journal of Fluid Mechanics* 709 (2012), pp. 445–489. doi: [10.1017/jfm.2012.343](https://doi.org/10.1017/jfm.2012.343).
- [72] W. Kong et al. “Bubbling and Slugging of Geldart Group A Powders in Small Diameter Columns”. In: *Industrial and Engineering Chemistry Research* 56 (2017), pp. 4136–4144. doi: [10.1021/acs.iecr.6b04798](https://doi.org/10.1021/acs.iecr.6b04798).
- [73] H. Kruggel-Emden et al. “Review and Extension of Normal Force Models for the Discrete Element Method”. In: *Powder Technology* 171 (2007), pp. 157–173. doi: [10.1016/j.powtec.2006.10.004](https://doi.org/10.1016/j.powtec.2006.10.004).
- [74] A. Le Gal et al. “Particle Flow and Heat Transfer in Fluidized Bed-in-Tube Solar Receivers”. In: *AIP Conference Proceedings* 2303 (2020), p. 070002. doi: [10.1063/5.0028761](https://doi.org/10.1063/5.0028761).
- [75] D. Legendre, C. Daniel, and P. Guiraud. “Experimental Study of a Drop Bouncing on a Wall in a Liquid”. In: *Physics of Fluids* 17 (2005), p. 097105. doi: [10.1063/1.2010527](https://doi.org/10.1063/1.2010527).
- [76] D. Legendre et al. “A Note on the Modelling of the Bouncing of Spherical Drops or Solid Spheres on a Wall in Viscous Fluid”. In: *Chemical Engineering Science* 61 (2006), pp. 3543–3549. doi: [10.1016/j.ces.2005.12.028](https://doi.org/10.1016/j.ces.2005.12.028).
- [77] J. W. Maccoll. “Aerodynamics of a Spinning Sphere”. In: *The Aeronautical Journal* 32 (1928), pp. 777–798. doi: [10.1017/S0368393100136260](https://doi.org/10.1017/S0368393100136260).
- [78] K. Matsubara et al. “High-Temperature Fluidized Receiver for Concentrated Solar Radiation by a Beam-down Reflector System”. In: *Energy Procedia* 49 (2014), pp. 447–456. doi: [10.1016/j.egypro.2014.03.048](https://doi.org/10.1016/j.egypro.2014.03.048).
- [79] S. McNamara and W. R. Young. “Inelastic Collapse and Clumping in a One-dimensional Granular Medium”. In: *Physics of Fluids A: Fluid Dynamics* 4 (1992), pp. 496–504. doi: [10.1063/1.858323](https://doi.org/10.1063/1.858323).

- [80] E. E. Michaelides, C. T. Crowe, and J.D. Schwarzkopf. *Multiphase Flow Handbook*. Second edition. CRC Press, 2017.
- [81] E. E. Michaelides and A. Roig. “A Reinterpretation of the Odar and Hamilton Data on the Unsteady Equation of Motion of Particles”. In: *AIChE Journal* 57 (2011), pp. 2997–3002. doi: [10.1002/aic.12498](https://doi.org/10.1002/aic.12498).
- [82] B. V. Mirtich. “Impulse-based dynamic simulation of rigid body systems”. PhD thesis. University of California, Berkeley, 1996.
- [83] F. Mohaghegh and H. S. Udaykumar. “Modeling Collisions of Arbitrary-Shaped Particles in Simulations of Particulate Flows”. In: *Powder Technology* 344 (2019), pp. 756–772. doi: [10.1016/j.powtec.2018.12.062](https://doi.org/10.1016/j.powtec.2018.12.062).
- [84] H. Müller-Steinhagen. “Concentrating Solar Thermal Power”. In: *Philosophical Transactions of the Royal Society A: Mathematical, Physical and Engineering Sciences* 371 (2013), p. 20110433. doi: [10.1098/rsta.2011.0433](https://doi.org/10.1098/rsta.2011.0433).
- [85] B. Oesterlé and T. Bui Dinh. “Experiments on the Lift of a Spinning Sphere in a Range of Intermediate Reynolds Numbers”. In: *Experiments in Fluids* 25 (1998), pp. 16–22. doi: [10.1007/s003480050203](https://doi.org/10.1007/s003480050203).
- [86] A. Ozel et al. “Particle Resolved Direct Numerical Simulation of a Liquid–Solid Fluidized Bed: Comparison with Experimental Data”. In: *International Journal of Multiphase Flow* 89 (2017), pp. 228–240. doi: [10.1016/j.ijmultiphaseflow.2016.10.013](https://doi.org/10.1016/j.ijmultiphaseflow.2016.10.013).
- [87] N. A. Patankar et al. “A New Formulation of the Distributed Lagrange Multiplier/Fictitious Domain Method for Particulate Flows”. In: *International Journal of Multiphase Flow* 26 (2000), pp. 1509–1524. doi: [10.1016/S0301-9322\(99\)00100-7](https://doi.org/10.1016/S0301-9322(99)00100-7).
- [88] I. Perez Lopez et al. “On-Sun Operation of a 150kWth Pilot Solar Receiver Using Dense Particle Suspension as Heat Transfer Fluid”. In: *Journal of Solar Energy* 137 (2016), pp. 463–476. doi: [10.1016/j.solener.2016.08.034](https://doi.org/10.1016/j.solener.2016.08.034).
- [89] C. S. Peskin. “Numerical Analysis of Blood Flow in the Heart”. In: *Journal of Computational Physics* 25 (1977), pp. 220–252. doi: [10.1016/0021-9991\(77\)90100-0](https://doi.org/10.1016/0021-9991(77)90100-0).
- [90] G. Pianet et al. “Assessment of the 1-Fluid Method for DNS of Particulate Flows: Sedimentation of a Single Sphere at Moderate to High Reynolds Numbers”. In: *Computers & Fluids* 36 (2007), pp. 359–375. doi: [10.1016/j.compfluid.2005.12.001](https://doi.org/10.1016/j.compfluid.2005.12.001).
- [91] M. Ploquin et al. “CFD Investigation of Level Fluctuations in Steam Accumulators as Thermal Storage: A Direct Steam Generation Application”. In: *Solar Energy* 245 (2022), pp. 11–18. doi: [10.1016/j.solener.2022.08.048](https://doi.org/10.1016/j.solener.2022.08.048).
- [92] Elbridge Gerry Puckett et al. “A High-Order Projection Method for Tracking Fluid Interfaces in Variable Density Incompressible Flows”. In: *Journal of Computational Physics* 130 (1997), pp. 269–282.

- [93] L. Vu-Quoc and X. Zhang. "An Elastoplastic Contact Force–Displacement Model in the Normal Direction: Displacement–Driven Version". In: *Proceedings of the Royal Society of London. Series A: Mathematical, Physical and Engineering Sciences* 455 (1999), pp. 4013–4044. doi: [10.1098/rspa.1999.0488](https://doi.org/10.1098/rspa.1999.0488).
- [94] M. Rahmani and A. Wachs. "Free Falling and Rising of Spherical and Angular Particles". In: *Physics of Fluids* 26 (2014), p. 083301. doi: [10.1063/1.4892840](https://doi.org/10.1063/1.4892840).
- [95] M. W. Reeks and S. McKee. "The Dispersive Effects of Basset History Forces on Particle Motion in a Turbulent Flow". In: *Physics of Fluids* 27 (1984), pp. 1573–1582. doi: [10.1063/1.864812](https://doi.org/10.1063/1.864812).
- [96] J. F. Richardson and W. N. Zaki. "The Sedimentation of a Suspension of Uniform Spheres under Conditions of Viscous Flow". In: *Chemical Engineering Science* 3 (1954), pp. 65–73. doi: [10.1016/0009-2509\(54\)85015-9](https://doi.org/10.1016/0009-2509(54)85015-9).
- [97] J.b. Ritz and J.p. Caltagirone. "A Numerical Continuous Model for the Hydrodynamics of Fluid Particle Systems". In: *International Journal for Numerical Methods in Fluids* 30 (1999), pp. 1067–1090.
- [98] S. I. Rubinow and Joseph B. Keller. "The Transverse Force on a Spinning Sphere Moving in a Viscous Fluid". In: *Journal of Fluid Mechanics* 11 (1961), p. 447. doi: [10.1017/S0022112061000640](https://doi.org/10.1017/S0022112061000640).
- [99] A. Ruiz-Angulo and M. L. Hunt. "Measurements of the Coefficient of Restitution for Particle Collisions with Ductile Surfaces in a Liquid". In: *Granular Matter* 12 (2010), pp. 185–191. doi: [10.1007/s10035-010-0166-y](https://doi.org/10.1007/s10035-010-0166-y).
- [100] F. Sabatier et al. "Experiments Support Simulations by the NEPTUNE_CFD Code in an Upflow Bubbling Fluidized Bed Reactor". In: *Chemical Engineering Journal* 385 (2020), p. 123568. doi: [10.1016/j.cej.2019.123568](https://doi.org/10.1016/j.cej.2019.123568).
- [101] P. G. Saffman. "The Lift on a Small Sphere in a Slow Shear Flow". In: *Journal of Fluid Mechanics* 22 (1965), pp. 385–400. doi: [10.1017/S0022112065000824](https://doi.org/10.1017/S0022112065000824).
- [102] N. Sharma and N. A. Patankar. "A Fast Computation Technique for the Direct Numerical Simulation of Rigid Particulate Flows". In: *Journal of Computational Physics* 205 (2005), pp. 439–457. doi: [10.1016/j.jcp.2004.11.012](https://doi.org/10.1016/j.jcp.2004.11.012).
- [103] A. B. Stevens and C. M. Hrenya. "Comparison of Soft-Sphere Models to Measurements of Collision Properties during Normal Impacts". In: *Powder Technology* 154 (2005), pp. 99–109. doi: [10.1016/j.powtec.2005.04.033](https://doi.org/10.1016/j.powtec.2005.04.033).
- [104] S. Subramaniam and S. Balachandar. *Modeling Approaches and Computational Methods for Particle-laden Turbulent Flows*. Academic Press, 2022.
- [105] S. Sundaresan, A. Ozel, and J. Kolehmainen. "Toward Constitutive Models for Momentum, Species, and Energy Transport in Gas–Particle Flows". In: *Annual Review of Chemical and Biomolecular Engineering* 9 (2018), pp. 61–81. doi: [10.1146/annurev-chembioeng-060817-084025](https://doi.org/10.1146/annurev-chembioeng-060817-084025).
- [106] T. Tanaka, K. Yamagata, and Y. Tsuji. "Experiment of Fluid Forces on a Rotating Sphere and Spheroid". In: *KSME/JSME THERMAL and FLUID Engineering Conference* (1990), pp. 366–369.

Bibliography

- [107] R. Temam and A. Miranville. *Mathematical Modeling in Continuum Mechanics*. 2nd ed. Cambridge University Press, 2005. doi: [10.1017/CB09780511755422](https://doi.org/10.1017/CB09780511755422).
- [108] S. Tenneti and S. Subramaniam. “Particle-Resolved Direct Numerical Simulation for Gas-Solid Flow Model Development”. In: *Annual Review of Fluid Mechanics* 46 (2014), pp. 199–230. doi: [10.1146/annurev-fluid-010313-141344](https://doi.org/10.1146/annurev-fluid-010313-141344).
- [109] A. Toutant and F. Bataille. “Turbulence Statistics in a Fully Developed Channel Flow Submitted to a High Temperature Gradient”. In: *International Journal of Thermal Sciences* 74 (2013), pp. 104–118. doi: [10.1016/j.ijthermalsci.2013.06.003](https://doi.org/10.1016/j.ijthermalsci.2013.06.003).
- [110] G. Tryggvason, R. Scardovelli, and S. Zaleski. *Direct Numerical Simulations of Gas-Liquid Multiphase Flows*. Cambridge: Cambridge Univ. Press, 2011. doi: [10.1017/CB09780511975264](https://doi.org/10.1017/CB09780511975264).
- [111] M. Uhlmann. “Interface-Resolved Direct Numerical Simulation of Vertical Particulate Channel Flow in the Turbulent Regime”. In: *Physics of Fluids* 20 (2008), p. 053305. doi: [10.1063/1.2912459](https://doi.org/10.1063/1.2912459).
- [112] M. A. Van Der Hoef et al. *Multiscale Modeling of Gas-Fluidized Beds*. Vol. 31. Academic Press, 2006, pp. 65–149. doi: [10.1016/S0065-2377\(06\)31002-2](https://doi.org/10.1016/S0065-2377(06)31002-2).
- [113] M. A. Van Der Hoef et al. “Numerical Simulation of Dense Gas-Solid Fluidized Beds: A Multiscale Modeling Strategy”. In: *Annual Review of Fluid Mechanics* 40 (2008), pp. 47–70. doi: [10.1146/annurev.fluid.40.111406.102130](https://doi.org/10.1146/annurev.fluid.40.111406.102130).
- [114] C. Veeramani, P. D. Mineev, and K. Nandakumar. “A Fictitious Domain Formulation for Flows with Rigid Particles: A Non-Lagrange Multiplier Version”. In: *Journal of Computational Physics* 224 (2007), pp. 867–879. doi: [10.1016/j.jcp.2006.10.028](https://doi.org/10.1016/j.jcp.2006.10.028).
- [115] S. Vincent et al. “A Lagrangian VOF Tensorial Penalty Method for the DNS of Resolved Particle-Laden Flows”. In: *Journal of Computational Physics* 256 (2014), pp. 582–614. doi: [10.1016/j.jcp.2013.08.023](https://doi.org/10.1016/j.jcp.2013.08.023).
- [116] A. Wachs et al. “Accuracy of Finite Volume/Staggered Grid Distributed Lagrange Multiplier/Fictitious Domain Simulations of Particulate Flows”. In: *Computers & Fluids* 115 (2015), pp. 154–172. doi: [10.1016/j.compfluid.2015.04.006](https://doi.org/10.1016/j.compfluid.2015.04.006).
- [117] O. R. Walton and R. L. Braun. “Viscosity, Granular-temperature, and Stress Calculations for Shearing Assemblies of Inelastic, Frictional Disks”. In: *Journal of Rheology* 30 (1986), pp. 949–980. doi: [10.1122/1.549893](https://doi.org/10.1122/1.549893).
- [118] Z. Yan et al. “Discrete Element Modelling (DEM) Input Parameters: Understanding Their Impact on Model Predictions Using Statistical Analysis”. In: *Computational Particle Mechanics* 2 (2015), pp. 283–299. doi: [10.1007/s40571-015-0056-5](https://doi.org/10.1007/s40571-015-0056-5).
- [119] N. N. Yanenko. *The Method of Fractional Steps*. Berlin, Heidelberg: Springer, 1971. doi: [10.1007/978-3-642-65108-3](https://doi.org/10.1007/978-3-642-65108-3).

- [120] F.-L. Yang and M. L. Hunt. “Dynamics of Particle-Particle Collisions in a Viscous Liquid”. In: *Physics of Fluids* 18 (2006), p. 121506. doi: [10.1063/1.2396925](https://doi.org/10.1063/1.2396925).
- [121] L. Yang et al. “Unified One-Fluid Formulation for Incompressible Flexible Solids and Multiphase Flows: Application to Hydrodynamics Using the Immersed Structural Potential Method (ISPM): Unified ISPM for Incompressible Solids and Multiphase Flows”. In: *International Journal for Numerical Methods in Fluids* 86 (2018), pp. 78–106. doi: [10.1002/flid.4408](https://doi.org/10.1002/flid.4408).
- [122] S. B. Yeom et al. “Application of the Discrete Element Method for Manufacturing Process Simulation in the Pharmaceutical Industry”. In: *Pharmaceutics* 11 (2019), p. 414. doi: [10.3390/pharmaceutics11080414](https://doi.org/10.3390/pharmaceutics11080414).
- [123] Z. Yu and A. Wachs. “A Fictitious Domain Method for Dynamic Simulation of Particle Sedimentation in Bingham Fluids”. In: *Journal of Non-Newtonian Fluid Mechanics* 145 (2007), pp. 78–91. doi: [10.1016/j.jnnfm.2007.02.007](https://doi.org/10.1016/j.jnnfm.2007.02.007).
- [124] Z. Yu et al. “Viscoelastic Mobility Problem of a System of Particles”. In: *Journal of Non-Newtonian Fluid Mechanics* 104 (2002), pp. 87–124. doi: [10.1016/S0377-0257\(02\)00014-9](https://doi.org/10.1016/S0377-0257(02)00014-9).
- [125] R. Zenit and M. L. Hunt. “Mechanics of Immersed Particle Collisions”. In: *Journal of Fluids Engineering* 121 (1999), pp. 179–184. doi: [10.1115/1.2821999](https://doi.org/10.1115/1.2821999).
- [126] H. Zhang et al. “High-Efficiency Solar Power Towers Using Particle Suspensions as Heat Carrier in the Receiver and in the Thermal Energy Storage”. In: *Renewable Energy* 111 (2017), pp. 438–446. doi: [10.1016/j.renene.2017.03.101](https://doi.org/10.1016/j.renene.2017.03.101).
- [127] H. Zhang et al. “Particle Circulation Loops in Solar Energy Capture and Storage: Gas–Solid Flow and Heat Transfer Considerations”. In: *Applied Energy* 161 (2016), pp. 206–224. doi: [10.1016/j.apenergy.2015.10.005](https://doi.org/10.1016/j.apenergy.2015.10.005).
- [128] H. Zhang et al. “Scale-up Considerations of the UBFB Solar Receiver”. In: *AIP Conference Proceedings* 2126 (2019), p. 030067. doi: [10.1063/1.5117579](https://doi.org/10.1063/1.5117579).
- [129] X. Zhang and L. Vu-Quoc. “Modeling the Dependence of the Coefficient of Restitution on the Impact Velocity in Elasto-Plastic Collisions”. In: *International Journal of Impact Engineering* 27 (2002), pp. 317–341. doi: [10.1016/S0734-743X\(01\)00052-5](https://doi.org/10.1016/S0734-743X(01)00052-5).
- [130] Z. Zhou et al. “Hydrodynamic Force and Torque Models for a Particle Moving near a Wall at Finite Particle Reynolds Numbers”. In: *International Journal of Multiphase Flow* 92 (2017), pp. 1–19. doi: [10.1016/j.ijmultiphaseflow.2017.01.018](https://doi.org/10.1016/j.ijmultiphaseflow.2017.01.018).

ABSTRACT / RÉSUMÉ

In english

Fluid particle flows hold significant importance in a variety of industrial applications, particularly in the context of third-generation concentrated solar power plants, where they can be used as both a heat transfer fluid and a storage medium. However, studying these flows presents considerable challenges due to the complex multiscale interactions governing them. Numerical simulation, particularly Direct Numerical Simulation (DNS) methods where the resolution is smaller than the particle diameter, emerges as a promising tool for better understanding these flows and aiding in the design of pilot-scale industrial applications. The increase in computational capabilities and the performance of numerical algorithms has made the particle resolved simulations of fluidized beds increasingly feasible for representative studies.

In this thesis, we present a numerical method based on the one-fluid formulation. This method combines the front tracking method with the viscous penalty method to simulate fluid particle flow behaviors. The front tracking method employs a dual mesh system. This system effectively tracks the moving solid interfaces, represented as a moving mesh, across a fixed simulation grid, ensuring accuracy in representing the particle movements. The viscous penalty method, on the other hand, plays a pivotal role in ensuring the fidelity of rigid body motion within the particles. This is achieved by treating the fluid within the particles as an extremely viscous medium, thereby enabling the simulation to realistically mimic the behavior of fluid particles under various conditions.

For short-term interactions between particles, a combined collision model is used. This model adeptly accounts for both viscous dissipation and solid dissipation, primarily due to lubrication effects and inelastic contacts between particles, respectively. The nuanced approach of this model allows for more natural simulations of particle interactions, reducing the reliance on arbitrary numerical parameters often seen in other models cited in the literature. The algorithm is implemented in TrioCFD an open-source framework designed for massively parallel computing. The accuracy and reliability of the simulation code were rigorously tested against well-established benchmarks in the literature. Furthermore, the thesis includes a parametric simulation of a lab-scale fluidized bed, comparing the accuracy of the algorithm against both experimental and numerical results. These comparisons demonstrate that the proposed algorithm aligns well with established benchmarks and exhibits good accuracy in its predictions.

In french

Les écoulements de fluide particules jouent un rôle important dans une variété d'applications industrielles, particulièrement dans le contexte des centrales solaires à concentration de troisième génération, où ils peuvent être utilisés à la fois comme fluide caloporteur et moyen de stockage thermique. Cependant, l'étude de ces écoulements présente des défis considérables en raison de la complexité des interactions multi-échelles qui les régissent. La simulation numérique, et en particulier les méthodes de Simulation Numérique Directe (DNS) où la résolution est inférieure au diamètre des particules, émerge comme un outil prometteur pour mieux comprendre ces écoulements. L'augmentation des moyens de calcul et la performance des algorithmes numériques ont rendu les simulations de lits fluidisés avec particules résolues de plus en plus réalisables pour des études à des échelles représentatives. Dans cette thèse, nous présentons une méthode numérique basée sur la formulation mono-fluide. Cette méthode combine la méthode de suivi de front avec la méthode de pénalisation visqueuse pour simuler les comportements des écoulements particuliers. La méthode de suivi de front utilise un système de maillage double. Ce système suit efficacement les interfaces solides en mouvement, représentées par un maillage mobile, à travers une grille de simulation fixe, garantissant ainsi la précision dans la représentation des mouvements des particules. La méthode de pénalisation visqueuse, quant à elle, joue un rôle essentiel pour assurer la condition de non-déformation à l'intérieur des particules. Cela est réalisé en traitant le fluide à l'intérieur des particules comme un milieu extrêmement visqueux, permettant ainsi à la simulation de reproduire de manière réaliste le comportement des particules solides dans diverses conditions. Pour les interactions à courte distance entre les particules, un modèle de collision combiné est utilisé. Ce modèle prend habilement en compte à la fois la dissipation visqueuse et la dissipation solide, principalement dues aux effets de lubrification et aux contacts inélastiques entre les particules, respectivement. L'approche nuancée de ce modèle permet des simulations plus naturelles des interactions entre particules, réduisant le nombre de paramètres numériques à utiliser dans le modèle. L'algorithme résultant est implémenté dans TrioCFD un code open-source conçu pour le calcul parallèle massif. La précision et la fiabilité du code de simulation ont été testées contre des références bien établies dans la littérature. De plus, la thèse inclut une simulation paramétrique d'un lit fluidisé à l'échelle de laboratoire, comparant la précision de l'algorithme aux résultats expérimentaux et numériques. Ces comparaisons démontrent que l'algorithme proposé reproduit correctement les références établies

